Refining Greenland geothermal heat flux through stable isotope analysis

Master Thesis in Earth Sciences (MSc)
at the University of Bergen, Norway

Jakob Gradl

Department of Earth Sciences
March, 2023

Abstract

Geothermal heat flux is an important control on the dynamics of glaciers and ice sheets. In Greenland however, only few direct observations of geothermal heat flux exist. The exact spatial distribution and magnitude of heat flux in Greenland is therefore largely unknown. Many studies have attempted to constrain heat flux in Greenland indirectly by modelling it based on other observable variables, such as the seismic and magnetic structure of the Greenland lithosphere, or through techniques that extrapolate the existing measurements onto models of the Greenland lithology. Various estimates of Greenand heat flux have been produced this way, however many do not agree well with each other and show large inter-estimate variability both in terms of magnitude and spatial distribution of estimated heat flux values.

Stable isotope composition of basal meltwater has previously not been considered in efforts to constrain Greenland geothermal heat flux. The ice layers in the Greenland ice sheet show large differences in δ^{18}O values resulting from changes in climate throughout their depositional history. If different ice layers are in contact with the bed, then spatial differences in geothermal heat flux will affect the local meltrates these layers experience at the ice sheet base and hence modulate the amount of meltwater each layer contributes into the subglacial drainaige system. If the δ^{18}O values of the melting ice layers are sufficiently different, the isotopic composition of the mixed meltwater that flows through the subglacial hydrological system will be different for different spatial distributions of geothermal heat flux.

By simulating the basal meltwater production in Greenland based on different published estimates of Greenland geothermal heat flux, I show in this thesis that different heat fluxes result in differences in the age distribution of the basal ice. In particular, the presence and extent of Eemian ice in central northern Greenland shows substantial differences for different heat flux estimates. As Eemian ice, being interglacial ice, shows higher δ^{18}O values than ice from the last glacial period, the modelled differences in Eemian extent result in detectable differences in the isotopic composition of the basal meltwater in North-east Greenland on the order of few permille. Stable isotope composition of basal meltwater might thus have the potential to contribute to the discussion about a heat flux hotspot in central northern Greenland.

Acknowledgements

Well, this is it. After almost eight years and having basically lived at my lesesalplass these past few weeks, I'm finally at the end of my studies now with a finished Master thesis. I could never have maneged this on my own without all the wonderful people that supported me along the way.

First of all, I would like to thank my supervisor Basile and my co-supervisor Hans Christian.

Basile, thank you for your patience through this project. I had no clue about ice modelling when I started this thesis, but you managed to slowly turn me into a modeller. Even though most of our communication was through Slack, I could always count on you to figure out ISSM issues for me and explain to me how python works. Your perspective on the process of constructing an ice sheet model and running simulations kept me motivated throughout this thesis. After seven months of un-successfully trying to set up a model of the Greenland ice sheet and another three months of losing my mind over a 1200-line routing algorithm, your pep-talks always brought me back to reality. I couldn't have done this project without you!

Hans Christian, thank you for giving me the opportunity to do some actual isotope measurements in this project about isotopes. That was a welcome distraction from the long days of staring into ISSM code and obsessing over why my simulations don't work.

I also want to say a big thank you to Martin Rückamp from the Bavarian Academy of Sciences for donating one of your Greenland models to me. After hiving tried to set up my own Greenland model in ISSM for months and months without success, the model but also your advice, experience, and knowledge that you shared so freely with me were critical to get this thesis going.

Elana, thank you for coffee hangs and moral support. I can't even count the hours we spent ranting about ISSM and inexplicably un-successful model runs. Having someone who is going through the same process of slowly turning into an ice-sheet modeller without

any prior coding experience, who is living through the same pit-falls and frustrations, who just gets what it feels like when the gazillionth model run still crashes and you still can't figure out what's going on was invaluable to keeping me sane through this project. Now I'm looking forward to many more coffee hangs and slowly working our way through all cafés in Bergen until you deliver your project as well :)

Vivien, thank you for being my best friend. We have lived through the ups and downs of our Bachelor and Master studies together (most of the time anyway...) and I can always count on you to lift me back up again when I'm down.

I want to thank my lunch group for giving me a social environment to balance out my coding life. When it's only me and my three computer screens the whole day, half an hour of human contact makes a world of difference. Thanks for cake-Mondays and wine lotteries. And thanks for the Cricket set ;)

Lastly, I want to thank Sølvi Haugland and the rest of the team at the Real kaffebar downstairs for being the first ones to throw a cheerful 'Heihei' at me in the morning, making delicious sandwiches, and supplying me with all the coffee re-fills I need to get through my day.

Contents

Nomenclature

Abbreviations:

C1-7	Black Circle analysis locations
GHF	Geothermal heat flux
ISSM	Ice-sheet and Sea-level System Model
GRIP	Greenland Ice core Porject
NGRIP	North Greenland Ice core Project
EGRIP	East Greenland Ice core Project
NEGIS	North-East Greenland ice stream
T1-10	Blue Triangle analysis locations
kyrs	thousands of years
ka BP	thousands of years ago before present
VSMOW	Vienna Standard Mean Ocean Water

GHF sets:

Colgan22, Colgan22NG	Colgan et al. (2022)
Greve19	Greve (2019)
Martos18	Martos et al. (2018)
FMaule09	Fox Maule et al. (2009)
Shapiro04	Shapiro and Ritzwoller (2004)
Lucazeau19	Lucazeau (2019)
GHF01-07	Synthetic GHF maps

Chapter 1

Introduction

Mass loss from the global cryosphere at present is responsible for more than half of climate change induced global sea level rise accounting for 1.9 of a total of 3.5 mm/yr sea level rise (millimetre per year) (Group, 2018). The Greenland ice sheet alone loses over 240 Billion tons of ice every year (Fox-Kemper et al., 2021; Shepherd et al., 2020; Khan et al., 2015) equating to a global sea level rise contribution of 0.8 mm/yr rendering it one of the largest single contributors to rising sea levels (Group, 2018). Hosting a staggering 2.6 Million cubic kilometers of ice (Grotzinger and Jordan, 2017), it has the potential to add 7.4 m to current sea level (Morlighem et al., 2017).

To investigate and constrain the impact the Greenland ice sheet will have on future sea level, projections and estimates of its future melt have been developed based on its current physical state and likely scenarios of future climate development (summarized in Fox-Kemper et al., 2021). Such investigations are performed by simulating the future behavior of the Greenland ice sheet using ice sheet models.

In order to produce accurate data, ice sheet models need sufficient boundary conditions that ensure stability and realism for the simulation. Through their control on the dynamics of the ice sheet, they can have great impact on the result of simulations. Geothermal heat flux (GHF) is an important boundary condition in ice sheet modelling as it controls the basal thermal state of the ice sheet (e.g., Meierbachtol et al., 2015; Näslund et al., 2005) and plays a leading role in the production of meltwater (e.g., McCormack et al., 2022; Kang et al., 2022). Consequently, the GHF influences the overall flow dynamics and thus geometry of the ice sheet (e.g., Greve and Hutter, 1995) and exerts control on flow speed through basal lubrication that is provided by meltwater (e.g., Smith-Johnsen et al., 2020) and thus ultimately mass loss through melting and calving.

However, since the GHF is a property of the bedrock-ice interface underneath the ice sheet it unfortunately eludes measurement and is therefore still largely mysterious (Davies

and Davies, 2010). This is problematic. Since the GHF exerts large control on ice dynamics, differences in GHF estimates employed in ice flow models will result in different ice sheet behaviour. For example, Rogozhina et al. (2012) demonstrated that simulating the past evolution of the Greenland ice sheet with different estimates of geothermal heat flux lead to large differences in modelled present-day ice sheet surface elevation.

Several estimates of the Greenland GHF have been put forth that aimed to constrain it through its relation to other quantities or other indirect methods (e.g., Greve, 2019; Martos et al., 2018; Shapiro and Ritzwoller, 2004; Lucazeau, 2019). But as wide as the range of methods that was used to produce these estimates, as wide is also the range of values and spatial distributions of GHF they produce. So in spite of several attempts to constrain the Greenland GHF, greater clarity about its form has so far not been achieved.

Stable isotope composition of Greenland meltwater has so far not been considered in efforts to constrain Greenland GHF. In this thesis, I will evaluate the potential of meltwater stable isotope analysis to infer information about the spatial variability and magnitude of heat flux underneath the Greenland ice sheet by simulating the thermo-mechanical response of the ice sheet to different published and synthetic GHF estimates and the imprint this leaves in basal meltwater isotopic composition. The aim of this thesis is to test the feasibility of this approach and produce a first estimate of the range and kind of information that can be gained from it about geothermal heat flux in Greenland.

The thesis is structured as follows: First, all necessary scientific background regarding ice dynamics, geothermal heat flux, and isotopic composition of ice are summarized in chapter 2. The following chapter 3 describes the concept of the suggested approach in more detail and presents the methodology used in this thesis to test it. The results of the analysis will be presented in chapter 4 and discussed in chapter 5. Finally, chapter 6 concludes the thesis.

Chapter 2

Scientific Background

2.1 What even is an Ice Sheet

Glaciers and ice sheets (as summarized by Grotzinger and Jordan, 2017) form in regions where snow is able to accumulate on the ground over several years. Over time, the initially loose snow will compact into an increasingly dense layer, which under its own increasing weight will eventually be transformed into ice. Accumulating more snow on its surface each winter, the newly formed glacier will grow and eventually start to deform under the load of its own weight. Ice inside the glacier will be transported away from regions of high surface accumulation (the accumulation area) to regions of melt where ice is removed from the glacier (the ablation area).

Valley glaciers form in high alpine regions where snow is able to accumulate on the flanks of mountains. Following gravity, they flow downwards into the adjacent valleys typically filling the entire width of the valley floor. They can reach between tens and up to several hundreds of meters in thickness and up to several kilometers in length.

Continental ice sheets extend far beyond individual mountain valleys and cover large areas of land. The Greenland ice sheet covers about 80 % of the land area in Greenland, the Antarctic ice sheet covers more than 90 % of the Antarctic continent. Their thickness is on the order of several kilometers, one to two orders of magnitude above the thickness of valley glaciers. In Greenland at the highest point of the ice sheet, the ice is more than 3.2 kilometers thick.

The accumulation area of glaciers and ice sheets is located in their highest regions. In valley glaciers, this is at the uphill end of the glacier. From there, the ice flows downwards towards the ablation area, located at the downhill end of the glacier. Their flow is thus one-directional. In ice sheets, the accumulation area is located in the centre and the ice

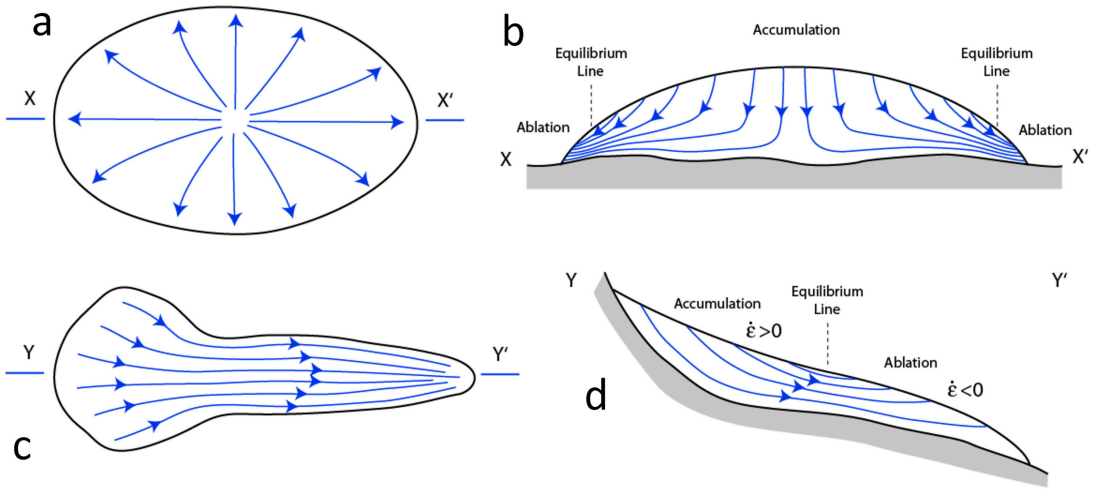

Figure 2.1: Schematics of the differences in flow between ice sheets (a,b) and valley glaciers (c,d). a,c: Top view; b,d: cross-section. Figure from Hudleston (2015).

flows down and outwards. Their ablation area is located along the entire margin of the ice sheet, so the ice flows from the centre outwards into all directions. The difference in flow is illustrated in figure 2.1.

2.1.1 The ice sheet in Greenland

The Greenland ice sheet is the largest continental ice mass in the northern hemisphere. It covers an area of more than 1.7 Million km^2 which is over 80 % of the Greenland land area (Grotzinger and Jordan, 2017). At it's thickest regions in the centre of Greenland, the ice sheet is over 3.2 km thick (Morlighem et al., 2017). From there, the ice flows outwards and into the surrounding oceans through a system of ice streams and outlet glaciers around its margin. The ice that is drained into the ocean is currently not being fully replaced and the mass of the ice sheet is in regress diminishing at a rate of over 240 Billion tons of ice every year (Shepherd et al., 2020).

Figure 2.2a shows a map of the surface velocity of the Greenland ice sheet. The velocity increases towards the margin where the ice flow converges and drains into the ocean through ice streams and outlet glaciers. The largest ice stream is the North-East Greenland ice stream (NEGIS) which drains ca. 16 % of the entire Greenland ice area (Rignot and Mouginot, 2012). In the central parts of the ice sheet, there is a clearly visible line of very low flow velocity. This is the central ice divide, all ice flows away from this line. The ice divide has multiple branches and subdivides the ice sheet into individual drainage basins (Zwally et al., 2012), shown in figure 2.2b. All ice that is in the same drainage basin will flow towards the same outlet glacier at the ice margin.

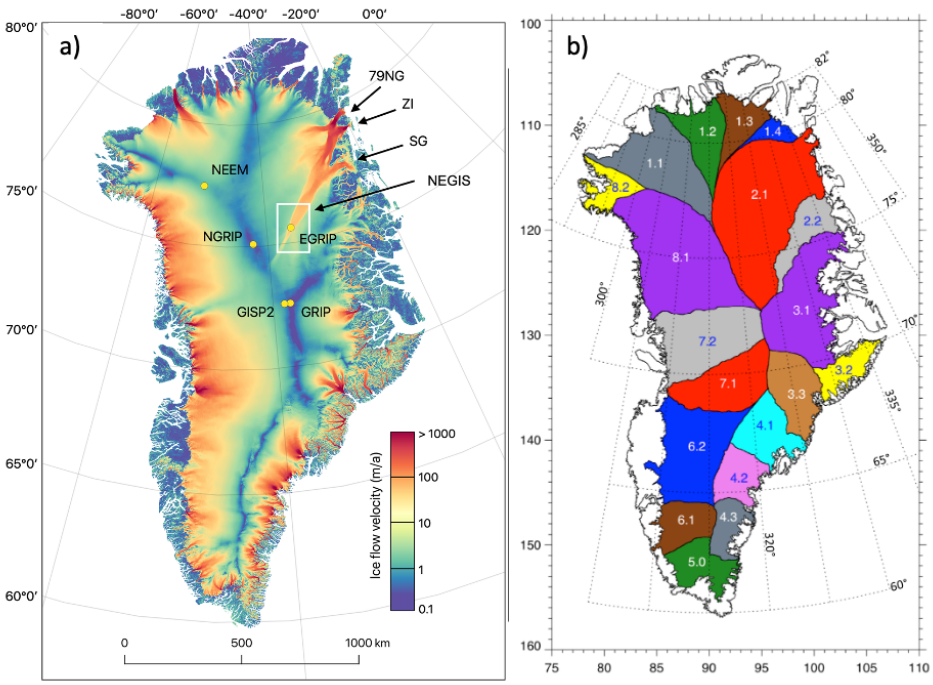

Figure 2.2: Greenland surface velocity and drainage basins. a) Map of Greenland surface velocity. Yellow dots indicate ice core sites. Arrows point to NEGIS ice stream and its outlet glaciers (79NG: Nioghalvfjerdjforden; ZI: Zachariæ Isstrøm). Figure from Franke et al. (2020). b) Map of the Greenland ice drainage basins. Figure from Zwally et al. (2012).

There are several ice core drilling sites located along the central ice divide (see figure 2.2a). At the ice divide, ice flow is directed straight downwards and the stratigraphy recorded in the ice cores is not greatly disturbed by effects of ice flow. Several of the concepts behind this statement will be elucidated in the following sections.

2.1.2 Fundamentals of ice flow

Ice as a material is - to a good approximation - incompressible. As the ice is buried and moves downwards in a glacier, included air bubbles and fractures collapse under the load of the increasing overlying ice column which results in some limited densification. However, compared to the deformation resulting from the large-scale movement of the glacier or ice sheet, these processes can be neglected (Cuffey and Paterson, 2010).

The motion of ice can hence be described as that of an incompressible fluid with high viscosity (Cuffey and Paterson, 2010). Driven by gravity, differences in surface elevation cause an internal gradient in hydrostatic pressure. This is called the driving stress. Stress is a measure of how hard a material is being pushed or pulled; more technically it is a force per unit area (Benn and Evans, 2010; Hewitt, 2021). The driving stress is oriented horizontally

in the direction of downward surface slope. Since it results from differences in surface elevation, the driving stress is independent of the topography of the underlying bedrock. The movement of a glacier or ice sheet thus follows the direction of steepest surface slope, regardless of the basal topography, with greater slope resulting in greater flow velocity (Benn and Evans, 2010; Cuffey and Paterson, 2010).

The motion of glacial ice is slow enough that acceleration and inertia have negligible effects on its movement. Glaciers are thus effectively in static equilibrium, meaning that forces acting on the glacier are in balance with each other (Cuffey and Paterson, 2010). The driving stress τ_d must therefore be balanced by an equal resisting stress τ_r, such that

$$\tau_d = \tau_r = \tau_b + \tau_w + \tau_L$$

in which τ_b, τ_w, and τ_L are the components of the resisting stress (see figure 2.3). The basal drag τ_b is the result of friction between the moving ice and the underlying bed. The lateral or wall drag τ_w describes the resistance to flow along the sides of a glacier or ice stream. The longitudinal stress τ_L is the result of along-flow stress gradients, i.e., compression or tension. The longitudinal stress is typically listed as a resisting stress, which is true in the case of longitudinal compression. In the case of tensile stress however, it would effectively contribute to the driving stress (Benn and Evans, 2010).

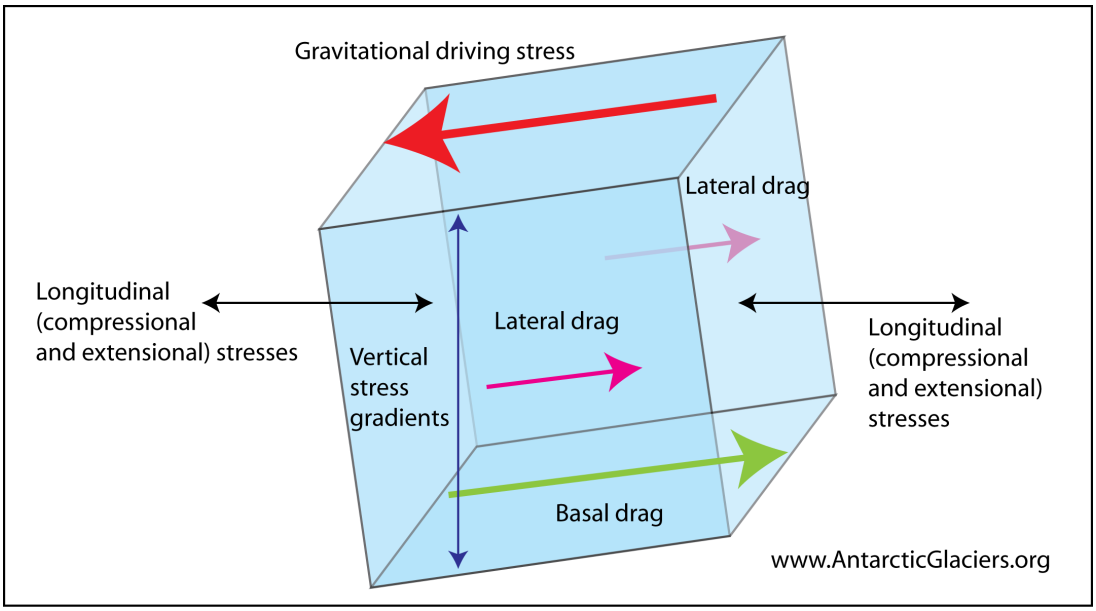

Figure 2.3: Sketch of the stress situation in a moving glacier. Figure from AntarcticGlaciers.org (2023).

The link between the stress balance of the ice and its resulting velocity is the rheology, which relates the stresses inside the ice to the strain, which describes the velocity of points

inside the ice relative to each other and is thus a measure of deformation (Hewitt, 2021). If the stress inside the ice is isotropic, i.e., equal in all directions, it is in balance and no deformation can occur. The rheology of the ice is therefore based on the deviatoric stress component, which is that component of the overall stress that deviates from being isotropic. The deviatoric stress shows a preferred direction and results in deformation of the ice in that direction (Cuffey and Paterson, 2010; Hewitt, 2021).

For ice, the most commonly used rheology law is Glen's flow law (Glen, 1955; Cuffey and Paterson, 2010)

$$\varepsilon = A\ E\ \tau^n \tag{2.1}$$

in which ε is the strain rate, τ is the stress, n is Glen's flow law exponent typically set to 3, and A and E are the creep or rate factor and the enhancement factor, respectively, which adapt the rheology to physical properties of the ice.

The relationship between stress and strain can alternatively be expressed through the viscosity η

$$\tau = 2\,\eta\,\varepsilon, \quad \text{with} \quad \eta = \frac{1}{2AE\tau^{n-1}} \tag{2.2}$$

(Hewitt, 2021; Cuffey and Paterson, 2010). The viscosity of ice is not a constant. Even though it is independent of the stress, it is influenced by several properties of the ice itself, such as temperature, ice-grain size, crystal fabric, impurity content, or liquid water content (Benn and Evans, 2010; Hewitt, 2021; Cuffey and Paterson, 2010). The rate and enhancement factors parameterize these influences and are hence necessary inclusions in Glen's flow law.

2.1.3 The importance of geothermal heat flux to ice dynamics

The movement of ice has two components that contribute to its velocity. Firstly, the weight of the ice itself causes it to deform and flow. Secondly, melting at the base of the ice will lubricate the bed with meltwater and allow the ice to slide (Cuffey and Paterson, 2010). The geothermal heat flux has the potential to influence both of these components and is thus an important factor in the movement of glaciers and ice sheets (Smith-Johnsen et al., 2020).

In the case of a frozen bed on which the ice doesn't slide, the geothermal heat flux provides the basal boundary condition for the energy balance of the ice

$$G = -k\,\frac{\partial T}{\partial n} \tag{2.3}$$

(Fowler, 2021), in which G denotes the geothermal heat flux, k is the thermal conductivity of the ice, T is the absolute temperature in Kelvin, and n is the unit normal vector pointing upwards into the ice.

As described in section 2.1.2, the viscosity of the ice changes with temperature, which is parameterized in Glen's flow law through the rate factor A. Increasing temperatures lead to softer ice and it will deform more easily under load (Cuffey and Paterson, 2010). Over the whole range of temperatures found in terrestrial ice, A varies by a factor of about 1000 (Cuffey and Paterson, 2010). As figure 2.4 shows, the influence of temperature on A is not linear and especially pronounced close to the melting point (Fowler, 2021).

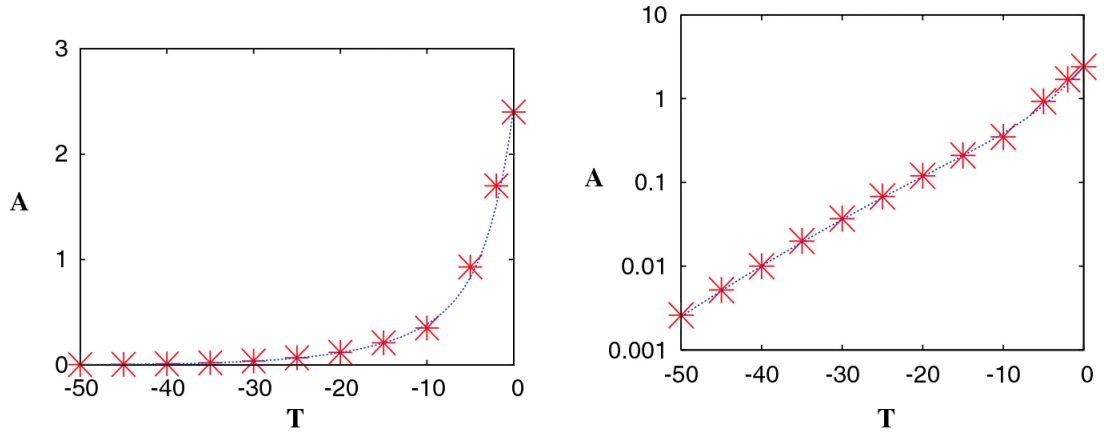

Figure 2.4: The relationship between the rate factor A and temperature T. Figure from Fowler (2021).

If the ice at the base is temperate, i.e., its temperature is at the pressure melting point, a thin layer of meltwater will form at the ice-bed interface allowing the ice to slide across the bed. This necessitates the inclusion of a frictional heat term $\tau_b u_b$ in equation 2.3 to account for the heat caused by the deformation of the sliding ice (Fowler, 2021)

$$G + \tau_b \, u_b + k \, \frac{\partial T}{\partial n} > 0 \tag{2.4}$$

in which τ_b is the basal shear stress and u_b is the basal sliding velocity.

The inequality denoted in equation 2.4 indicates net heat flux from the ice to the bed, i.e., the base of the ice is melting. Including basal melt in equation 2.4 gives

$$G + \tau_b \, u_b + k \, \frac{\partial T}{\partial n} = \rho_w \, L \, v_w \tag{2.5}$$

in which ρ_w denotes the density of water, L the latent heat, and v_w the meltwater flux per unit area (Fowler, 2021).

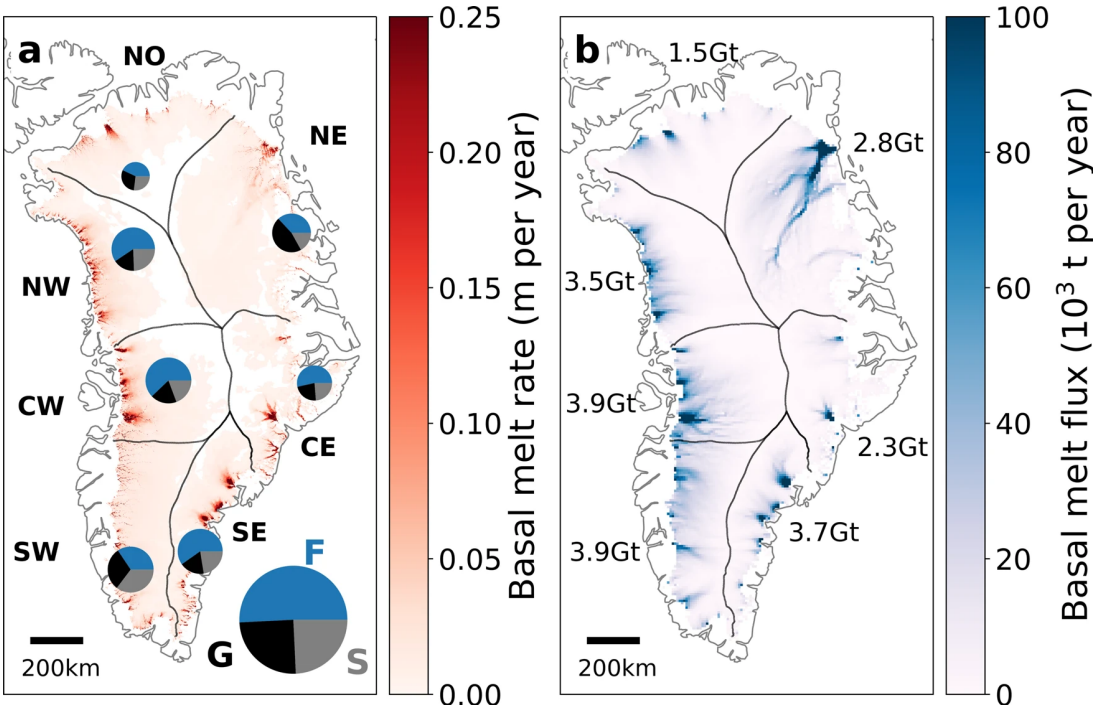

Figure 2.5: Basal melt in Greenland and resulting meltwater flux. a) Basal melt raters in Greenland. Pie charts show the respective contributions to basal melt production from geothermal heat flux (G, black), frictional heat (F, blue), and heat from surface meltwater (S, grey). b) Basal meltwater flux. Numbers indicate total flux for each sector. Figure from Karlsson et al. (2021)

Model studies show that geothermal heat flux has large influence on the dynamic behaviour of glaciers and ice sheets. Modelling the response of a glacial system in eastern Antarctica to different heat flux estimates, Kang et al. (2022) found large differences in the resulting simulations of basal thermal state and meltwater production. Karlsson et al. (2021) estimated that geothermal heat flux is responsible for around a quarter of the total basal meltwater production in Greenland, going up to almost half in the north-eastern part of the ice sheet (see figure 2.5). In a study by Rogozhina et al. (2012), a transient simulation of the Greenland ice sheet resulted in different ice sheet geometries for different heat flux estimates (see figure 2.6). Näslund et al. (2005) found substantial increases in local ice surface velocity in simulations of the paleo-Fennoscandian ice sheet when increasing the spatial resolution of the employed geothermal heat flux. Modelling studies of the North-east Greenland ice stream even suggest that exceptionally high heat flux is necessary for this system to prevail at all (Smith-Johnsen et al., 2020).

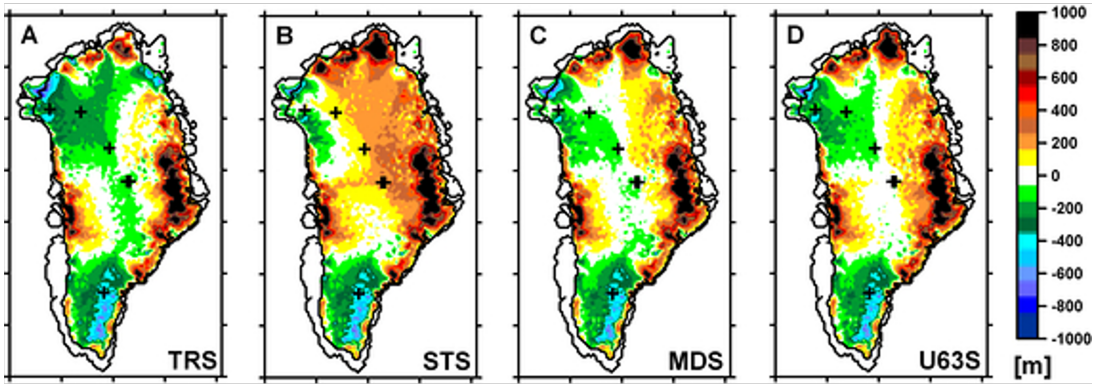

Figure 2.6: Geometry of the Greenland ice sheet as a response to four different estimates of GHF (A-D). Thicknesses are displayed relative to observed present-day ice sheet thickness. Figure from Rogozhina et al. (2012).

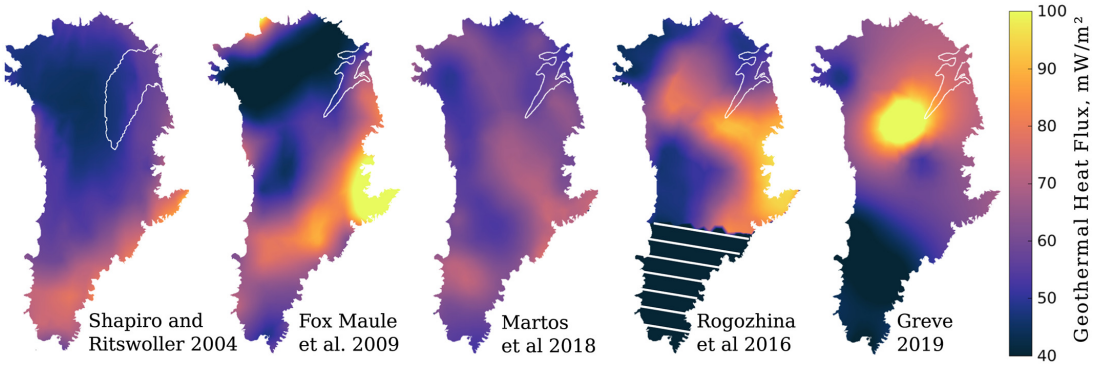

Figure 2.7: Different estimates of geothermal heat flux in Greenland. Figure from Smith-Johnsen et al. (2020).

2.2 Geothermal heat flux in Greenland

Direct observations of the geothermal heat flux underneath the Greenland ice sheet (i.e., the heat flux from the bedrock into the basal ice) are sparse since they are limited to the drilling sites of the few deep ice cores (Davies and Davies, 2010; Rezvanbehbahani et al., 2019). Table 2.1 lists observations of heat flux at five Greenland ice core drilling sites (see figures 2.2a and 2.8 for locations; Rezvanbehbahani et al., 2017; Dahl-Jensen et al., 1998; Petrunin et al., 2013; Dahl-Jensen et al., 2003; Greve, 2005). Values are between 50 and 60 mW/m^2 for GRIP, GISP2, and Camp Century. Dye-3 in the south of Greenland shows lower heat flux of 20 mW/m^2. NGRIP (North Greenland ice core project) shows particularly high heat flux of over 100 mW/m^2. Heat flux measurements on the exposed rock along the coast show values between 30 to 40 mW/m^2 at the southern tip of Greenland and between 70 to 100 mW/m^2 in the North-east (see figure 2.8). Because the GHF has such great influence on the dynamics of the Greenland ice sheet (see section 2.1.3) several studies have attempted to constrain GHF in Greenland indirectly through its relationship to other observable variables (see for example figure 2.7).

Table 2.1: Observations of geothermal heat flux at the Greenland ice core sites. Table from Rezvanbehbahani et al. (2017).

Borehole Name	Latitude (°N)	Longitude (°W)	GHF (mW m^{-2})	Reference
[i]GRIP	72.58	-37.64	51.3	*Dahl-Jensen et al.* [1998]
[i]GISP2	72.60	-38.50	60	*Petrunin et al.* [2013]
[i]NorthGRIP	75.10	-42.32	90 & 135 & 160	*Dahl-Jensen et al.* [2003]; *Greve* [2005]
[i]Dye 3	65.18	-43.82	20	*Greve* [2005]
[i]Camp Century	77.18	-61.13	50	*Greve* [2005]

Some studies use seismic data to model lithospheric properties to infer GHF from modelled heat conduction through the crust (e.g., Rogozhina et al., 2016; Artemieva, 2019; Petrunin et al., 2013). Martos et al. (2018) and Fox Maule et al. (2009) use magnetic data to infer the Curie-depth of the lithoshpere to infer GHF. Such lithoshpere-based GHF estimates typically result in an elongated band of high heat flux that extends across central northern Greenland to the eastern coast where it reaches maximum values. It is more distinct from background GHF in the models based on seismic data than the model based on magnetic data and also located further North in the former than in the latter. Seismic-based models show an area of particularly high heat flux where the high-GHF band meets the eastern coast of Greenland in the Fjordland regions which is broadly consistent with heat flux observations that likewise show higher values in this area (see figure 2.8). The high heat flux band is generally attributed to the proposed passage of the Icelandic mantle plume underneath Greenland between ca. 80 and 30 Million years ago. However, Colgan et al. (2022) note that this plume track might only be an artefact of the geophysically inferred lithosphere parameters of the models. They argue that the observable imprints of the potential passage of the Icelandic plume are now likely limited to the base of the lithoshpere and therefore don't represent heat flow conditions at the present day bed surface.

Other approaches base their models on the few heat flux measurements that are available in Greenland and its surrounding areas. Rezvanbehbahani et al. (2017) and Colgan et al. (2022) combine heat flux measurements with different sets of lithological and tectonic properties of the locations where they were taken and then use machine learning to extrapolate GHF in Greenland based on lithology. Greve (2019) modifies an existing global heat flux model so that a simulation of the Greenland ice sheet reproduces basal temperatures measured at the ice core locations. These estimates based on heat flux measurements suggest a region of very high heat flux in central northern Greenland but do not show indications of the Icelandic plume track (Rezvanbehbahani et al., 2017; Colgan et al., 2022; Greve, 2019). The area of high heat flux in central northern Greenland appears in these estimates because

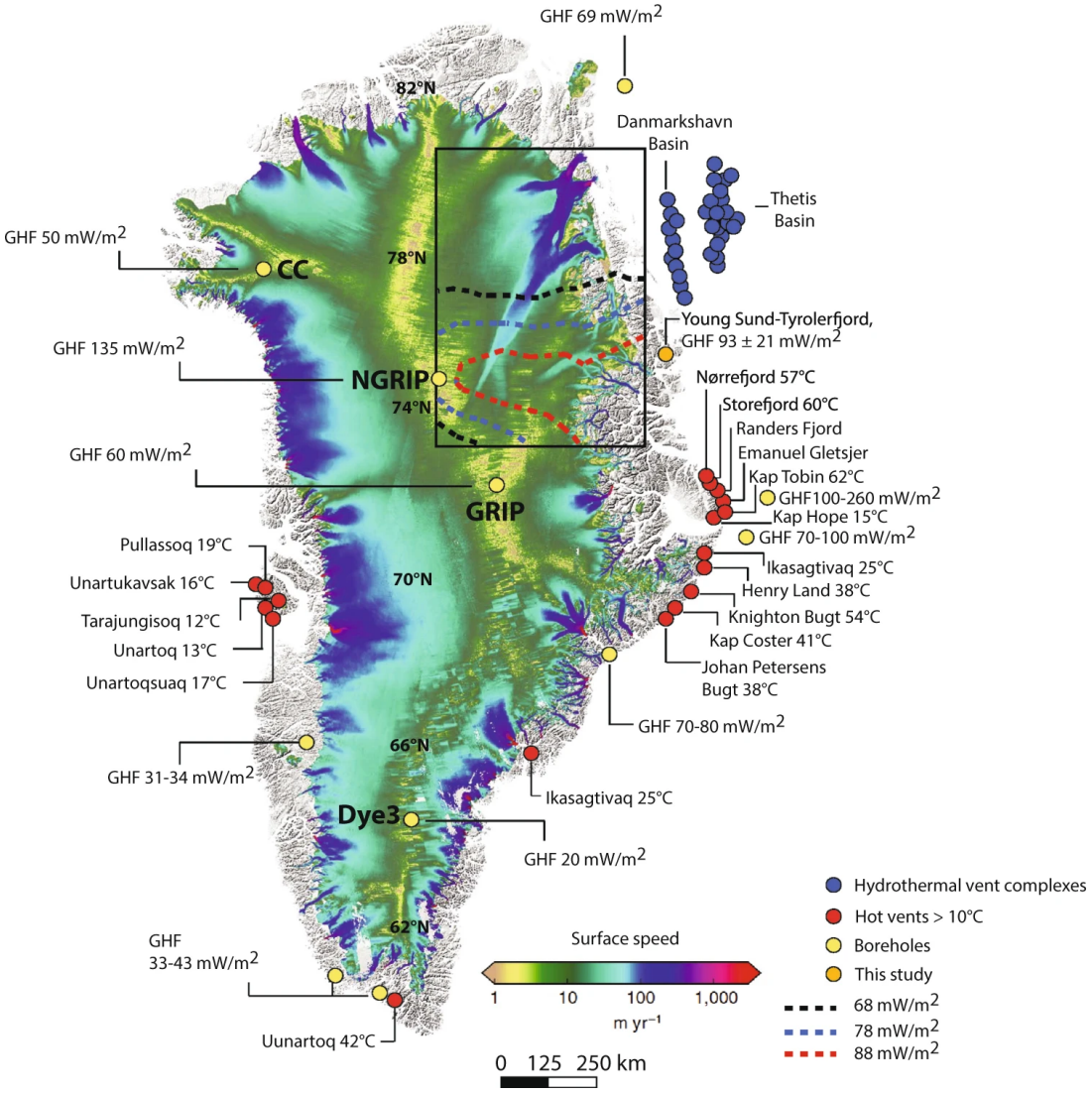

Figure 2.8: Observations of geothermal heat flux in Greenland. Figure from Rysgaard et al. (2018).

of the high heat flux that has been inferred from observed basal melting rates at the bottom of the NGRIP ice core. When removing this data point from the set of heat flux input data, the high heat flux anomaly disappears entirely in the GHF estimate of Colgan et al. (2022).

Alternatively, estimates of heat flux in Greenland can be sourced from global heat flux estimates. Multiple studies have produced such estimates using similar techniques as those described above (e.g., Shapiro and Ritzwoller, 2004; Pollack et al., 1993; Lucazeau, 2019). Interestingly, global GHF estimates often result in highest heat flux along the south-eastern coast of Greenland, whereas studies that produce a Greenland-specific GHF estimate often show particularly low heat flux in the southern tip of Greenland (e.g., Artemieva, 2019; Greve, 2019; Colgan et al., 2022).

Other studies have tried to infer heat flux from observed dynamics of the Greenland ice

sheet and constrained the heat flux values that are required to explain or reproduce them. Fahnestock et al. (2001) inferred basal melt rates of 0.1 ma^{-1} (meter per year) in the onset region of NEGIS from age-stratigraphy analyses in radar profiles. They concluded that exceptionally high heat flux of 970 mW/m^2 (Milliwatts per square meter) is required to produce such high melt rates in that area. Smith-Johnsen et al. (2020) confirmed this estimate in a ice flow modelling study showing that this heat flux value is required to sustain the NEGIS ice stream system. However, heat flux estimates that are based on basal melt rates might be prone to over-estimation as heat from the subglacial hydrological system, hydrothermal circulation, or basal friction may locally increase basal melt (Rogozhina et al., 2016). Smith-Johnsen et al. (2020) themselves note that it is unlikely that the 970 mW/m^2 required to sustain NEGIS are produced by geothermal heat flux alone seeing as the value is unreasonably high (the background median heat flux value is about 60 mW/m^2 in continental crust, Fahnestock et al., 2001; Bons et al., 2021) and suggest hydrothermal circulation as an alternative heat source. Based on seismic analyses of the lithosphere, Artemieva (2019) suggests presently active shallow tectono-magmatic processes in central-eastern Greenland, that might contribute to the high heat flux at NEGIS. Zeising and Humbert (2021) suggest friction in the subglacial water system at NEGIS to be a key contributor to the high heat flux.

2.3 Age structure of the Greenland ice sheet

Throughout their depositional history, ice sheets incorporate gases, particles, and trace elements into their stratigraphic record that allow for absolute dating of the ice layers in ice cores (ice core sites in figures 2.2a, 2.8, Hammer et al., 1978). Some of these proxies show strong seasonal cycles that allow for the counting of annual layers (e.g., classical stratigraphy, density, fabric, deposits of minerals), others can be correlated to certain events (e.g., fall-out of nuclear fission products, ash and solutes from dated volcanic eruptions) or show a time dependent evolution (radioactive material). Absolute chronologies for the Greenland ice cores have been established in this way (as summarized by Johnsen et al., 2001). In sections of the cores where no such data are available or in the lower parts of the cores where annual ice layers are too thin to reliably count, chronologies can be filled-in or extended by age-models that are based on theoretical considerations of ice flow (see section 2.3.1).

The established absolute chronologies can be transferred onto other measures of the stratigraphy of the Greenland ice sheet, such as ice-internal radio reflectors, which are generally assumed to be parallel to the layering of the ice (see for example figure 2.9). For example, Fahnestock et al. (2001) use this approach to compare sections of dated radiostratigraphy in northern Greenland with age-models to infer basal melt rates. MacGregor et al. (2015) correlate dated radiostratigraphy sections from the entire Greenland ice sheet

and produce a three-dimensional estimate of its age-stratigraphy in the top 80 - 90 % of the ice sheet. However, towards the base of the ice the radar reflections of the layers are typically quite weak and ambiguous if visible at all. Therefore, the areal coverage of the MacGregor et al. (2015) age estimate decreases substantially below the top 80 % of the ice sheet and covers only a small area of the actual base of the ice.

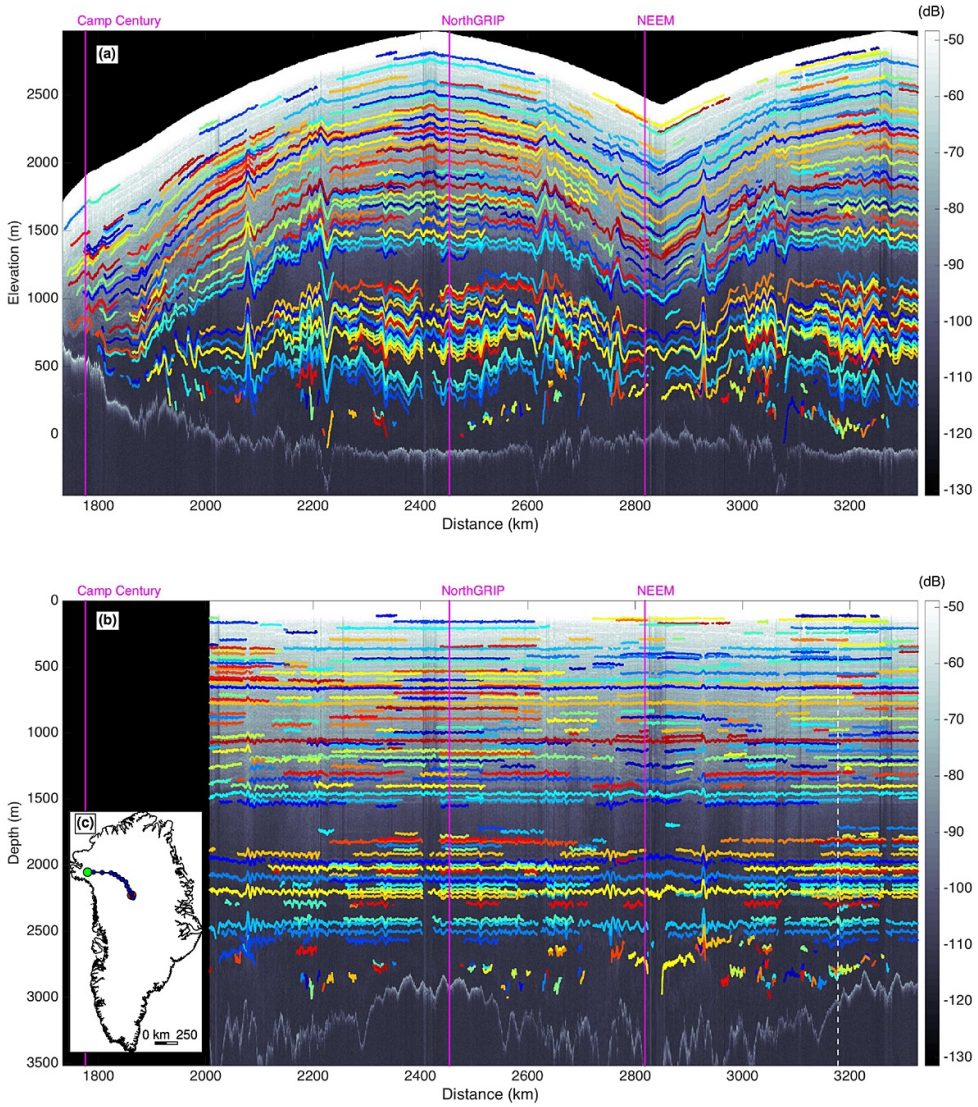

Figure 2.9: Example of traced radiostratigraphy in Greenland, displayed in terms of a) elevation and b) a flattened projection. Profiles intersect with three ice cores, that can be used for absolute dating of the radio traces. Figure from MacGregor et al. (2015).

One of the key unresolved questions in Greenland age stratigraphy is the volume and extent of Eemian ice, i.e., remnant ice from the last interglacial period, roughly from 130 to 115 ka BP (thousands of years ago befor present). The extent of the Eemian ice is an important factor in understanding and simulating the dynamic behaviour of the Greenland ice sheet as this ice is reported to have substantially higher viscosity (i.e., is more rigid) than the overlying younger ice from the last glacial period (Dahl-Jensen et al., 2013; Azuma and

Higashi, 1984; Dahl-Jensen and Gundestrup, 1989; Jacka, 1984).

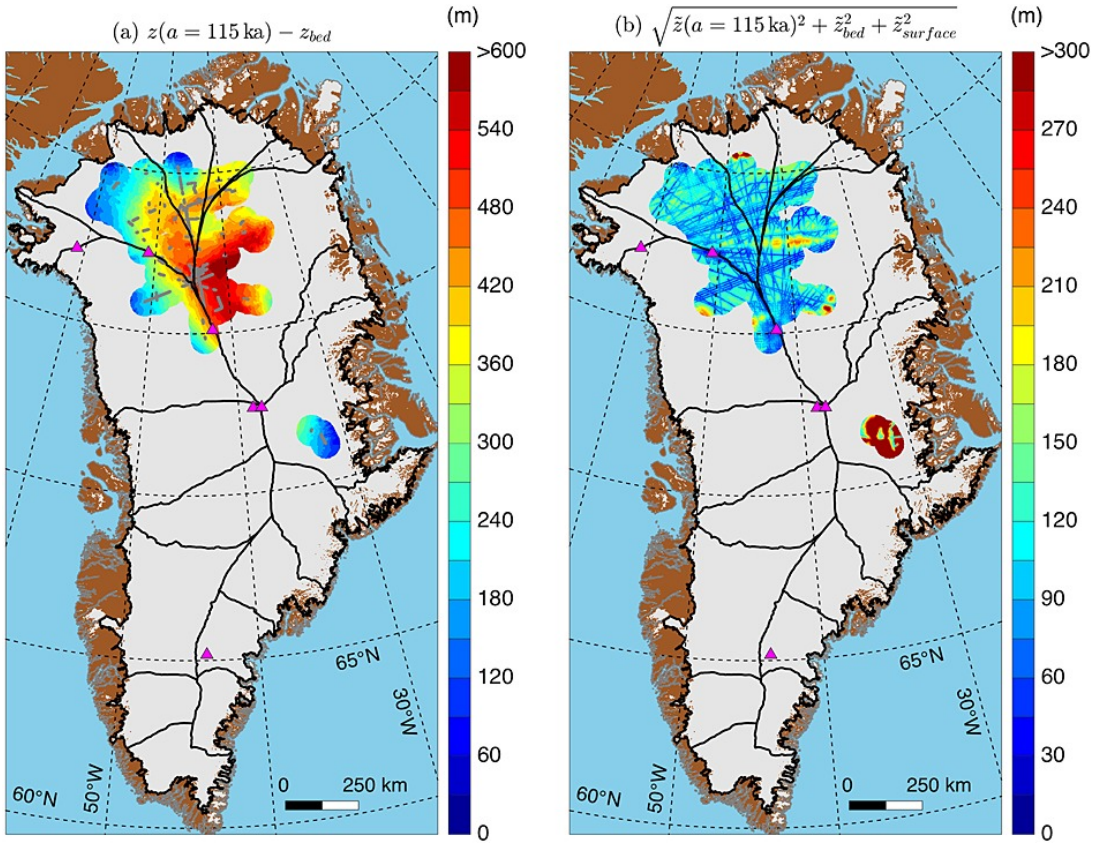

Figure 2.10: Estimated distribution of Eemian ice in Greenland. a) Apparent thickness inferred from radiostratigraphy; b) Error estimate. Figure from MacGregor et al. (2015).

Eemian ice has indeed been found in a disrupted state in the NEEM ice core in northern Greenland (Dahl-Jensen et al., 2013). According to the estimate of MacGregor et al. (2015), Eemian ice should be present in the central part of northern Greenland with maximum thicknesses on the order of 600 m in the vicinity of the North-East Greenland ice stream (see figure 2.10).

2.3.1 Theoretical models of ice age

Theoretical relations between depth and age of ice layers in an ice sheet are based on mathematical considerations of their vertical motion and the deformation they experience as the move through the ice column (as summarized by Cuffey and Paterson, 2010). In the simplest case, at the centre of an ice divide, ice layers move straight down while being vertically compressed and horizontally stretched (figure 2.11). Vertical motion and compression are caused by the increasing overburdening load exerted by the subsequently deposited layers. The current depth of an ice layer deposited at some time in the past is determined by the sum

of the thicknesses of the overlying younger layers. In other words, it is determined by the subsequent accumulation and the cumulative strain, which can alternatively be expressed as the history of vertical velocity of the ice layer.

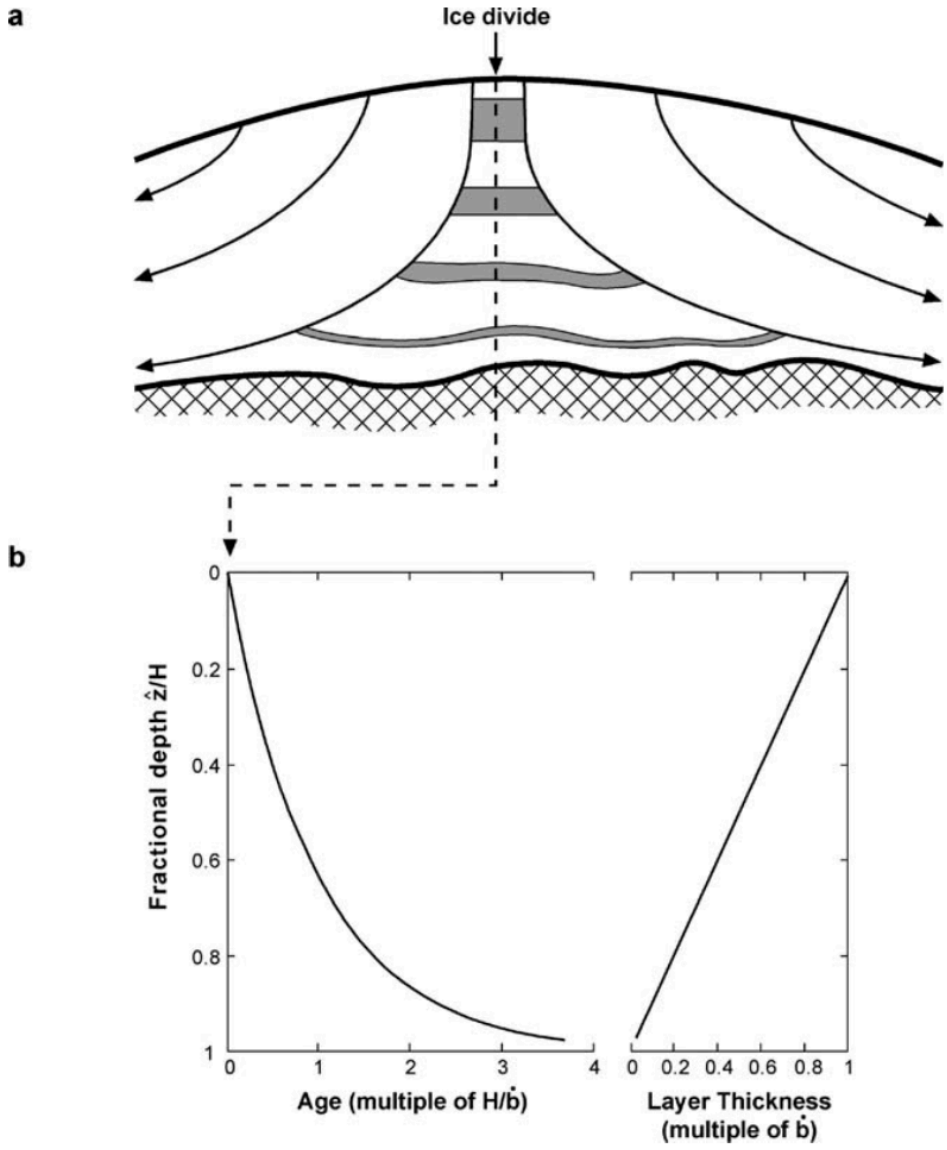

Figure 2.11: Concept of mathematical age models. a) Schematic of the vertical motion and deformation of ice layers at an ice divide. b) Evolution of age and thickness of ice layers with depth. Figure from Cuffey and Paterson (2010).

As surface accumulation varies in time, strain and vertical velocity may also vary throughout the history of an ice layer. Several models exist that circumvent this issue by making simplifying assumptions.

Nye (1963) assumes that melting at the base is negligible and the vertical strain rate is uniform along any vertical line in the ice, and thus relates the current thickness of an ice

layer to its current depth, its initial thickness, and the thickness of the ice sheet at the time the layer was deposited. Ice layer thicknesses decrease with depth but stay proportional to their initial thickness. If one further assumes the ice sheet to be in steady state with constant surface accumulation and thickness, the age of an ice layer at a given depth in the ice sheet can be calculated simply from its depth in the ice sheet, the thickness of the ice sheet, and the surface accumulation rate.

The incompressibility of ice requires that vertical compression must be counterbalanced by horizontal stretching. Conversely, if the base of the ice is frozen to the bed, horizontal motion is not possible and vertical strain rates decrease to zero towards the base, implying shearing of the ice near the base. Dansgaard and Johnsen (1969) adjusted the Nye-model by introducing a basal shear layer. In the upper part of the ice sheet, the model is identical to the Nye-model assuming uniform vertical strain, but below a certain depth, the ”kink-hight”, vertical (and horizontal) strain decreases linearly to zero.

Generally, the Dansgaard-Johnsen model results in faster increase of age with depth than the Nye-model, although the depth of the kink-hight has great influence on the age evolution in the lower part of the ice and must be adjusted to each respective case. However, since both the Nye-model and the Dansgaard-Johnsen model assume zero basal melt, meaning that no ice is removed at the base, vertical velocities necessarily decrease to zero at the base and both models will hence predict infinite age at the very base of the ice.

Trying to fit age models to dated radar reflectors in Greenland, Fahnestock et al. (2001) find that in some areas neither the Nye-model nor the Dansgaard-Johnsen model are able to produce acceptable fits. Fahnestock et al. (2001) solve this issue by modifying the Nye-model to allow for basal melt. This effectively lowers the vertical strain rate and ages increase slower compared to the Nye-model. However by incorporating basal melt, vertical velocities no longer decrease to zero at the base. This means that in contrast to the Nye and the Dansgaard-Johnsen models, the Nye+melt model is able to produce a finite estimate of the age of the basal ice (see also section 3.2.1).

2.3.2 Key concepts of isotope stratigraphy

The water that makes up the ice in glaciers and ice sheets consists of oxygen and hydrogen atoms which naturally occur as heavier and lighter stable isotopes (as summarized by Fischer et al., 2021; Kendall et al., 2014). The two main isotopologues (molecules of same atomic composition but different isotope content) of water are $H_2^{16}O$ (which is lighter) and $H_2^{18}O$ (which is heavier) with relative abundances of 99.76 % and 0.201 % respectively.

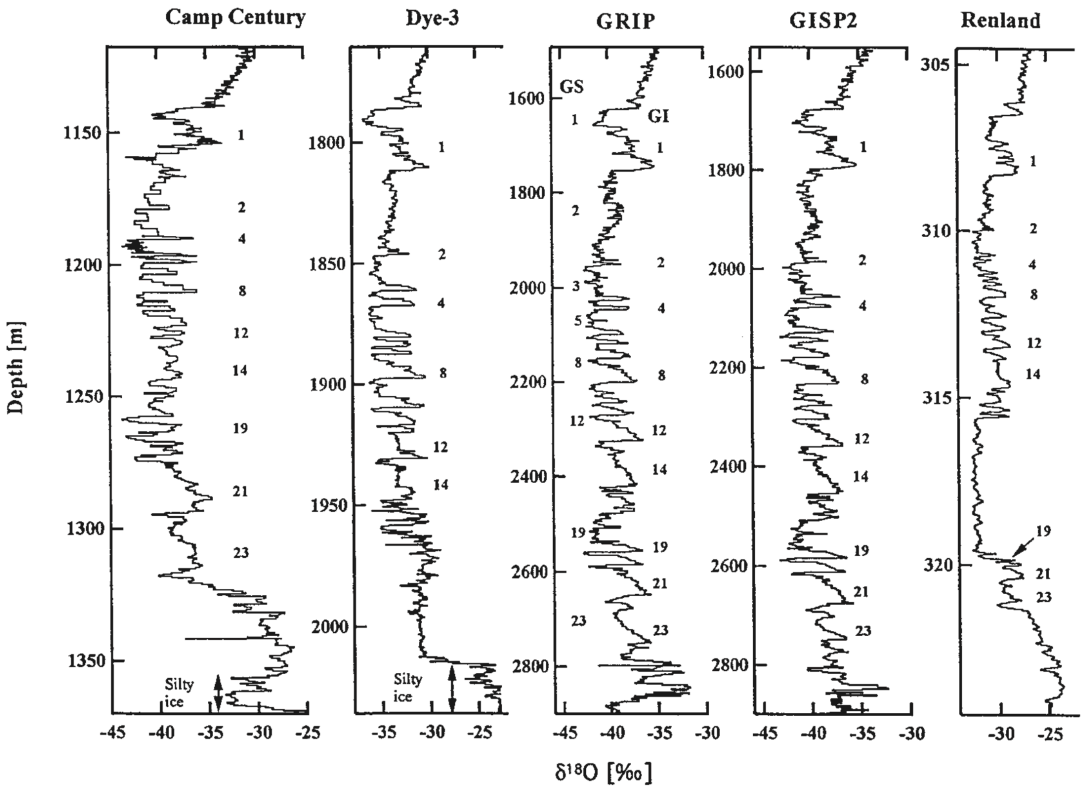

Figure 2.12: Isotope records (d18O) from five Greenland ice cores. Figure from Johnsen et al. (2001).

Because of their different masses, these isotopologues behave slightly differently during phase transitions (evaporation, condensation, freezing) which results in a slight change in their relative abundance in the water after the phase transition compared to before. This is referred to as isotope-fractionation.

The abundances of the isotopologues are measured as the ratio of the heavier isotope to the lighter isotope, $R^{18} = {}^{18}O/{}^{16}O$. Isotope ratios are determined relative to those in a standard sample, which for water typically is Vienna Standard Mean Ocean Water (VSMOW), and are expressed in permille [‰] using the δ-notation

$$\delta^{18}O = \frac{R^{18}}{R^{18}_{VSMOW}} - 1$$

in which R^{18} is the isotope ratio of the sample and R^{18}_{VSMOW} is the isotope ratio of the VSMOW standard. Positive δ-values indicate the sample is enriched in the heavy isotope compared to the standard, negative values indicate the sample is depleted of the heavy isotope compared to the standard.

The δ^{18}O value of ice is routinely measured in ice cores across their entire length. Figure 2.12 shows the δ^{18}O values of five Greenland ice cores (Johnsen et al., 2001). All of

them show δ-values in the range of -45 to -25 ‰ for the ice. Figure 2.13 shows a comparison between the isotope record at the GRIP and NGRIP ice cores. They show very similar evolution of isotope values over time, despite their geographical distance of 325 km. This is because the fractionation process that creates the variations in isotope composition of the water depends intimately on temperature. The main control of variations in isotope values is therefore the global climate, implying that isotope values in all Greenland ice cores show similar behaviour over the lengths of their records.

In the δ^{18}O record of the NGRIP ice core (red curve in figure 2.13 Andersen et al., 2004), glacial and interglacial periods can be clearly distinguished showing large differences on the order of several permille. Above 1500 m depth, δ^{18}O are quite stable around -36 ‰ showing only little variability over depth. This corresponds to the current Holocene interglacial period, that began at around 11.7 ka BP (Walker et al., 2008, 2009). The second to last interglacial period, the Eemian which lasted between 129 and 116 ka BP (CAPE-Last Interglacial Project Members, 2006; Bazin et al., 2013), shows slightly higher but still similar isotope values of around -32 ‰ visible at the very bottom of the NGRIP core. In the ice core section between the Holocene and Eemian, corresponding to the last glacial period, the Weichselian, δ^{18}O values are generally between -40 and -44 ‰. There are short excrusions in isotope values up to around -36 ‰, but in general the glacial ice shows much lower δ^{18}O values than the interglacial sections of the ice core.

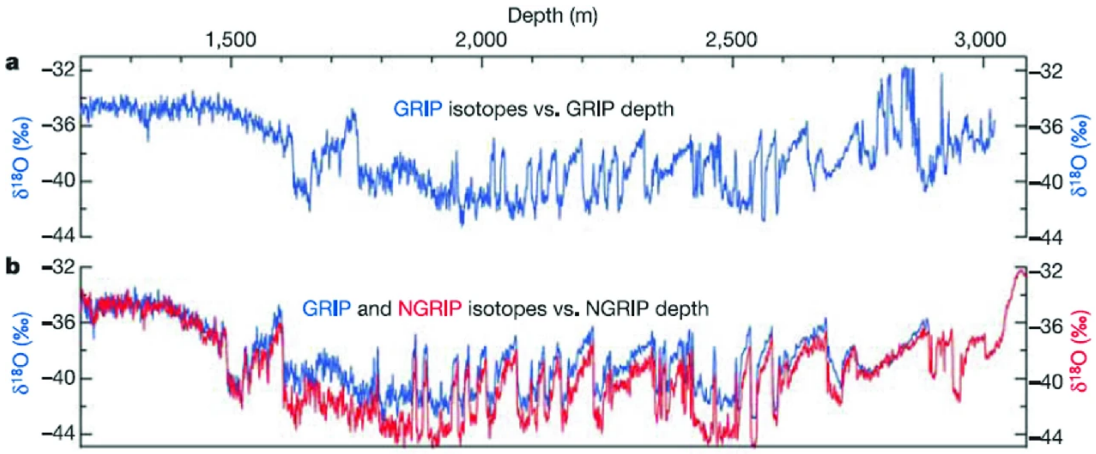

Figure 2.13: Comparison of d18O records from GRIP and NGRIP ice cores. a) GRIP isotope record; b) age-matched GRIP and NGRIP records. Figure from Andersen et al. (2004).

However, although climate is the main control of the overall evolution of the isotope values in the Greenland ice cores, the δ^{18}O curves of GRIP and NGRIP displayed in figure 2.13 do show a systematic difference of about 1-2 ‰ which can be attributed to the geographical location of the core sites relative to each other (Andersen et al., 2004). Dif-

ferent locations may receive precipitation from different source areas. As the seas around Greenland show large differences in temperature, evaporation will lead to different degrees of fractionation and hence different isotope compositions of the resulting precipitation. As the vapour in clouds condensates, isotope composition will again undergo fractionation and the water vapour in the cloud is depleted of the heavier isotope. As the formation of rain or snow in the cloud goes on, fracionation continues and the cloud is being more and more depleted of the heavier isotope. The resulting precipitation will thus show more and more negative δ^{18}O values the more fractionation the cloud has already experienced. This is referred to as Raileigh-fractionation (Kendall et al., 2014). Since precipitation events are controlled by changes in altitude of the cloud, regions that are higher up (which in the case of Greenland also implies farther inland) receive lighter precipitation than regions further down (or nearer to the coast).

In the isotope record of an ice core however, there is yet another factor that needs to be taken into account. Since ice moves, the ice that can be found in an ice core has not necessarily been deposited at the same location, but rather somewhere farther upstream closer to the ice divide. This effect is more pronounced for deeper sections of an ice core, as figure 2.14 shows. For example, assuming the basal ice at EGRIP (East Greenland ice core porject) to be more than 100 kyrs old, Gerber et al. (2021) estimate the source region for that ice to be within 50 km of the ice divide, even though EGRIP itself is located over 300 km away from the ice divide. They conclude that under these circumstances the basal ice at EGRIP would have been deposited under similar conditions as the ice at GRIP and NGRIP. Reeh et al. (2002) analyzed the δ^{18}O records of a number of ice cores collected around the margin of the Greenland ice sheet. Some of them extend far back in time, covering the last glacial period and even reaching into the Eemian interglacial towards their bases. Reeh et al. (2002) likewise argue that ice of this age would have been deposited near the ice divide and subsequently transported to its current location.

2.4 Subglacial hydrology

There are two sources that contribute water to the glacial water system. Firstly, the glacial ice itself can produce meltwater at the surface, the interior, and the bed of the glacier. Secondly, water can enter from external sources in the form of rain on the surface or groundwater influx from below (Benn and Evans, 2010). Once the water is at the base (either being produced/inserted there or, in the case of surface water, being conducted there through crevasses and moulins) it will enter the subglacial drainage system and be evacuated from the glacial environment. The network of subglacial conduits that make up the drainage system can be categorized into two main types. Efficient and inefficient drainage systems (as

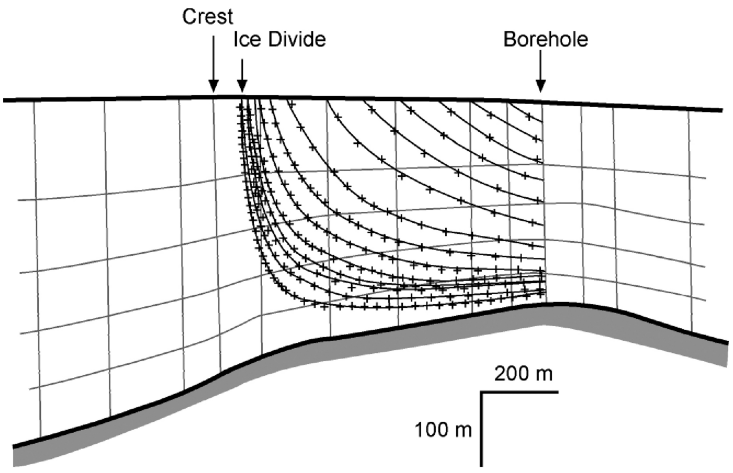

Figure 2.14: Schematic of the flowpaths of ice in an ice sheet and where the ice in a borehole would have originated at the surface. Figure from Cuffey and Paterson (2010).

summarized by Flowers, 2015; Benn and Evans, 2010).

The efficient drainage system is comprised of different types of channels that are either carved upwards into the ice (Röthlisberger-channels) or downwards into the bed (Nye-channels; see figure 2.15). These structures typically form during the melt season when water input to the base is high and evacuate water quickly from the subglacial environment. The channels remain open as long as water flux though them is high enough that the melt along the channel walls from the released energy counterbalances the slow collapse of the channel through ice creep. When the water flux subsides, the channels will slowly close.

Thin water films, interconnected cavities, and flow through the basal sediment are part of the inefficient drainage system (see figure 2.15). This drainage system is prevailing when the water input to the base is low as the capacity for water transport is very limited. Other than the channels of the efficient drainage system, these structures are not invoked by the water flux but rather the subglacial environment itself. Water films form at the ice-bed interface in regions where the basal ice is at pressure-melting point, cavities form on the lee-side of bumps in the bed where the normal stress exerted by the moving ice is minimal and water pressure can exceed ice overburden pressure, and groundwater flow is enabled by the presence of sediment.

The components of the subglacial drainage system evolve dynamically, channels and cavities open and close depending on water availability and ice flow. While several hydrological models exist that can be coupled to ice flow models and simulate the transient behaviour of these drainage components (e.g., de Fleurian et al., 2014; Werder et al., 2013; Hewitt, 2011; Sommers et al., 2018), many studies use a simpler approach to modelling subglacial water routing (e.g., Karlsson and Dahl-Jensen, 2015; Karlsson et al., 2021; Chu

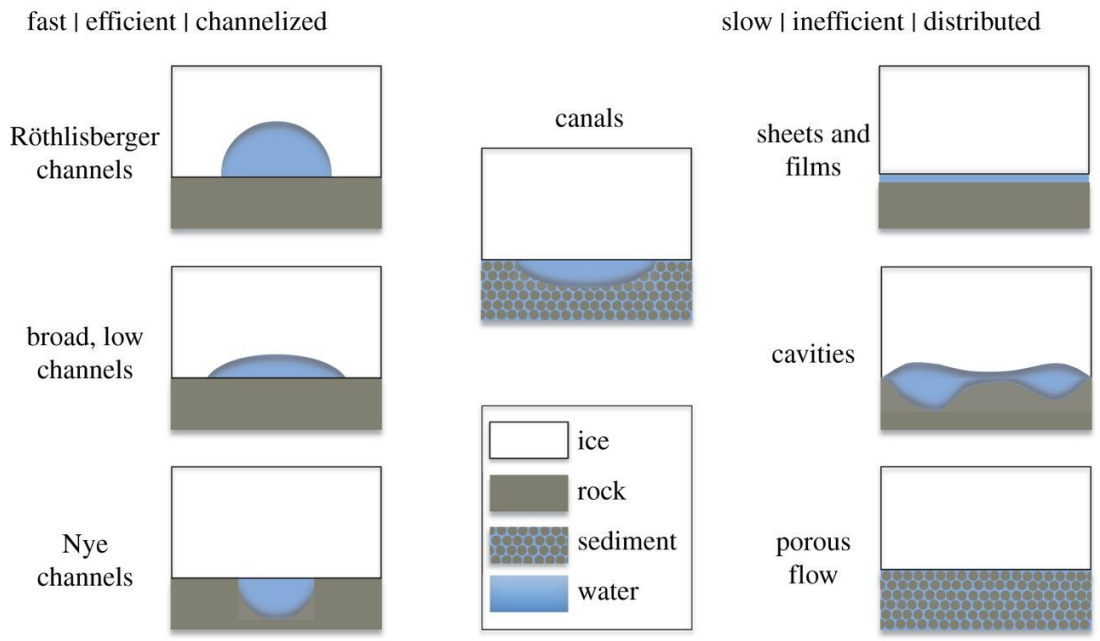

Figure 2.15: Examples of types of subglacial conduit systems, grouped in efficient (left) and inefficient (right). Figure from Flowers (2015).

et al., 2016; Lindbäck et al., 2015; Rippin et al., 2003).

Generally, water moves along gradients in hydropotential. The subglacial hydropotential Φ can be calculated as the sum of the elevation potential of the water and its pressure (Shreve, 1972)

$$\Phi = \rho_w \, g \, z_b + p_w \tag{2.6}$$

in which p_w is the water pressure, ρ_w is the density of water, g is the gravitational acceleration, and z_b is the elevation of the bed. Equation 2.6 is technically only true inside subglacial conduits, but for the purpose of modelling can be assumed to be valid everywhere in and under the ice (Shreve, 1972).

The water pressure p_w and the ice overburden pressure p_i are connected by the effective pressure N. The effective pressure is defined as the difference between ice overburden pressure and water pressure, $N = p_i - p_w$. The water pressure can thus be formulated as a fraction of ice overburden pressure by introducing a factor f, which is the ratio of water pressure to ice overburden pressure, $f = p_w/p_i$, and is called the floatation fraction (e.g., Willis et al., 2012; Banwell et al., 2013; Chu et al., 2016).

$$p_w \;=\; p_i - N \;=\; f \, p_i \;=\; f \, \rho_i \, g \, H \tag{2.7}$$

with H denoting the thickness of the ice which can also be expressed as the difference between surface elevation z_s and bed elevation z_b, $H = z_s - z_b$. Substituting p_w in equation

2.6 with 2.7 gives

$$\Phi = \rho_w \, g \, z_b + f \, \rho_i \, g \, (z_s - z_b) \tag{2.8}$$

From the definition of f and equation 2.7 it is clear that $f = 1$ indicates that water pressure is equal to ice overburden pressure, for $f < 1$ water pressure is lower than ice overburden pressure, and for $f > 1$ it is higher. A natural upper boundary of $f = 1.1$ arises from the higher density of water compared to ice, so that fractures or moulins in the ice that are filled with water would produce basal water pressures above ice overburden pressure (Chu et al., 2016). Studies of borehole water pressures around the margin of the Greenland ice sheet seem to suggest that floataion fraction quickly rises to values above 0.9 and close to 1 within 50 km of the ice sheet margin and remain at high values farther inland (Meierbachtol et al., 2013; Andrews et al., 2014). However, the same kind of studies do not exist for the interior of Greenland where only the boreholes of the few deep ice cores reach all the way to the base of the ice sheet, so the floatation of the bulk of the Greenland ice sheet is still an open question.

In reality, f will vary in time and space. In modelling studies however, it is often assumed to be uniform (e.g., Willis et al., 2012; Rippin et al., 2003; Banwell et al., 2013). Chu et al. (2016) and Lindbäck et al. (2015) used equation 2.8 to study the effects of basal water pressure on the spatial structure of the subglacial drainage system by simulating subglacial drainage systems of glaciers in Greenland for different values of f. According to these model studies, the floatation fraction has a substantial influence on the delineation between catchment areas of adjacent subglacial water outlets, showing that for certain areas the basal water will flow to one outlet for lower floatations and to a different outlet for higher floatations.

Chapter 3

Data and Methods

Inferring geothermal heat flux from stable isotopes is based on a conceptual influence of spatial variability in GHF distribution on the stable isotope composition of the basal meltwater underneath an ice sheet (see figure 3.1). As described in section 2.1.3, geothermal heat flux excerts a large control on the dynamic behaviour of ice sheets as it influences both the flow dynamics of the ice as well as the rate of meltwater production at the ice-bed interface. The spatial distribution and magnitude of basal melting is therefore dependant on the spatial distribution and magnitude of the GHF. Higher heat flux leads to higher melt rates and larger melt areas, lower heat flux leads to lower melt rates and smaller melt areas.

The produced basal meltwater flows along the bed through the subglacial drainage system following the gradient in subglacial hydropotential. On its journey from the interior of the ice sheet to its margin it will converge into streams that leave the subglacial water system through defined outlets at the ice margin. As the geothermal heat flux controls the size of the basal melt area, the size of the area from where basal meltwater drains towards each outlet (the drainage area) will also change for different distributions of GHF.

The melting of the ice at the base of the ice sheet transmits the isotopic composition of the ice into the basal meltwater system. Since the isotopic composition of the Greenland ice sheet is not uniform and differs substantially between different ice layers (see section 2.3.2), meltwater produced from different ice layers will have accordingly different isotopic composition. Different extents and magnitudes of basal melt will change the amount of meltwater that layers of different isotopic composition can contribute to the basal water system. The isotopic composition of the composite meltwater that exits at the outlet is a mixture of the isotopic composition of all the meltwater produced in the drainage area of that outlet. Hence, through the control of GHF on basal melting, the isotopic composition of the draining basal meltwater will be different for different distributions of heat flux.

To test this concept, I will simulate the basal meltwater production in Greenland and the

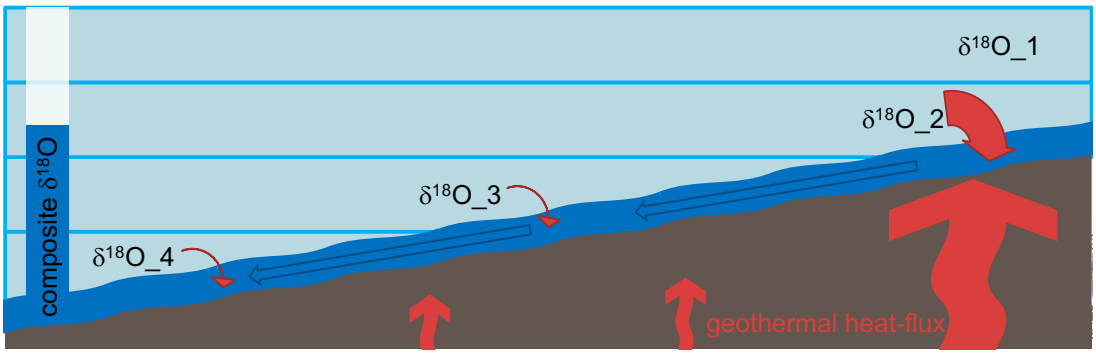

Figure 3.1: Conceptual relationship between geothermal heat flux and isotopic composition of basal meltwater (see text for detailed explanation). Light-blue horizontal layers indicated ice layers with different isotope composition d18O_1 to d18O_4. Brown area indicates bedrock. Wavy upwards-pointing arrows indicate geothermal heat flux with larger arrows indicating larger heat flux. Curved downwards-pointing arrows indicate basal meltwater flux from the ice to the basal meltwater layer, larger arrows indicating larger flux. Basal meltwater layer indicated by dark blue layer between ice and bedrock with arrows indicating flow direction. White and blue vertical bar on left side indicates a borehole in which basal meltwater with a mixed isotope signal collects.

associated stable isotope composition of the basal meltwater based on different estimates of geothermal heat flux. This will allow me to constrain the impact of GHF on the isotopic composition of the basal meltwater and hence test the ability of stable isotope analysis in predicting GHF distribution.

The basal meltwater production is simulated as a steady state response to different geothermal heat flux estimates with the help of a three-dimensional numerical model of the Greenland ice sheet. The age of the basal ice is estimated based on a mathematical depth-age relation (see section 2.3.1) as a proxy for the isotopic composition of the basal ice (see secion 2.3.2). The isotopic composition of the basal ice is extrapolated from the NGRIP-δ^{18}O record and its correlation to the climate record of the Antarctic Vostok ice core. The movement and mixture of the water in the subglacial drainage system will be modelled based on the Shreve-hydropotential (see section 2.4). The δ^{18}O values of the basal meltwater are treated as a conservative tracer in the hydrological system which allows them to mix in accordance with the water movement through the drainage. Finally, the composite isotopic composition of the mixed basal water is extracted at a number of defined locations and variability between the different GHF-scenarios is analyzed.

Details for each step of the methodology are provided in the following sections. Section 3.1 describes the ice-sheet model and the set-up of the numerical experiments. Section 3.2 outlines the procedure to estimate the age of the basal ice and its isotopic composition. Section 3.3 describes the routing algorithm used to model the subglacial drainage and mixing of isotope values. Finally, section 3.4 describes the analysis of the modelled basal meltwater

isotopic composition.

3.1 Simulating basal meltwater production in Greenland

3.1.1 Ice sheet model and setup

The Ice-sheet and Sea-level System Model (ISSM) (Larour et al., 2012; Seroussi et al., 2013) is a finite-element, three-dimensional, thermo-mechanically coupled ice-flow model that simulates ice-flow by solving the stress- and energy-balance equations. The model used here was provided by Martin Rückamp from the Bavarian Academy of Sciences, Germany[1] (Rückamp, 2022). It is similar to the model used in Seroussi et al. (2013). It uses the Higher-Order (HO) approximation of the momentum balance equations (Blatter, 1995; Pattyn, 2003) which simplifies the Stokes equations by assuming that horizontal gradients of vertical velocities are negligible compared to vertical gradient of horizontal velocities and that bridging effects are negligible. This effectively decouples vertical and horizontal velocities in the flow-model (Seroussi et al., 2013). In order to reproduce present-day surface velocities, the M1QN3 inversion algorithm (Gilbert and Lemaréchal, 1989) is used to infer the basal friction coefficient. A dataset of observed surface volocities with Greenland wide coverage is used as target in the inversion (Joughin et al., 2016; JOUGHIN et al., 2018).

Since the purpose of the model is to simulate basal meltwater production, it is necessary to simulate the thermal regime using a formulation based on enthalpy instead of temperature (Aschwanden et al., 2012; Kleiner et al., 2015; Rückamp et al., 2020). In this formulation, heat capacity and conductivity are variable which enables the model to simulate liquid water content in the ice and hence phase transitions between ice and water. This further necessitates the use of a rheology formulation that accounts for both ice temperature and liquid water content since liquid water in the ice has significant impact on the flow behaviour (Greve and Blatter, 2009). Here the formulation of Lliboutry and Duval (1985) is used.

The model domain covers the entire glaciated area in Greenland. The three-dimensional irregular triangular mesh consists of over 1.8 Million prismatic elements on 15 vertical layers, each layer consisting of over 130 000 triangular elements. Horizontal mesh resolution is anisotropic on the order of 10 km for most of the ice sheet and increased in areas of high

[1] Attempts to construct my own model of the Greenland ice sheet ultimately failed due to time constraints, which is why I had to resort to external sources. However, after the several months that I spent tweaking model parameters, trying different surface data sets for the initial conditions, reading up on different stabilization terms, testing different combinations of solvers, and running dozens and dozens of sometimes even successful stress balances, inversions, thermal steady states, and transients I was at least able to use Martin's model without any issues, despite having no prior experience in ice-sheet modelling at all.

surface velocity around the ice margin. The vertical resolution between the layers increases towards the base where temperature gradients and vertical shearing are concentrated (e.g., Seroussi et al., 2013). Eight of the 15 layers are concentrated in the bottom 25 % of the ice sheet, the vertical distance between the bottom layers is on the order of meters. The resolution of the thermal regime is further increased by using P2-elements in the vertical that are able to capture exponential vertical temperature gradients rather than linearly approximating them (Cuzzone et al., 2018). Bed and surface topographies are taken from BedMachine V4 (Morlighem et al., 2017).

3.1.2 Numerical experiments

The basal meltwater production is simulated as a steady-state response to different geothermal heat flux fields. In total, 14 experiments are run, seven of which with GHF estimates from published literature and seven with synthetic heat flux maps that are described in section 3.1.3. For each experiment, the initial state of the model is updated with the data of the respective GHF field. All other variables and parameters remain unchanged and are the same between the different experiments. The experiments are run as thermo-mechanical steady state simulations. The steady state solver alternates between solving the stressbalance with coupled friction inversion and solving the energy balance for the thermal regime. Ice hardness is continuously updated according to the rheology before each iteration. This is repeated until both ice velocity and temperature fields converge on a solution. The solution is the steady-state response of the coupled velocity and temperature fields to the respective geothermal heat flux field in each experiment.

3.1.3 Geothermal heat flux data

This section describes the heat flux data sets that were used for the different experiments of the basal meltwater simulation (see section 3.1.2. The GHF data sets shown in figure 3.2 are taken from published literature and are commonly used in modelling studies of the Greenland ice sheet (e.g., Rogozhina et al., 2012; Smith-Johnsen et al., 2020), hereafter referred to as *GHF estimates*. The data sets shown in figure 3.3 are synthetic heat flux maps constructed to isolate and analyze the influence of key features of the GHF estimates, hereafter referred to as *synthetic GHFs*.

Colgan22, Colgan22NG - Similar to the method and result of Rezvanbehbahani et al. (2017) (not considered here), Colgan et al. (2022) trained a machine-learning algorithm with 419 point measurements of geothermal heat flux. Since heat flux measurements in Greenland are only available at the few ice core sites in the interior of the ice sheet and at few locations at the exposed bedrock around the coast, Colgan et al. (2022) included a portion of the surrounding oceans into the training data set as these areas are show much higher density

in heat flux measurements. The algorithm correlates the heat flux observations to a number of geopyhsical and tectono-lithological datasets to extrapolate the individual measurements into two GHF maps of full areal coverage in Greenland and surrounding offshore areas.

The authors considered the exceptionally high observed heat flux at the bottom of NGRIP (130 mW/m^2) to be a likely outlier and hence constructed two GHF scenarios in their machine-learning algorithm, one trained with (*Colgan22NG*) and one without (*Colgan22*) this data point. Compared to other existing estimates of Greenland GHF, both GHF maps show uncommonly low heat flux values of 40 - 50 mW/m^2 in the vast majority of the Greenland area with lowest values in the South and mean values of 44 mW/m^2 (Colgan22) and 48 mW/m^2 (Colgan22NG). Only Colgan22NG shows higher heat flux values in the NGRIP area in the central northern part with values of 70 - 90 mW/m^2.

Greve19 - Greve (2019) modified the gobal heat flux estimate of Pollack et al. (1993) at the five Greenland ice core locations (NEEM, NGRIP, GRIP, Camp Century, Dye3) and three coastal bedrock borehole locations such that a paleoclimate spinup simulation of the Greenland Ice Sheet reproduces the basal temperatures measured at the five ice core locations.

This estimate shows a pronounced hotspot of over 130 mW/m^2 at the NGRIP ice core location in central northern Greenland corresponding to observations there. The surrounding areas in northern Greenland show heat flux values between 60 and 90 mW/m^2, the southern tip of Greenland shows lower values between 30 and 40 mW/m^2.

Martos18 - Martos et al. (2018) estimated the Curie depth in Greenland through spectral analysis of the crustal magnetic anomaly field. The Curie depth is the depth at which the minerals in the crust lose their ability to sustain magnetization because of increasing temperature. They subsequently constructed a thermal model of the crust between the estimated Curie depth and the base of the ice sheet and simulating heat flux through the Greenland, thus constraining GHF values at the bed surface.

The GHF map shows an elongated area of elevated heat flux of 65 to 75 mW/m^2 that crosses the island in a straight line from north-east to south-west. Martos et al. (2018) interpret this a the remnant of the passage of the Icelandic hotspot. The area on the southern tip of the island also shows elevated heat flux of similar values. The remaining areas show lower heat flux values of around 40 to 50 mW/m^2. Overall, heat flux values show less variability compared to other GHF estimates and the spatial distribution is visibly more homogeneous.

FMaule09 - Similar to Martos et al. (2018), Fox Maule et al. (2009) modeled the thermal structure of the crust in Greenland based on estimates of the Curie-depth and simulated heat flux through the crust to the surface. Their estimate of the Curie-depth is however based on an estimate of the thickness of the magnetized part of the upper crust in Greenland

which they obtained by reconstructing Earth's magnetic field in a model.

The average heat flux in their estimate is 68 mW/m^2. It is higher in the southern and south-eastern part of Greenland with values between 60 to 80 mW/m^2. The central part of northern Greenland shows slightly lower values of 50 to 60 mW/m^2. Highest values can be found at Blosseville Kyst with 90 to 110 mW/m^2. Lowest heat flux values below 50 mW/m^2 are located towards the north-western border. This GHF estimate shows more spatial heterogeneity, larger value range, and surprisingly different spatial distribution of heat flux values compared to the estimate of Martos et al. (2018), despite similar methodology.

Shapiro04 - Shapiro and Ritzwoller (2004) produced an estimate of global GHF by relating existing global heat flux measurements to the seismic structure of the underlying crust and upper mantle. They used a global model of seismic shear velocities to extrapolate GHF values to areas where no measured data exist based on their structural similarity to areas with observed heat flux.

In Greenland, this GHF estimate shows highest heat flux along the south-western coast and across the southern tip of Greenland with values ranging between 70 and 80 mW/m^2. The majority of the remaining area shows low heat flux values below 50 mW/m^2 with lowest values in the central northern part of Greenland. This is in direct contrast to the estimates of, e.g., Colgan et al. (2022) and Greve (2019) who estiamted particularly high heat flux in this region. This is because the heat flux data set used by Shapiro and Ritzwoller (2004) does not include the heat flux observations from the ice cores in the interior of Greenland, but only observation from a few locations around the coast. The high observed heat flux at NGRIP is thus not considered in their structural similarity function.

Lucazeau19 - The global heat flux estimate of Lucazeau (2019) is an update to the estimate of Pollack et al. (1993) and based on almost 70,000 globally distributed heat flux measurements. Unlike the method of Shapiro and Ritzwoller (2004), the estimate is produced by relating the measured heat flux values to several characteristics of the respective measurement locations (instead of only seismic structure) including seismic tomography, lithosphere thickness, Curie point depth, free air anomalies, topography, and distance to different tectonic features. These characteristics are then used as predictors in a similarity method to extrapolate heat flux values to areas where no measured data exist.

However, their data set of global heat flux observation contains only a single data point in the interior of Greenland. The resulting GHF map is thus still similar to the estimate of Shapiro and Ritzwoller (2004) with highest heat flux values of around 80 mW/m^2 along the south-eastern coast and in the southern tip of Greenland, but otherwise fairly homogeneous GHF distribution. Heat flux in the northern part of Greenland is slightly higher than in the estimate of Shapiro and Ritzwoller (2004) with values around 60 to 70 mW/m^2.

GHF01-07 - In addition to the existing estimates of Greenland GHF, some ISSM simu-

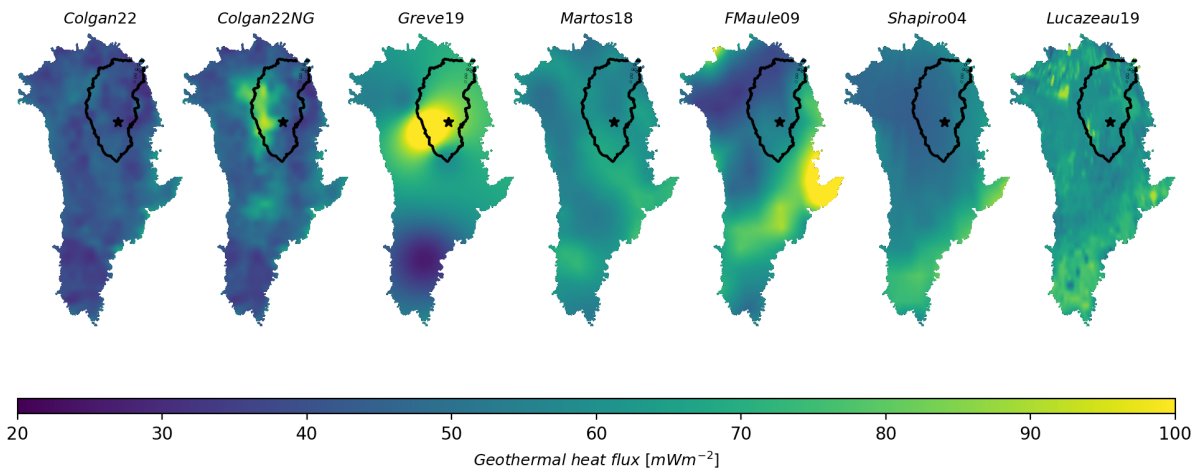

Figure 3.2: Heat flux maps of the GHF estimates. Heat flux is cut off at 100 mW/m2 but exceeds that value in Greve19 and FMaule09. Red star indicates location of EGRIP.

lations have been performed with synthetic GHF distributions. These synthetic GHF maps (figure 3.3) are based on the published GHF estimates but are much simpler in their nature and designed to study individual features of the GHF estimates.

Three main scenarios have been designed. A uniform GHF is simulated to constrain a reference isotopic composition of the basal water resulting from a GHF without any spatial variability. To isolate effects of some of the most distinct and common features of the GHF estimates, two GHF anomaly scenarios are superimposed onto the uniform distribution: A high GHF anomaly in central northern Greenland akin to the Greve (2019) and Colgan et al. (2022) GHF estimates as well as a gradient of increasing GHF from North-West to South-East similar to the GHFs by Shapiro and Ritzwoller (2004), Lucazeau (2019), and to an extent Fox Maule et al. (2009). These three scenarios have been realized in two sets, one with a uniform background GHF of 70 mW/m2 and one with a background of 40 mW/m2, which roughly covers the range of mean GHF values of the GHF estimates. Additionally, one GHF map has been designed with a higher GHF in the southern half of Greenland, to investigate whether heat flux variations in the south have an influence on the ice sheet in the north, i.e., whether GHF variations in one ice sheet drainage basin have a detectable influence on the ice sheet in another drainage basin.

3.2 The isotopic composition of basal ice

The isotopic composition of the basal ice is modelled based on its relationship to the age of the ice that has been established in the Greenland ice cores (see section 2.3.1). The age of the basal ice can be modeled by applying the Nye+melt age model (Fahnestock et al., 2001), described in detail in section 3.2.1 (see section 2.3.1 for more general information on age models).

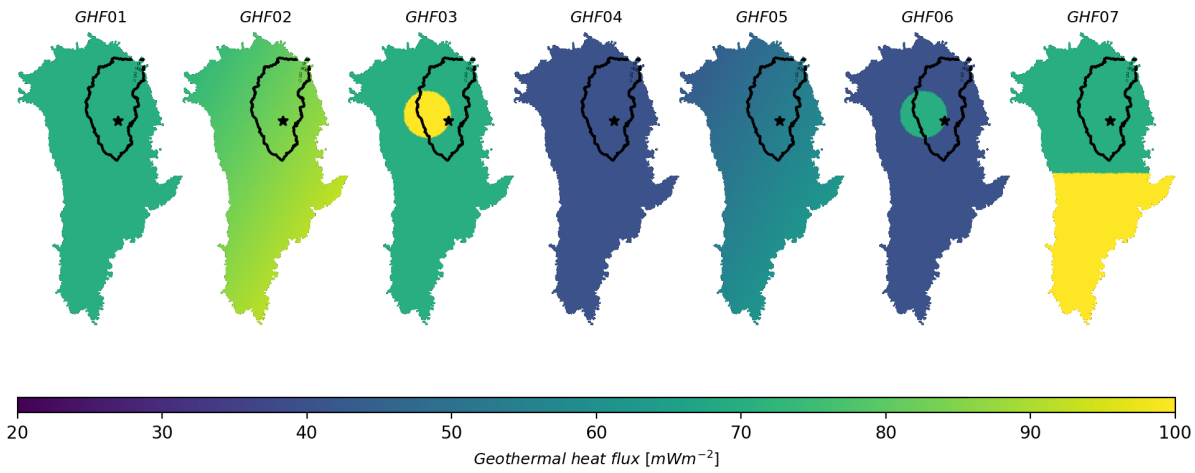

Figure 3.3: Heat flux maps of the synthetic GHF scenarios. Red star indicates location of EGRIP.

The isotope model is based on the isotope record from the NGRIP ice core (Andersen et al., 2004). This ice core is located on the ice divide in northern Greenland. The deep ice of the Greenland ice sheet is expected to have been deposited at or near the ice divide, even in the outer regions near the margin (see section 2.3.2). Since the analysis will focus on the area around the North-East Greenland ice stream, the isotope record of the near NGRIP ice core is ideal as the basis of the modelling of the basal isotope content.

However, the base at NGRIP dates back to only 123 ka BP (Andersen et al., 2004), which is exceeded by the age estimate for the basal ice in the simulations. Large areas of the simulated basal ice are more than 20 kyrs (thousands of years) older (see section 4.3). It is therefore necessary to utilise a longer record to extrapolate the isotope composition of the deepest ice.

This is achieved by correlating the isotope record of NGRIP to the record of atmospheric CO_2 from the Antarctic Vostok ice core (Petit et al., 1999). CO_2 is a global atmospheric tracer as it has a long atmospheric lifetime on the order of 100 yrs compared to the 1 year atmospheric exchange time between the northern and the southern hemisphere. It can thus be used to synchronise ice core records from Greenland and Antarctica (Blunier et al., 2007).

The CO_2 record at Vostok spans the timeframe of the past 420 kyrs covering four glacial-interglacial cycles (Petit et al., 1999). This extends sufficiently beyond the oldest ages of the simulated Greenland ice. The temporal resolution of the Vostok record, however, is variable and on the order of 0.5 - 2 kyrs. The NGRIP record has much higher temporal resolution which consequently cannot be modeled based on the Vostok record. The NGRIP isotope record is therefore treated with a 500-year running mean to decrease its resolution and prepare it for the correlation analysis.

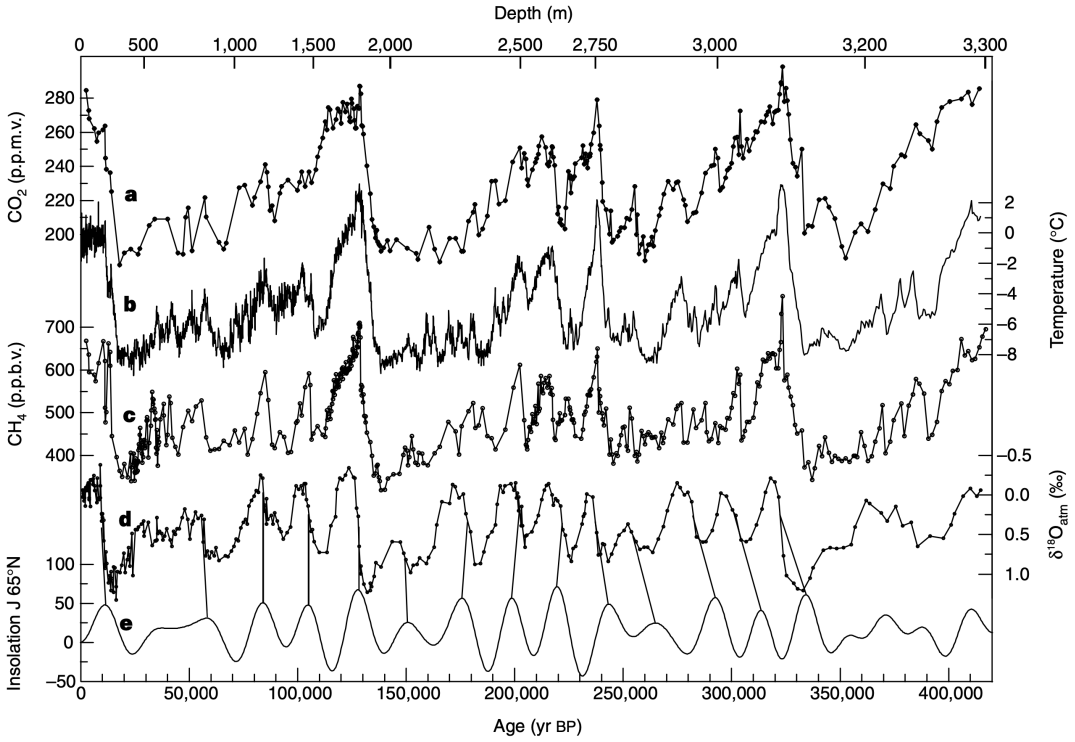

Figure 3.4: Records of different variables obtained from the Antarctic Vostok ice core. Graph a shows the CO2 record used for the extrapolation of the NGRIP isotope record. Figure from Petit et al. (1999).

Correlation of the thus treated NGRIP isotope record with the Vostok CO_2 record results in the relationship

$$iso[‰] = CO_2[ppm] * 0.08424944 - 58.729291 \tag{3.1}$$

with an R^2-value of 0.67, in which iso is the reconstructed NGRIP δ^{18}O record in $[‰]$ and CO_2 is the atmospheric CO_2 concentration in $[ppm]$ (parts per million) recorded in the Vostok ice core. As can be seen in figure 3.5, the reconstructed isotope record follows the original NGRIP record quite closely. Reconstructed Eemian values however fall noticeably short of the values in NGRIP and don't exceed Holocene values.

The modeled ages of the simulated basal ice are mostly not equal to the age of one of the Vostok data points but fall in between them. Extrapolating a CO_2 concentration to all modeled ice-ages is done by linearly interpolating between the CO_2 concentrations of the two age-adjacent Vostok data points. The respective influence of the two Vostok data points in the interpolation are scaled based on their age-distance to the modeled ice-age. The youngest age at Vostok is at 2.342 ka BP (with a CO_2 level of 184.7 ppm). For modeled ice-ages younger than that, a CO_2 concentration of 280 ppm is assumed.

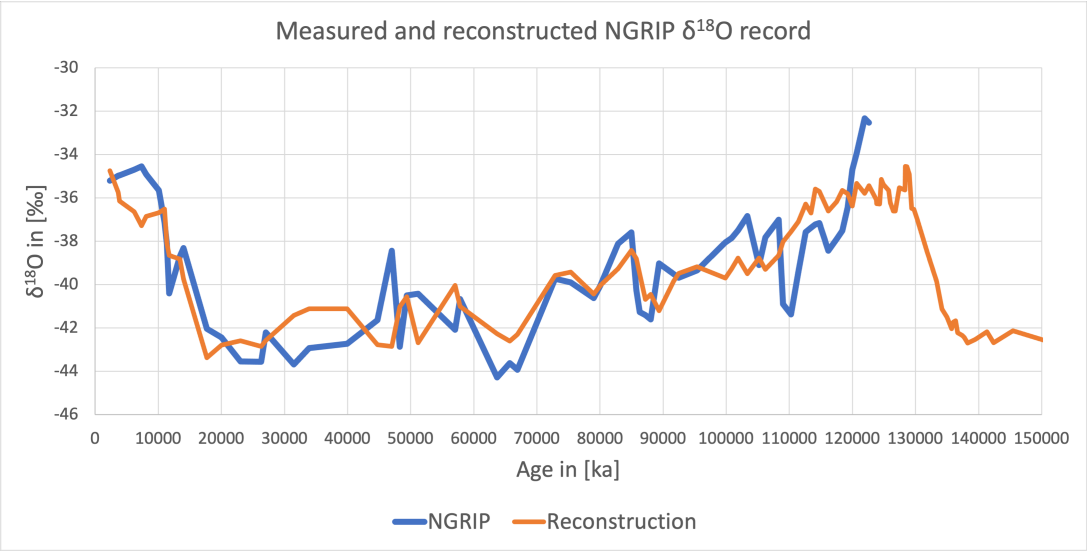

Figure 3.5: Isotope record of the NGRIP ice core. Blue line shows the original data from NGRIP treated with a 500-year running mean, orange line shows the reconstruction based on the Vostok CO2 record that extends beyond the NGRIP record.

Through the use of equation 3.1, it is possible to extrapolate the isotopic composition of the basal ice in Greenland with full areal coverage and beyond the extent of the record of the NGRIP ice core.

3.2.1 The Nye-plus-melt age model

The Nye+melt age model was formulated by Fahnestock et al. (2001). It is an extension of the age model developed by Nye (Nye, 1963) and circumvents the issue of infinite age at the base, that is inherent to other age models (see section 2.3.1), by accounting for basal melt and thus allowing for vertical movement of the ice at the base.

As laid out in section 2.3.1, the age t of an ice-layer in an ice sheet located at distance z above the base is related to the history of its vertical velocity w (notation follows Fischer et al., 2021), such that

$$t = \int_H^z \frac{1}{w}\, dz \tag{3.2}$$

(Fischer et al., 2021), in which H is the thickness of the ice sheet. The original Nye model (Nye, 1963) assumes constant vertical strain rate ε which means that vertical velocity is solely a function of depth. Assuming the ice sheet to be in steady state, the vertical strain rate can be set equal to the (constant) accumulation rate A divided by the ice thickness H. Hence, the vertical velocity can be expressed as

$$w(z) = -\varepsilon z = -\frac{A}{H} z \tag{3.3}$$

(Fischer et al., 2021; Fahnestock et al., 2001).

Inserting the Nye-model of vertical velocity into equation 3.2 gives the age of the ice as

$$t(z) = -\int_H^z \frac{H}{Az}\, dz = -\frac{H}{A}\, ln\left(\frac{z}{H}\right)$$

(Fischer et al., 2021).

In case of basal melting, the vertical velocity at the base ($z = 0$) is given by the basal melting rate M

$$w(z = 0) = -M$$

The original Nye-model doesn't account for basal melting. However, equation 3.3 is easily modified to incorporate basal melt

$$w(z) = -\frac{A - M}{H} z - M$$

(Fahnestock et al., 2001; Fischer et al., 2021).

Inserting this new 'Nye+melt' model of the vertical velocity into equation 3.2 then gives the age as

$$t(z) = -\int_H^z \frac{-1}{\frac{A-M}{H} z + M}\, dz = -\int_H^z \frac{-H}{MH + z(A - M)}\, dz$$

Integration finally provides the solution of the Nye+melt age model of ice layers in an ice sheet

$$t(z) = \frac{H}{A - M}\, ln\left(\frac{(A - M)H + HM}{(A - M)z + HM}\right) \tag{3.4}$$

3.3 An algorithm for the computation of basal meltwater routing and isotope mixing

To model the subglacial routing of water through the basal hydrological system, I use an algorithm that recursively computes the upstream water routing at each mesh vertex. This method is similar to previous studies by, e.g., Willis et al. (2012) who used the D8 algorithm (O'Callaghan and Mark, 1984) to model subglacial drainage or Chu et al. (2016) who used the D∞ algorithm (Tarboton, 1997). The latest version of this type of algorithm is the MD∞ (Seibert and McGlynn, 2007), which I use in this thesis. The MD∞ algorithm simulates water routing on a discrete grid based on hydropotential. Unlike previous algorithms, the MD∞ is able to simulate both convergent as well as divergent flow in all directions independent of the cardinal directions of the grid. Seibert and McGlynn (2007) define the mathemat-

ical framework of the algorithm for a regular quadratic grid which requires adaptation to the irregular triangular mesh used in the ISSM ice-sheet model. Mixing of isotope values in the basal water system is superimposed on this routing algorithm as a conservative tracer.

3.3.1 Previously existing algorithms

The MD∞ hydrological routing algorithm of Seibert and McGlynn (2007) is the most recent extension to the D8 algorithm originally formulated by O'Callaghan and Mark (1984). The D8 algorithm was developed to calculate surface water flow based on surface topography. The topography is provided as a digital elevation model which stores topographic data on a regular grid with square mesh cells, each cell containing one data point in its centre. The D8 algorithm compares the topographic height of each grid cell with the height of its eight neighbouring cells, identifies the steepest downward gradient, i.e., the neighbouring cell with the greatest downslope difference in topographic height, and routes all surface water that is present at the location to that cell.

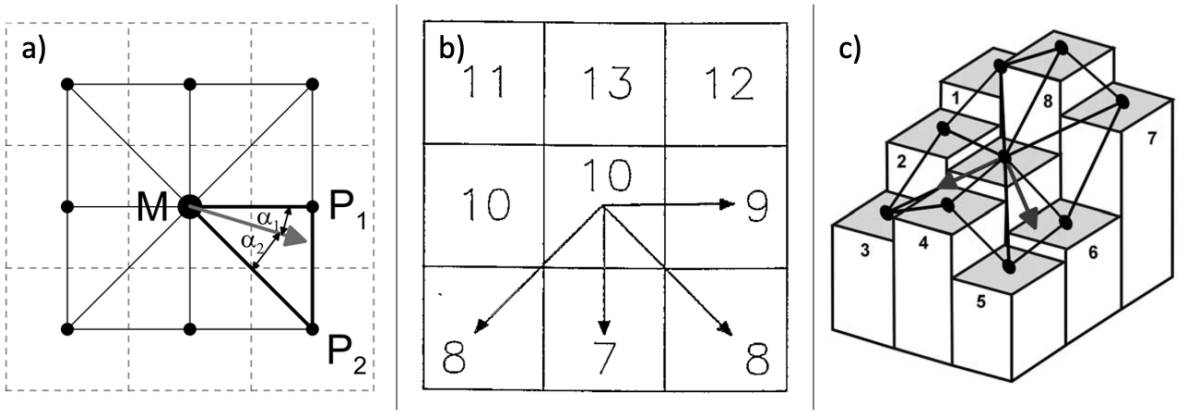

Figure 3.6: Geometrical concepts of the routing algorithms. a) D∞, dashed lines indicate the fundamental grid, points and solid lines indicate the constructed triangular mesh, arrow indicates direction of routing, water is routed from M to P1 and P2 proportional to angles a1 and a2; b) MD8, solid lines indicate the grid, numbers indicate topographic height, arrows indicate direction of routing, water is being routed from the centre cell to all cells of lower height; c) MD∞, three-dimensional depiction of the topography of the square grid and the constructed triangular mesh, arrows indicate direction of routing, routing is performed in multiple directions and in between data points. Figures a,c from Seibert and McGlynn (2007), figure b from Quinn et al. (1991).

However, since the routing in the D8 algorithm is performed by comparing one grid cell with its eight neighbouring cells and routing all water to only one of these cells, the routing is fundamentally limited to eight directions, hence the abbreviation D8. Water can be routed to one of the four cells that share a boundary with the centre cell (four cardinal

directions) or to one of the four cells that share one of the corners of the centre cell (four diagonal directions) (see figure 3.7a).

In reality, the flow of water is of course not limited to only four cardinal and four diagonal directions but can be directed in any direction between them. Additionally, depending on the shape of the local topography, water flow can split into multiple streams.

The first of these issues has been addressed in the D∞ algorithm by Tarboton (1997). In this algorithm water can be routed in any direction between the cardinal and diagonal grid directions. This is achieved by constructing eight triangular mesh elements around the centre grid cell (see figure 3.6a). Each of these triangles has one corner on the centre point of the centre grid cell, one corner on the centre point of one of the grid cells adjacent in cardinal direction, and the last corner on the centre point of one of the two adjacent cells in diagonal direction. Thus, instead of containing one topographic data point in their centre, these triangles connect three neighbouring data points and are thus tilted in the direction of the surface slope which is independent of the cardinal and diagonal directions. To perform the routing, the angular distance between the surface slope (which is the theoretically correct direction of routing) and the two nearest actual grid points is used to partition the water flow from the centre cell between these cells. This partitioning effectively enables the algorithm to route area into directions that lie in between the discrete grid points. Using this method, the amount of possible routing directions is thus infinite, hence the name D∞ (see figure 3.7c).

However, the D∞ algorithm is still restricted to routing the water at a grid cell in only one single direction. This issue has been addressed separately in the MD8 algorithm by Quinn et al. (1991) who extended the D8 algorithm to be able to split the routing into multiple directions at any grid point. In this algorithm, water flow is distributed to all of the eight neighbouring grid cells that lie downslope of the centre grid cell (see figure 3.6b). The distribution of area to the receiving grid cells is partitioned proportional to the steepness of the slope between the centre grid cell and each receiving grid cell. This algorithm is thus able to split the water routing into multiple directions at each grid point, i.e., simulate divergent flow (see figure 3.7b). It is however still fundamentally restricted to the eight cardinal and diagonal directions of the square mesh, hence the name MD8.

Finally, Seibert and McGlynn (2007) have combined these two extensions of the D8 to form the MD∞ routing algorithm (see figure 3.6c). By utilizing the triangular mesh elements of the D∞ and considering multiple downflow directions at each grid point like the MD8, this algorithm is independent of the cardinal and diagonal directions of the grid and is able to partition water flow into multiple directions (see figure 3.7d).

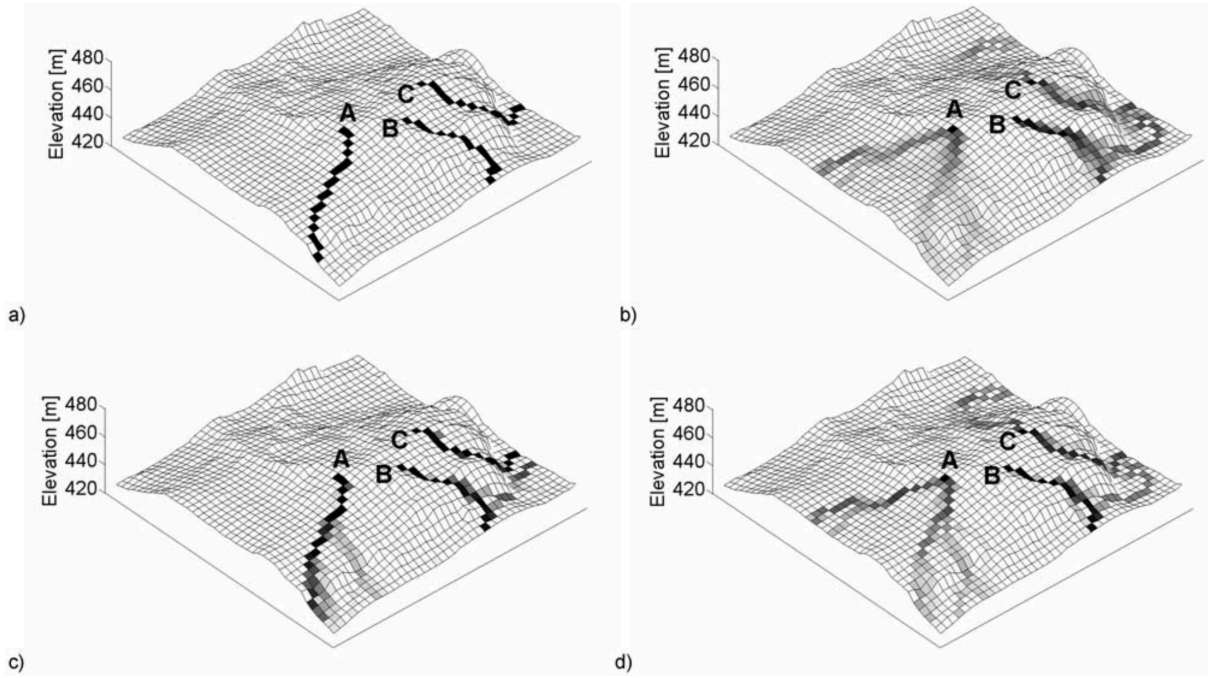

Figure 3.7: Comparison of the performance of the different routing algorithms. a) D8; b) MD8; c) D∞; d) MD∞. Figure from Seibert and McGlynn (2007).

3.3.2 Adaptation of MD∞ to ISSM mesh geometry

For this thesis, the routing algorithm will be combined with output data of the ISSM ice sheet model to simulate subglacial water routing and isotope transport. To do this, the MD∞ algorithm, which is designed to route surface water, needs to be adapted in two ways.

Firstly, the water routing does not follow the slope of the bed topography but the gradient of the subglacial hydropotential. This adaptation is straightforward as it simply requires replacing topographic height with the hydropotential in the calculation of the slope. The hydropotential is the Shreve-hydropotential as described in section 2.4 and is calculated according to equation 2.8. Similar to the method of Chu et al. (2016), the hydropotentail is calculated for six different floatation fractions going from $f = 0.6$ in 0.1 step increments to $f = 1.1$, which reflects floatation scenarios ranging from underpressured to slightly overpressured. Spurious small sinks in the hydropotential are filled in as the routing algorithm is not capable of simulating stagnant water flow (i.e., subglacial lakes). The six resulting hydropotential fields are displayed in figure 3.8.

Secondly, the basal meltwater data produced by the ice sheet model are not distributed on a uniform grid of square cells but an irregular triangular mesh. The data could of course

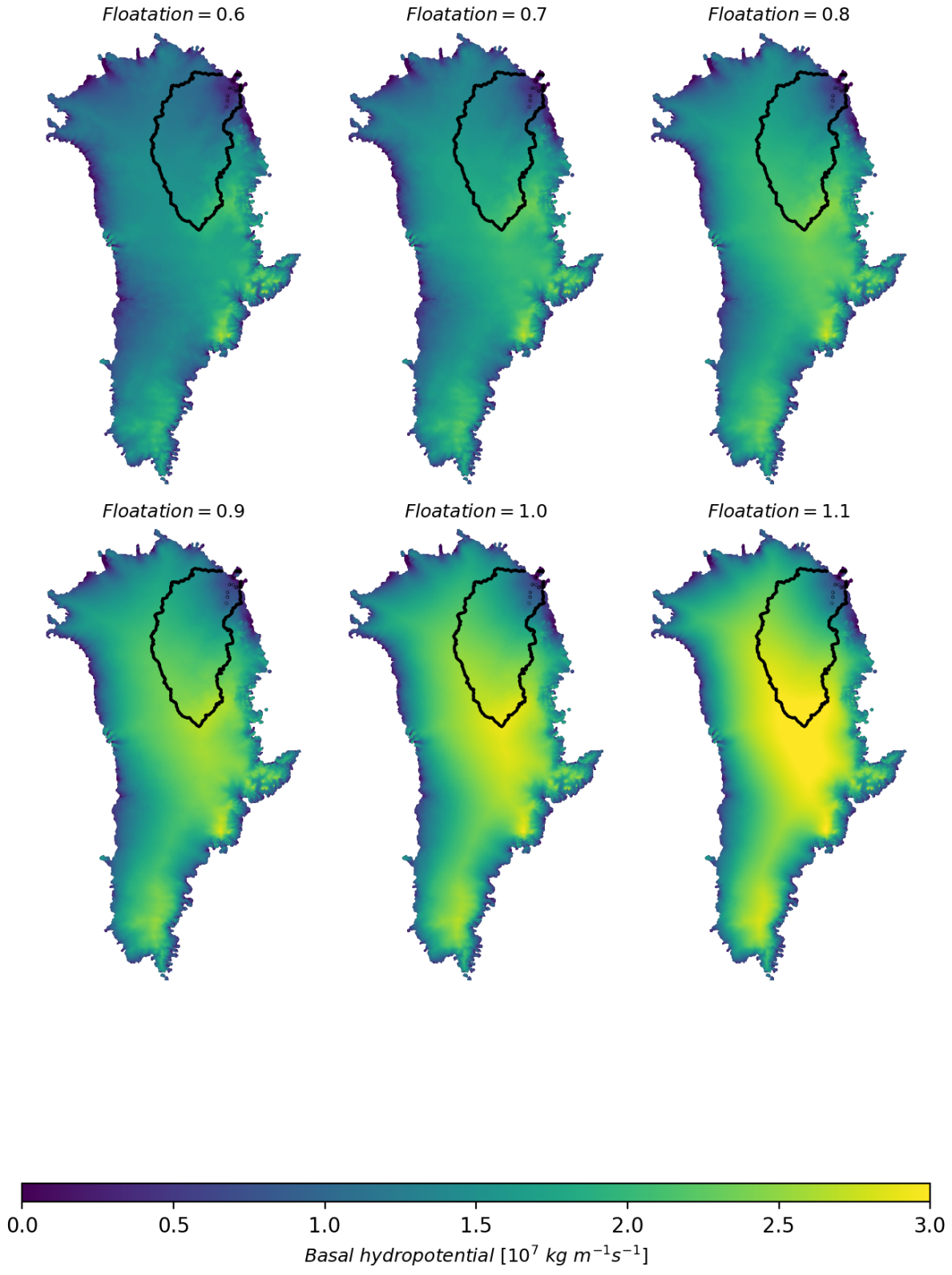

Figure 3.8: Greenland basal hydropotential for six different floatation fractions. Black outline indicates NEGIS drainage area (see figure 3.12).

be interpolated onto a square grid, however seeing as the concept of the D∞ routing scheme of Tarboton (1997) is to construct a triangular mesh on top of the original square grid the algorithm is easily adapted to an a-priori triangular mesh. However, seeing as the mesh used in the ISSM model is an irregular mesh, the number of triangular elements surrounding each data point is variable and usually less than eight. The number of surrounding elements needs to be checked for every data point as it affects the partitioning of flow for multi-directional routing.

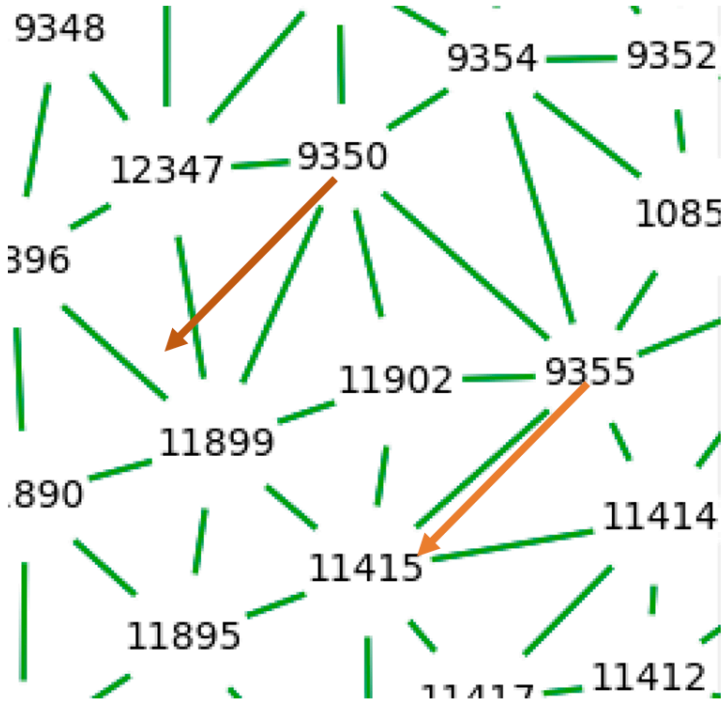

Figure 3.9: Example of the routing bug caused by the irregular mesh geometry. Green lines indicate the mesh, numbers are the numbers of the mesh vertices. Arrows indicate the direction of the gradient in hydropotential. The issue arises at vertex 11902, which is technically downslope of vertices 9350 and 9355 but doesn't receive any water from them. As the hydropotential gradient is not parallel to the connecting lines between the two upstream vertices (9350 and 9355) and their respective down stream vertices, the flow from each vertex is split between the two next vertex points according to the method of Tarboton (1997) shown in figure 3.6. Vertex 9350 thus routes water to vertices 12347 and 11899, and vertex 9355 routes to vertices 11415 and 11414. Neither of them route to vertex 11902 which breaks and restarts the routing at this vertex.

Unlike the square grid used in the original algorithms, the irregular mesh does actually create a fundamental bug in the routing that needs to be artificially fixed. Figure 3.9 shows a scenario in which a vertex doesn't receive water from neighbouring vertices even though it is lower in hydropotential. This is problematic as this effectively breaks and restarts the routing at this vertex meaning that all upstream information in terms of water volume and isotope content are lost. This situation is caused by local mesh geometry and cannot easily

be avoided inherent to the irregular nature of the mesh. Here, it is fixed in an intermediate post-processing step after calculating the routing directions for each vertex but before performing the actual routing. The output of the routing-direction calculation is scanned for such vertices that don't receive any water while at the same time being lower in hydropotential than some of their neighbouring vertices. They are then assigned a constant fraction of the outflux of all adjacent vertices that are higher in hydropotential. Volume of routed water is being conserved. It is a somewhat un-physical approach, but the benefit of unbroken water routing and persistence of routed information justifies that trade-off.

Using an irregular mesh for the routing comes with some conceptual differences to using a uniform grid. 1) The irregular mesh doesn't have any cardinal directions since all elements have different proportions and orientations, thus rendering mesh-induced bias in the overall routing direction impossible. 2) The mesh elements don't have uniform area. This needs to be corrected for in any analysis of flux or substance transport. 3) The number of surrounding triangular elements at any given data point in the mesh is variable. This implies that the resolution of routing direction and multi-directionality is also variable for different point in the mesh.

3.3.3 Including isotope mixing into the routing algorithm

The isotopic composition of water acts as a conservative tracer (Kendall et al., 2014). When two or more water masses are mixed, the δ^{18}O-value of the mixed water will be a composite of the respective δ^{18}O-values of each source water modulated by the fraction each source contributed to the new water mass.

Assume a water flow Q, defined as the flux of a volume of water per unit time, that is fed by several water influxes Q_i from n different sources such that

$$Q = \sum_{i=0}^{n} Q_i$$

Isotopic mass balance requires that the isotopic composition of the water of Q will be an intermediate of the isotopic compositions of all contributing water masses Q_i such that

$$Q\delta_w = \sum_{i=0}^{n} Q_i\delta_i \tag{3.5}$$

(Clark and Fritz, 1997) in which δ_w is the isotopic composition of the water in Q and δ_i is the isotopic composition of the water Q_i from each source.

This relationship has been successfully employed in the field of hydrology to delineate the contributions of different sources to a body of water (as reviewed by Klaus and McDonnell, 2013). If the isotopic compositions of a reservoir of water and all its water sources are known, equation 3.5 can be used to calculate the amount of water that each source has contributed to the reservoir. For example, Boral et al. (2019) were able to trace the variability in the contribution of glacial meltwater to Ganges river headwaters in the Himalayas using oxygen isotopes in the meltwater as tracers. Miller et al. (2021) found that meltwater from alpine glaciers is a critical source of recharge for mountain groundwater systems by separating the contribution of glacial meltwater in the mixed groundwater through its stable isotope signature.

Conversely, equation 3.5 can also be used to calculate the isotopic composition of mixed water given that all influxes and their isotopic compositions are known. In the routing algorithm, in can therefore be employed to calculate the isotopic composition of the basal meltwater and simulate the evolution of its δ^{18}O-values as it moves underneath the ice and mixes with meltwaters from different source regions.

At each mesh vertex, the basal meltwater is a mixture of 1) the meltwater produced at that vertex and 2) the meltwater routed to that vertex from its neighboring vertices. The isotopic composition of the meltwater that is produced at that vertex is that of the glacial ice at the base of the ice sheet at that vertex (see section 3.2; e.g., Boral et al., 2019; Miller et al., 2021). The influxes from the neighbouring vertices contribute their respective isotopic compositions to the initial meltwater. The composite isotopic composition of the mixed basal meltwater at any given vertex can thus be expressed by adapting equation 3.5 to the outlined scenario, which results in

$$Q_{out}\delta_w = Q_{melt}\delta_{ice} + \sum_{i=0}^{n} Q_i\delta_i \tag{3.6}$$

in which Q_{out} is the total outflux of water from the main vertex and δ_w is the composite isotopic value of the mixed basal meltwater at that vertex. For the meltwater produced at that vertex, Q_{melt} is the flux induced by the meltwater production and δ_{ice} is the isotopic composition of the melting basal ice. The water influxes from n neighbouring vertices are denoted by Q_i with δ_i as the isotopic composition of each influx.

Conceptually, this means that at any location the composite isotopic value of the basal meltwater is equal to the isotopic composition of the basal ice modulated by the basal melting rate and integrated over the basal upstream watershed area that drains water to that location.

The volume-flux Q_{melt} at each vertex can be calculated by multiplying the basal meltwater production rate given in meter per year $[ma^{-1}]$ with the area that is associated with the vertex. The volume of Q_{out} is calculated through the routing algorithm and is conceptually the basal meltwater production integrated over the basal upstream watershed area. The volume of Q_i is calculated in the same way, seeing as Q_i is Q_{out} at vertex i (or a fraction thereof in case of multi-directional routing at vertex i).

3.3.4 Testing the adapted algorithm

The functionality of the adapted algorithm is tested on a square domain with simple scenarios of hydropotential, basal meltwater production, and isotopic composition of the basal ice. The square test-mesh is generated in ISSM as an irregular triangular mesh similar in structure to that used in the Greenland model. The size of the domain is 1000 x 1000 m. An exemplary section of the mesh is shown in figure 3.10. Three hydropotential scenarios (shown in figure 3.11) have been constructed simulating parallel flow ('slope'), convergent flow ('valley'), and divergent flow ('peak'). The basal melting rate (shown in figure 3.10) is divided in two sections of different meltwater production to test if spatial variability in meltrate is correctly reflected in the volume routing. The basal isotope composition (figure 3.10) shows a one-directional gradient on an angle to the boundary between the melting zones to test the mixing of isotope values in the routed water.

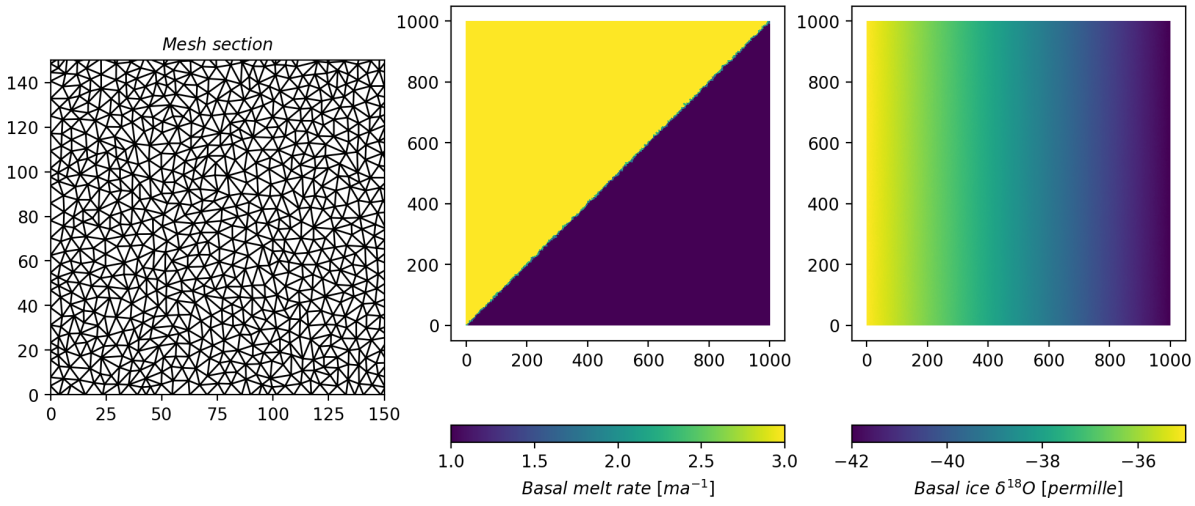

Figure 3.10: The setup of the routing test to test the routing algorithm. Left: Zoom-in section of the test mesh; Middle: Basal melt rate; Right: Isotopic composition of basal ice.

Figure 3.11 shows the results of the routing test. The routing is following the gradient in hydropotential correctly. In the 'slope' scenario designed to simulate parallel water flow, limited cross-gradient mixing of water still occurs, which is not unrealistic considering the

turbulent nature of real water flow. In all three scenarios it can be seen that water accumulates at the boundary of the domain and at low-spots in the hydropotential. These places effectively act as sinks as the routing is purely based on gradients in hydropotential and doesn't account for the volume of water present at any given vertex. In other words, the algorithm can only model water flow. It is not able to simulate the formation and overflow of lakes or otherwise stagnant water.

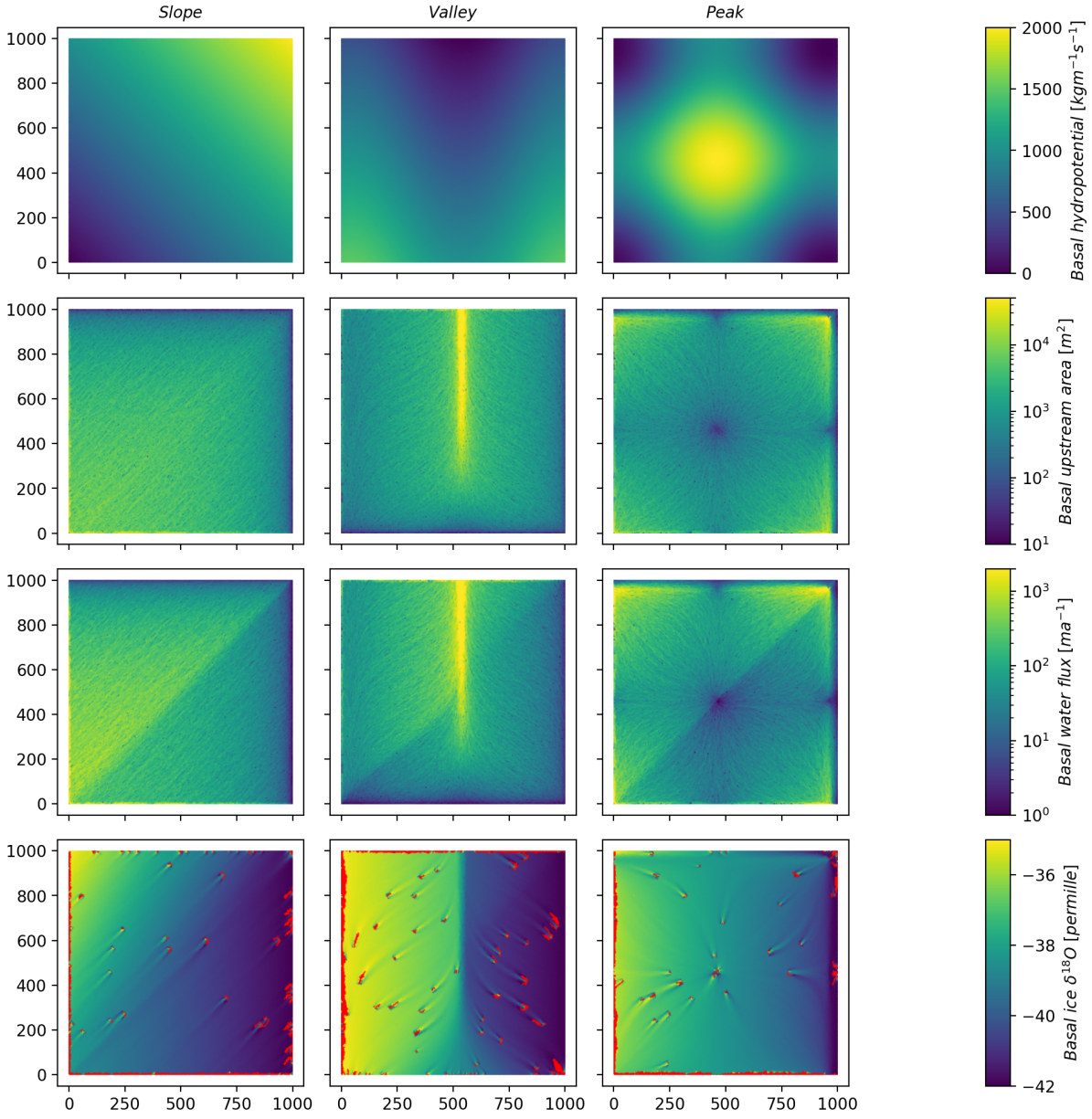

Figure 3.11: Results of the routing test, each column representing one scenario. Top row: Basal hydropotential that sets the test scenario; Second row: Cumulative basal upstream area; Third row: Basal water flux; Bottom row: Isotope composition of the routed and mixed basal water, red indicating bad values.

The routing and mixing of the isotope signal largely works in conjunction with the simu-

lated basal volume flux. However, as this part of the routing is based on mass-conservation it runs into issues along the boundary of the domain where it produces isotope values outside of the range of the input values, which is not possible. Likewise, the algorithm seems to run into mass conservation problems at spurious vertices throughout the domain. This problem could unfortunately not be solved in time. However, it doesn't seem to interfere with the mixing of isotope values on the large scale, so for the purposes of this thesis the algorithm can be considered to work.

3.4 Analysis of the basal meltwater isotopic composition

The analysis of the basal meltwater isotope data is focused on the area around the North-East Greenland Ice Stream (NEGIS). This area is of particular interest in terms of GHF. Some studies suggest high GHF to be the main driver of the fast ice flow of NEGIS (see section 2.1.3). In the adjacent area in central northern Greenland, some studies suggest a region of particularly high heat flux (see section 2.2). It is also the area where the potential remains of the Eemian ice are expected to be (see section 2.3.1). Seeing as over 15 % of the Greenland ice sheet area are draining through the NEGIS system Rignot and Mouginot (2012), untangling its underlying GHF conditions would be of great value.

The domain of the analysis is the area of the subglacial hydrological drainage system underneath the NEGIS region that drains basal meltwater towards the two northern outlet glaciers of NEGIS. This will be referred to as "NEGIS drainage basin" in this text. The NEGIS drainage basin is computed using the routing algorithm described in Section 3.3 and represents the area from where subglacial water drains towards Zachariæ Isstrøm and Nioghalvfjerdsfjorden. Since the hydropotential is the main driver of the water routing, the exact shape and size of the NEGIS drainage basin depends on the floatation fraction that is assumed for the calculation of the Shreve-hydropotential. Hence, this method results in six different estimates of the NEGIS drainage basin each corresponding to one of the six floatation fractions used to calculate the routing (see section 3.3.2, figure 3.12). The domain of the analysis is that part of the NEGIS drainage basin area that is common between all six floatation scenarios.

The shape of the NEGIS drainage basin would furthermore differ between the different GHF scenarios as the extent of the drainage depends on the extent of the basal melt area. However, since the routing is based on the Shreve-approximation of the hydropotential, it is set by the geometry of the ice sheet itself and thus independent of the actual amaount or even availability of basal water. The domain of the analysis can be hence be calculated from a 'master routing' that assumes uniform basal melting everywhere and is thus equal to the

maximum potential drainage area from where water would drain towards the NEGIS outlets.

For the individual GHF-(i.e., melting-)scenarios, areas with no basal melting are treated as frozen in the routing algorithm and the routing is directed around them to avoid development of large-scale sinks. However, it is still governed by the overall shape of the hydropotential and will thus not randomly flow back into the drainage system, meaning that even though the area of the NEGIS drainage basin might be different for the different GHF scenarios, the structure of drainage system will still develop in a similar way. This allows for the selection of defined analysis locations based on the properties and structure of the master drainage.

Inside the analysis domain, two sets of point locations have been chosen for the analysis (see figure 3.12). The seven black circles (C) are deliberately placed to follow the three main drainage pathways that form inside the NEGIS drainage basin, C1 and C2 follow the northern drainage path that is most prominent in the lowest floatation scenario, C3 and C4 follow the middle drainage path, and C5 and C6 follow the southern drainage path that formes right underneath NEGIS and is more prominent for the higher floatation scenarios. The exact paths of the drainage pathways differ slightly for the different floatations, but the Cs are placed to be inside the area of maximum water convergence for all scenarios. C7 is placed to cover the far southern tip of the domain and is part of the northern drainage path for the lower floatations up to $f = 0.8$ and part of the southern drainage path for the higher floatations from and above $f = 0.9$.

The ten blue triangles (T) are selected randomly within the analysis domain. Since it would be impossible to know if a drilling campaign will hit right in the centre of one of the drainage pathways with their borehole, it is important to get an estimate of how the isotope signal behaves outside of and in between the main water convergence areas.

The EGRIP location is also included in the analysis, since there will be the possibility for actual sampling of basal meltwater once the drilling is completed.

The positions of the Cs and also of EGRIP are given in x and y coordinates which don't necessarily align with the ISSM mesh points on which the data are stored. Therefore, at each C the data is taken from the nearest mesh vertex. The Ts are randomly selected vertices within the framework of the ISSM mesh, so they align with a data point by default.

At each analysis point, the mean isotope value is computed from the six isotope values derived from the six different floatation-scenarios. The maximum and minimum isotope values are extracted to give an estimate of the error range that is induced by the uncertainty

of the floatation.

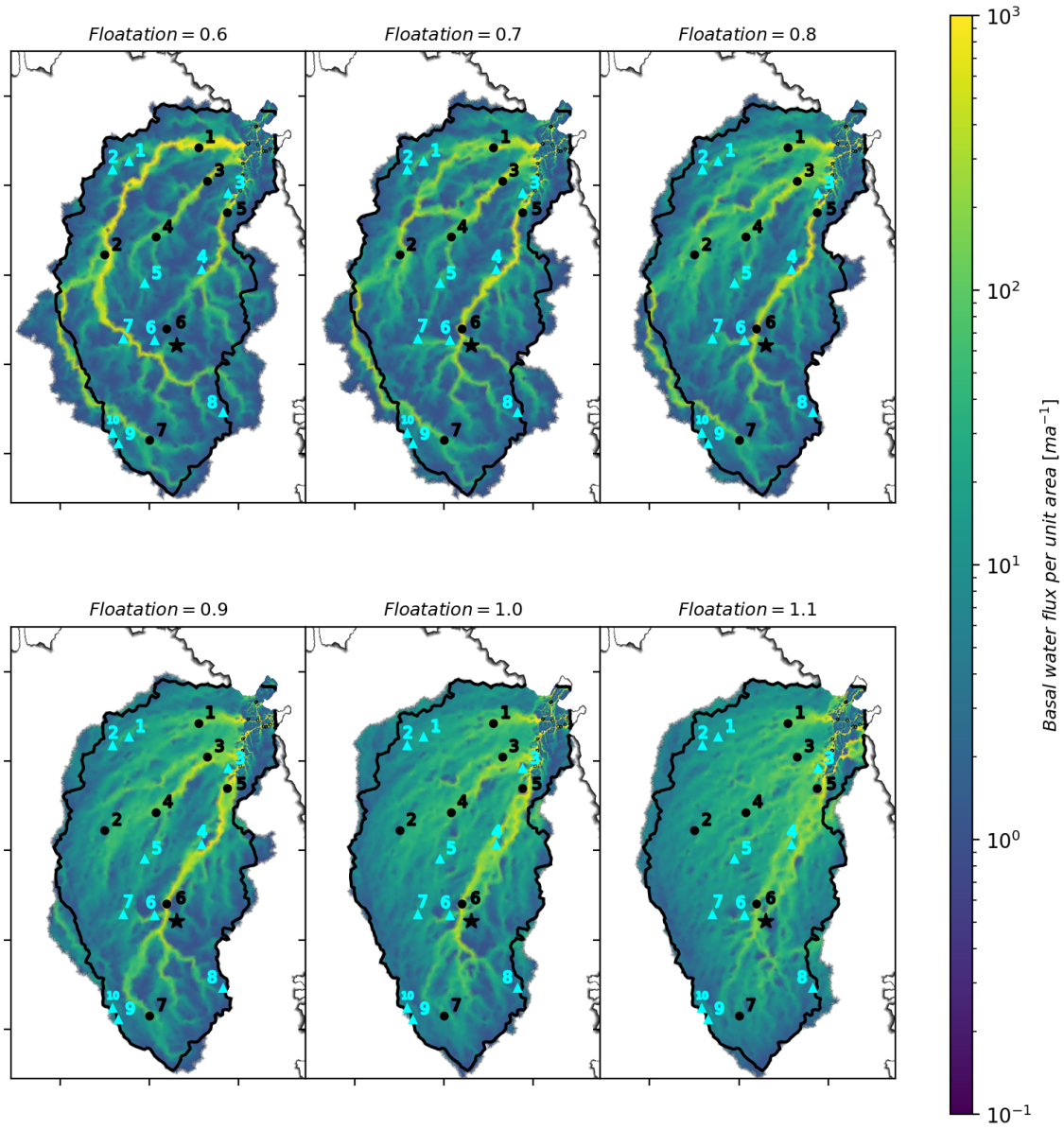

Figure 3.12: The subglacial drainage system in the NEGIS area for the six different floatation scenarios. Values on colorbar indicate area-normalized water flux. Black circles and blue triangles are analysis locations (see text). Black star indicates location of EGRIP. Black outline indicates the minimum common drainage area for spatial reference.

Chapter 4

Results

4.1 Results of ISSM simulations and basal melt estimates for different GHFs

Figures 4.1 and 4.2 show the estimates of basal meltrate produced by the ISSM simulations for each GHF scenario. Higher meltrates are generally found towards the perimeter of the ice sheet, whereas the inner parts of the ice sheet show lower meltrates, especially along the ice divides, with some GHF scenarios showing large areas of zero melt or even negative melt, i.e., basal freeze-on. High meltrates can be found underneath NEGIS in all GHF scenarios and generally along the western boundary of the ice, while the south-eastern part of Greenland generally shows very low and even negative meltrates. High variability in meltrate estimates between the GHF scenarios can be found in central North-Greenland and the area surrounding NEGIS.

Positive meltrates are generally of the order of 10^{-2} m/yr in the majority of the inner parts of Greenland, but increase to an order of 10^{-1} m/yr around the perimeter of the ice sheet, even reaching up to mulitple meters per year in some of the outlet glaciers.

For the GHF estimates (figures 4.1), Greve19 clearly shows the highest meltrates in northern Greenland, especially in the NEGIS drainage basin. Colgan22 shows the smallest overall meltarea.

Greve19, Martos18, and Lucazeau19 all produce meltrates that cover the entire area of the NEGIS drainage basin. FMaule09 shows large coverage of that area but around the perimiter of the drainage basin are some spots with frozen bed. Colgan22, Colgan22NG, and Shapiro04 all show large areas within the NEGIS drainage basin without basal melt. For Shapiro04, a large area of frozen bed is located along the south-western boundary of the dranage basin, for Colgan22NG a similarly sized area of frozen bed is located at the south-eastern boundary. Colgan22 shows shows essentially a combination of these two with large

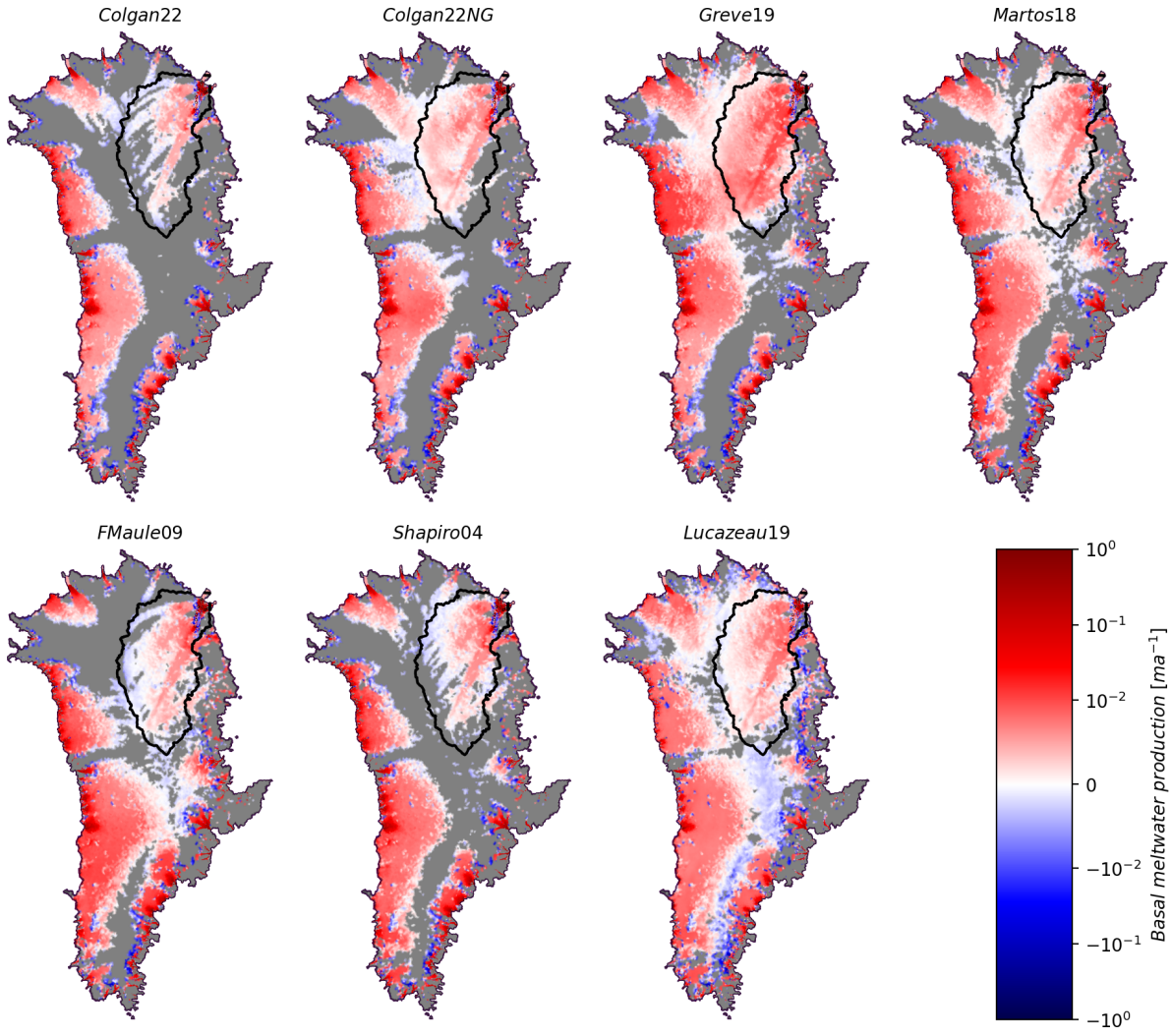

Figure 4.1: Simulated basal melt for the different GHF estimates. Red areas indicate basal melt, blue areas indicate basal freeze-on, grey indicates areas of zero basal melt. Black outline indicates the minimum NEGIS drainage area as spatial reference (see figure 3.12).

melt-free areas along both of these boundaries.

For Colgan22NG, Greve19, Martos18 and Lucazeau19, the basal ice is also melting in the central northern part of Greenland immediately west of the NEGIS drainage basin where the Eemian ice is assumed to be located.

For Colgan22, FMaule09, and Shapiro04, melt area does not extend beyond the western boundary of the NEGIS drainage basin into the central northern area. All of the GHF estimates show only very limited melting to the East and South of the NEGIS drainage basin.

For the synthetic GHFs (figure 4.2), GHF02 shows the highest melt rates and the largest areal coverage. Almost the entirety of the ice sheet base is melting in that scenario. Only areas towards the South-east are melt-free. GHF01, 03, and 07 show comparably large melt areas but with larger melt-free areas along the entire eastern margin. GHF03 shows very

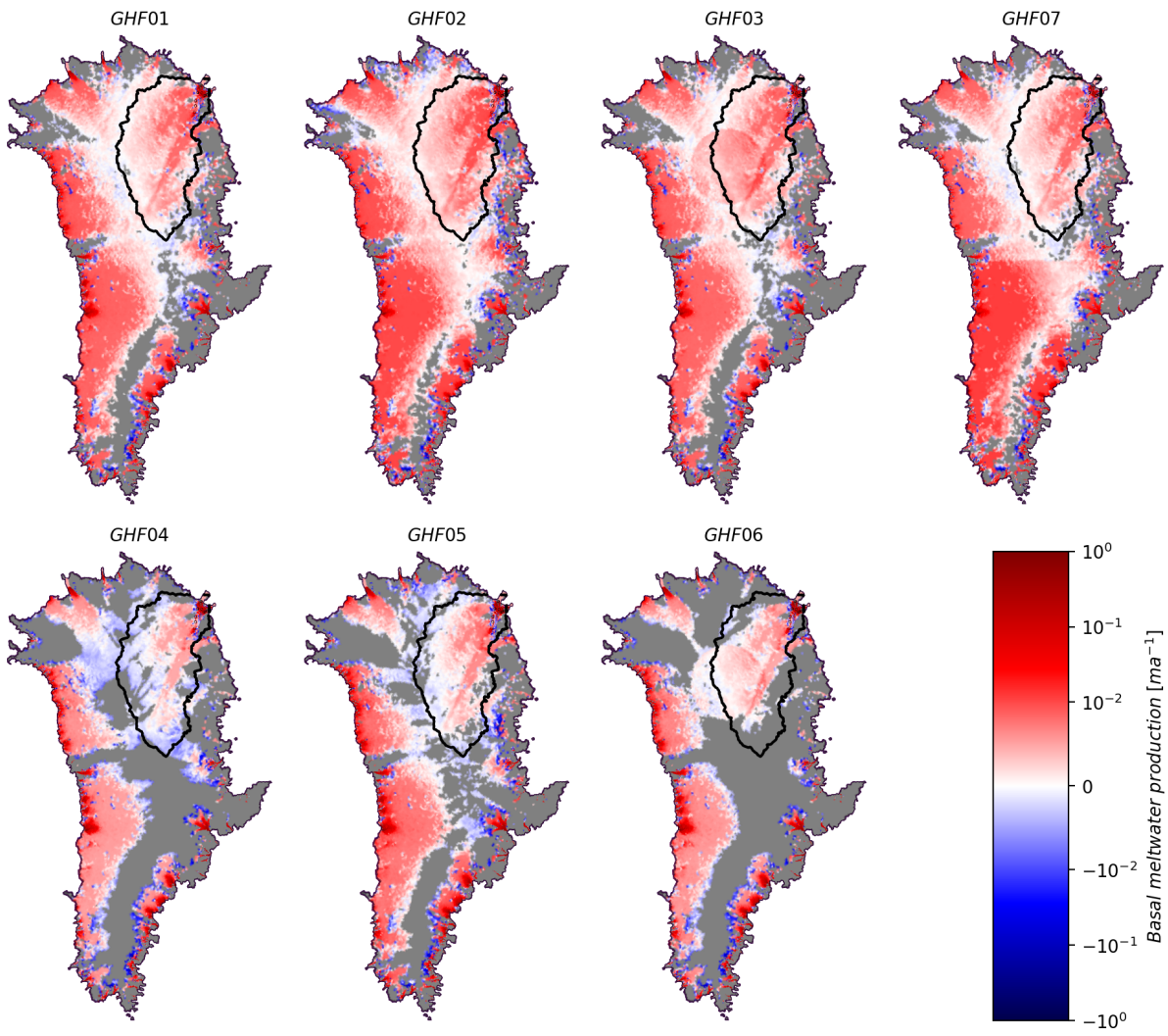

Figure 4.2: Simulated basal melt for the synthetic GHF scenarios. Colors as for figure 4.1.

high basal meltrates in the central northern part where the high GHF anomaly is placed. Elevation of meltrates in response to that anomaly is largely constrained to the exact area of the anomaly, its outline is clearly visible in the meltrate distribution. Similarly, the high GHF in the southern part of GHF07 does not seem to impact melt rates in the northern part, the boundary between the areas of higher and lower GHF is clearly visible.

GHF04-06 show substantially smaller meltareas, in particular towards the South-east and along the ice divides. Only GHF05 shows somewhat full areal coverage of basal melt in the NEGIS area, GHF04 and 06 show large areas within the NEGIS basin with no melting, GHF04 even has substantial areas of basal freeze-on covering large areas of the central northern part of Greenland.

4.2 Results of the subglacial water routing

Figure 4.3 shows the Greenland subglacial water drainage system for the six different floatation scenarios (see figure 3.8) calculated with the routing algorithm described in section 3.3. The drainages shown here have been calculated assuming uniform basal melt rate across the entire model domain. They thus represent the drainages with largest possible extent and maximum upstream area. In the routing allorithm, areas of no basal melt are treated as areas of basal freeze-on and are assumed to be impermeable for water flow. However, since the routing is based on the Shreve approximation of the hydropotential, differences in water input have no effect on the shape of the hydropotential and the structure of the drainage system will develop in the same way for all the different GHF scenarios (see also section 5.3 for a discussion of the implications of using the Shreve approximation). The drainage systems for each GHF scenario are therefore effectively the same as the ones shown in figure 4.3, just cropped to the area of basal melt (the routed water volume however will of course differ for each scenario, which is important for the mixing of the isotope signals in the basal water system). The drainage systems for each GHF scenario can thus be regarded as subsets of the maximum drainage systems.

Clear narrow drainage pathways develop at the base of the ice for the lower floatation fractions. However, they progressively ”smear out” for higher floatation fractions, which is particularly visible for floatations above 0.9. The drainage system for floatation fraction 1.1 ultimately doesn’t show any distinct drainage paths, rather the drainage is uniform across the entire area. This is consistent with the notion that lower floatation fractions lead to higher degrees of convergent water flow, whereas overpressured systems will lead to divergent water flow (Röthlisberger, 1972). For the higher floatations, the drainage paths are increasingly restricted to the ice drainage basins (see figure 4.3). Most ice divides become clearly visible in the structure of the basal drainage system above floatation 0.9. For the lower floatations, drainage pathways also flow across boundaries between ice drainage basins. A lot of drainage pathways originate in the central eastern part of Greenland and route water across the central ice divide to the West and to the North.

The figure shows area normalized water flux at the base. This naturally increases downstream of the drainages towards the ice margin as the drainage system is integrating more and more basal meltwater. In the lower floatations, the flux is more concentrated into the narrower drainage pathways where it is particularly large. In the higher floatations, flux is more distributed and hence shows lower maxima.

Furthermore, it can be seen that the location of the drainage pathways is largely stable across the different floatations. However, at some locations the main drainage will switch from one pathway to another above a threshold floataion fraction, similar to modelling re-

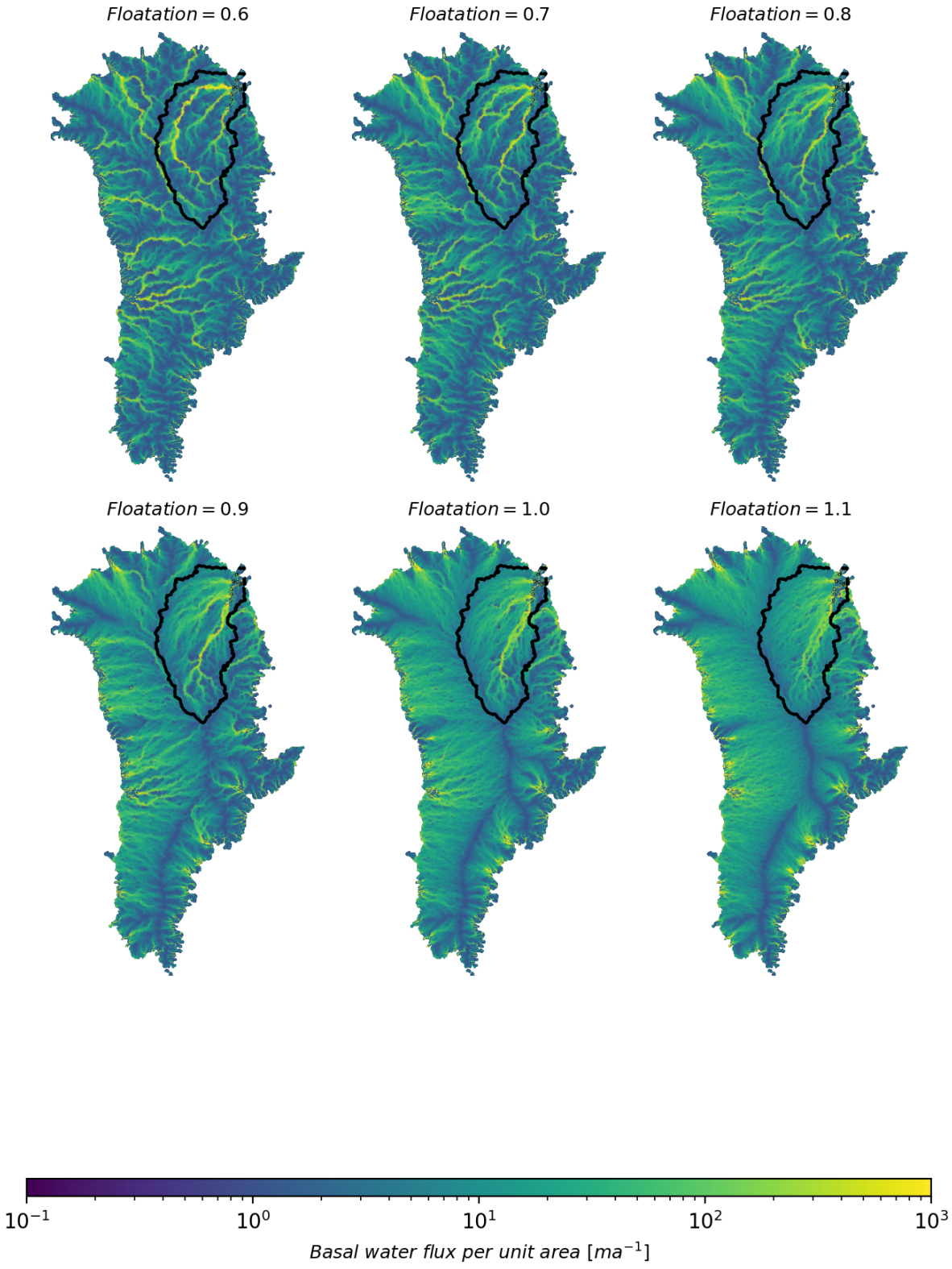

Figure 4.3: Greenland basal water flux for six different floatation fractions. Black outline indicates NEGIS drainage area (see figure 3.12).

sults described by Chu et al. (2016). In the NEGIS drainage basin, the main water drainage from the inception area of NEGIS in the south of the basin to its outlet glaciers switches between floatations 0.6 and 0.7 from a pathway following the northern boundary of the drainage basin to one directly underneath the ice stream. Another long drainage pathway going from central Greenland to Pettermann glacier in the North is diverted to the west above floatation 0.8.

4.3 Results of the age and isotope composition estimate of the basal ice

Table 4.1: Areas of glacial/interglacial periods in basal ice age. Area is given in square kilometers. Percentages indicate fraction of total area.

Estimated GHFs							
	Colgan22	Colgan22NG	Greve19	Martos18	FMaule09	Shapiro04	Lucazeau19
Total area	410 493	613 226	818 645	723 837	626 869	539 734	815 486
Holocene	78 704 (19.2 %)	80 272 (13.1 %)	86 394 (10.6 %)	94 347 (13.0 %)	97 169 (15.5 %)	98 080 (18.2 %)	97 344 (11.9 %)
Weichselian	325 434 (79.3 %)	519 801 (84.8 %)	726 243 (88.7 %)	608 111 (84.0 %)	521 047 (83.1 %)	434 263 (80.5 %)	695 728 (85.3 %)
Eemian	4 105 (1.0 %)	8 664 (1.4 %)	4 167 (0.5 %)	12 839 (1.8 %)	5 845 (0.9 %)	5 023 (0.9 %)	15 396 (1.9 %)
Saalian (capped at 140 ka)	2 249 (0.5 %)	4 490 (0.7 %)	1 841 (0.2 %)	8 541 (1.2 %)	2 808 (0.4 %)	2 368 (0.4 %)	7 018 (0.9 %)

Synthetic GHFs							
	GHF01	GHF02	GHF03	GHF04	GHF05	GHF06	GHF07
Total area	888 875	1 085 229	914 991	447 540	591 785	481 332	1 001 214
Holocene	95 590 (10.8 %)	111 633 (10.3 %)	93 090 (10.2 %)	76 366 (17.1 %)	91 648 (15.5 %)	77 635 (16.1 %)	111 719 (11.2 %)
Weichselian	771 075 (86.7 %)	967 368 (89.1 %)	814 711 (89.0 %)	363 799 (81.3 %)	490 570 (82.9 %)	385 439 (80.1 %)	867 716 (86.7 %)
Eemian	13 990 (1.6 %)	4 455 (0.4 %)	4 401 (0.5 %)	5 281 (1.2 %)	5 955 (1.0 %)	12 558 (2.6 %)	13 517 (1.4 %)
Saalian (capped at 140 ka)	8 221 (0.9 %)	1 773 (0.2 %)	2 789 (0.3 %)	2 094 (0.5 %)	3 612 (0.6 %)	5 700 (1.2 %)	8 262 (0.8 %)

Figures 4.4 and 4.5 show age and isotopic composition of the basal ice for the GHF estimates, figures 4.6 and 4.7 show the same for the synthetic GHFs. They also highlight the areal distribution and extent of the ice of the different glacial/interglacial periods (Holocene, Weichselian, Eemian, Saalian) at the base of the ice sheet. The corresponding data is listed in table 4.1. The boundaries between the glacial/interglacial periods are 11.7 ka for Holocene/Weichselian boundary, 116 ka for Weichselian/Eemian boundary, and 128.5 ka for Eemian/Saalian boundary (Bazin et al., 2013; Walker et al., 2008, 2009; Andersen et al., 2004; CAPE-Last Interglacial Project Members, 2006; Gibbard and Head, 2020).

The age estimates for the basal ice have been calculated from the simulated basal melt rates using the Nye+melt method as layed out in section 2.3.1. As the Nye+melt method

critically depends on the presence of basal melt to not result in infinite age, the age estimate can only cover areas where the simulations of the different GHF scenarios result in positive basal melt. The total area covered by the age estimate thus differs substantially between the GHF scenarios ranging from ca 400 000 km^2 to over 1 000 000 km^2.

The youngest basal ice is of holocene age and can be found around the perimeter of the ice sheet, mostly in the South and Southwest. From there, age increases towards the centre of the ice sheet. The oldest ice dates back to around 140 ka for all GHF scenarios, which means that it is ice from the Saalian glacial period. Ages above 140 ka appear only on spurious individual nodes amongst the oldest ice. The age estimate is therefore capped at 140 ka. Still, that time frame contains the full duration of the Eemian interglacial which appears in the basal age estimate of all GHF scenarios. However, the extent of the area that is covered by Eemian ice differs by a factor of three between the smallest and the largest extents, ranging from ca. 4 000 km^2 to ca. 15 000 km^2 (see table 4.1). The precise location of the oldest ice varies for the different GHF scenarios, but it can be found in the general region of central north-Greenland. Largest extents of Eemian ice are found in the Martos18 and Lucazeau19 scenarios. FMaule09 and Shapiro04 show smaller Eemian extent, Colgan22NG shows several distinct small areas of Eemian ice. Greve19 shows little amounts of Eemian ice but largely outside of the NEGIS drainage area. Minimal extent of Eemina ice is found in Colgan22. In the synthetic scenarios, only GHF01, 06, and 07 show large amounts of Eemian ice. This corresponds to the scenarios in which the central northern part of Greenland has medium heat flux values of 70 mW/m^2. For GHF02 and 03 heat flux values are higher, for GHF04 and 05 they are lower. In both cases, extent of Eemian ice at the base is reduced.

In all scenarios, ice from the last glacial period (Weichselian) covers by far the largest area with around 80 to 90 % of the total area, followed by ice from the Holocene which covers between 10 and 20 % of the total area. Eemian and Saalian ice each cover less than 2 % of the total area in all but one scenario.

The isotopic composition of the basal ice has been calculated based on its relationship to ice age as layed out in section 3.2. Isotope values range between minimally -43.4 ‰ and maximally -34.5 ‰ to -33.9 ‰, depending on the GHF scenario. Regions of Holocene ice show high isotope values above -36 ‰. Weichselian ice shows lower isotope values between around -40 ‰ to -44 ‰. Weichselian isotope values generally decrease during the progression of the glacial period (see figure 3.5). Therefore, the lowest values can be found towards the transition to the Holocene ice in the outer areas of the glacial ice that correspond to the younger parts of the glacial period. Higher values can be found in the inner areas of the glacial ice that correspond to the older parts of the glacial period. Within the glacial ice,

striations of undulating higher and lower isotope values can be observed parallel to the ice sheet boundary. These correspond to the major isotopic variations within the Weichselian period, as seen in the graph of the reconstructed NGRIP isotope values (figure 3.5). The Eemian ice in the central areas of northern Greenland shows higher isotope values up to -34 ‰. As the different GHF scenarios show different basal extents of the Eemian ice area, the isotope values in northern Greenland vary accordingly and are highest in the GHF scenarios with largest Eemian ice areas.

4.4 Results basal meltwater isotopic composition

Figures 4.8 and 4.9 show the isotopic composition of the basal meltwater calculated by combining the hydrological routing of the basal meltwater with the isotopic composition of the basal ice as described in section 3.3.3. The displayed isotope values are the mean isotope values of the basal meltwater calculated from the six floatation scenarios. The overall distribution of isotope values is similar to the isotope distribution in the basal ice, but appears ”smeared” in comparison. Since the isotope values are mixed together along the basal drainage system, the overall isotopic composition of the basal water is more homogeneous and doesn’t show as much spatial variability as the basal ice. Notably, the lowest isotope values in the youngest part of the Weichselian ice are ”over-written” as they are mixed with the much higher isotope values from the upstream Eemian ice. This can be observed in particular along the main drainage paths (see figure 3.12) where the bulk of the upstream inland meltwater flows to and consequently lifts the local isotopic signal. In between the major drainage pathways, the lower local isotopic signal of the younger Weichselian ice is more dominant.

Figure 4.10 shows the isotope values of the basal meltwater for the different GHF scenarios at selected locations (plots showing the graphs of all locations can be found in the appendix, A). The isotope values are again the mean isotope values of the respective six floatation renditions of each GHF scenario. The error estimate depicted as an error bar at each data point is the span between the maximum and minimum isotope value of the floatation scenarios at that location. Plots are shown for locations C1, C7, and a cluster of locations around the EGRIP area that show similar behaviour (EGRIP, C4, C6, T5, T6). Other locations did not show identifiable differences in the isotope values between different GHF scenarios and are therefore excluded from further analysis.

Looking at the synthetic GHF scenarios in figure 4.10 it can be seen that the isotopic values produced by GHF07 are virtually indistinguishable from the values produced by GHF01. This result was expected, as the two GHFs differ only in the southern half of

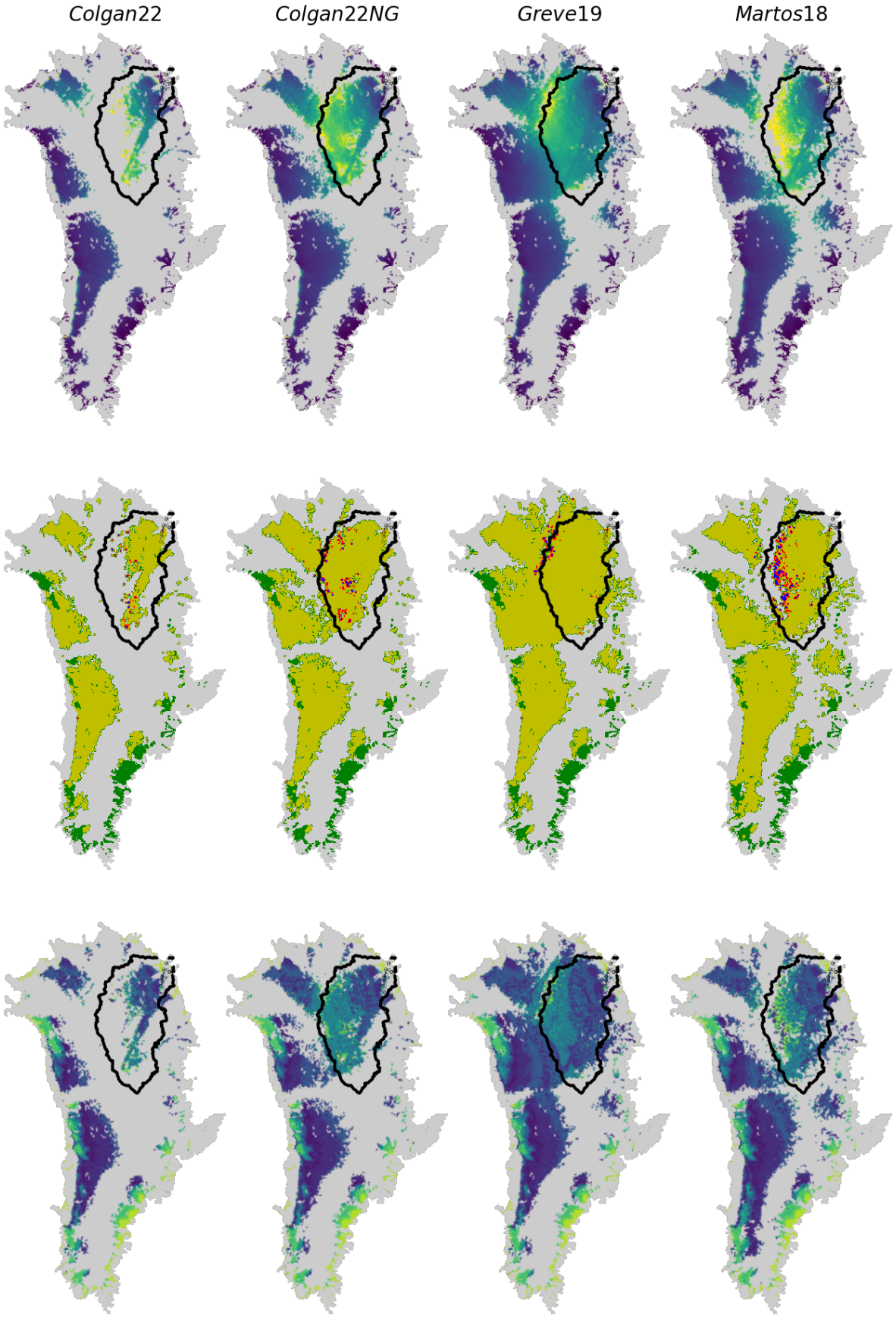

Figure 4.4: Age and isotopic composition of the basal ice for the GHF estimates. Each column refers to one GHF scenario. The first row shows the basal age estimate, the second row shows the areal distribution of inter-/glacial periods in the basal age, and the third row shows the estimate of the isotopic composition of the basal ice.

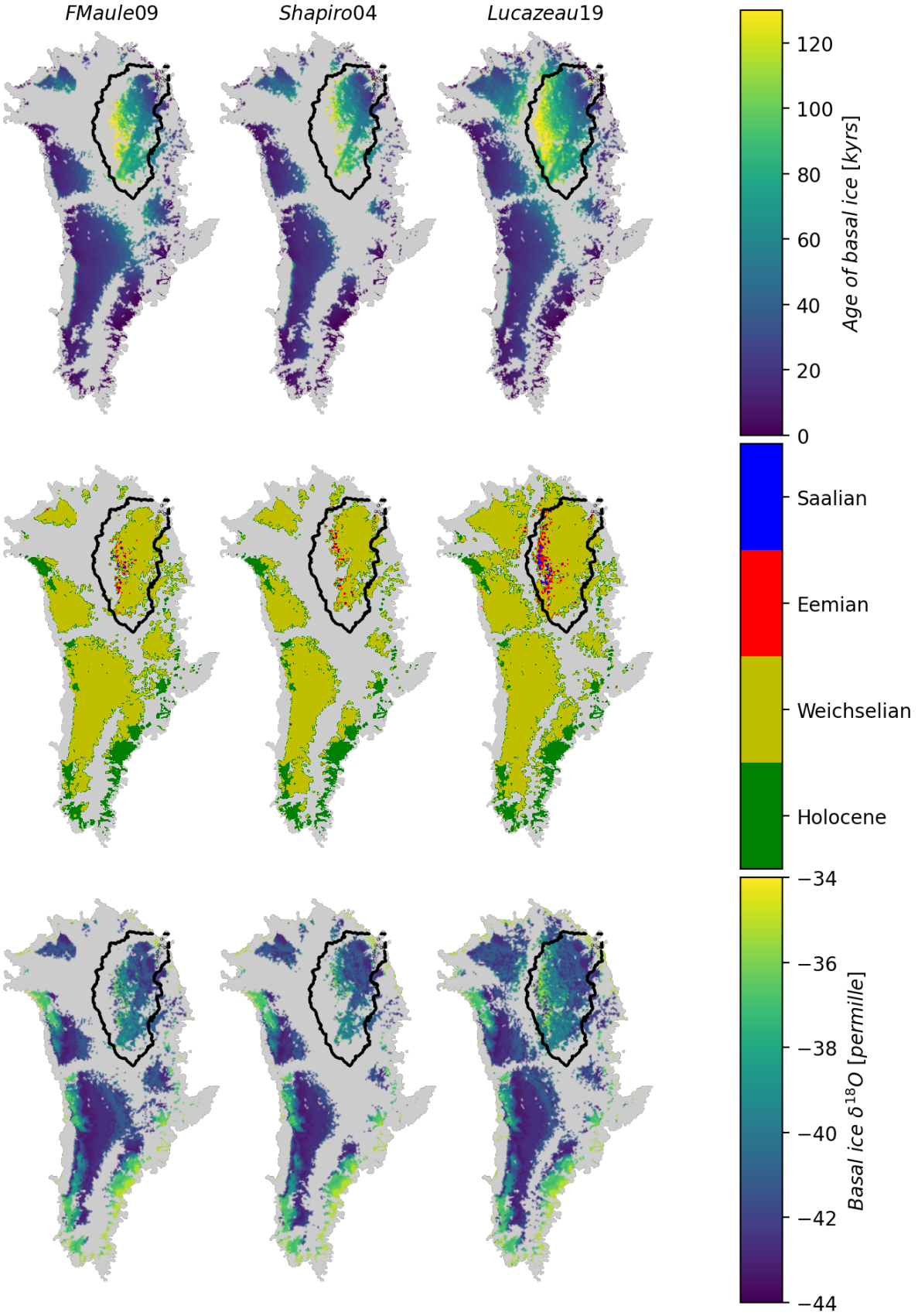

Figure 4.5: Continuation of figure 4.4. First row colorbar indicates basal ice age in kyrs, second row colorbar gives period labels, third row colorbar indicates delta18O values in ‰.

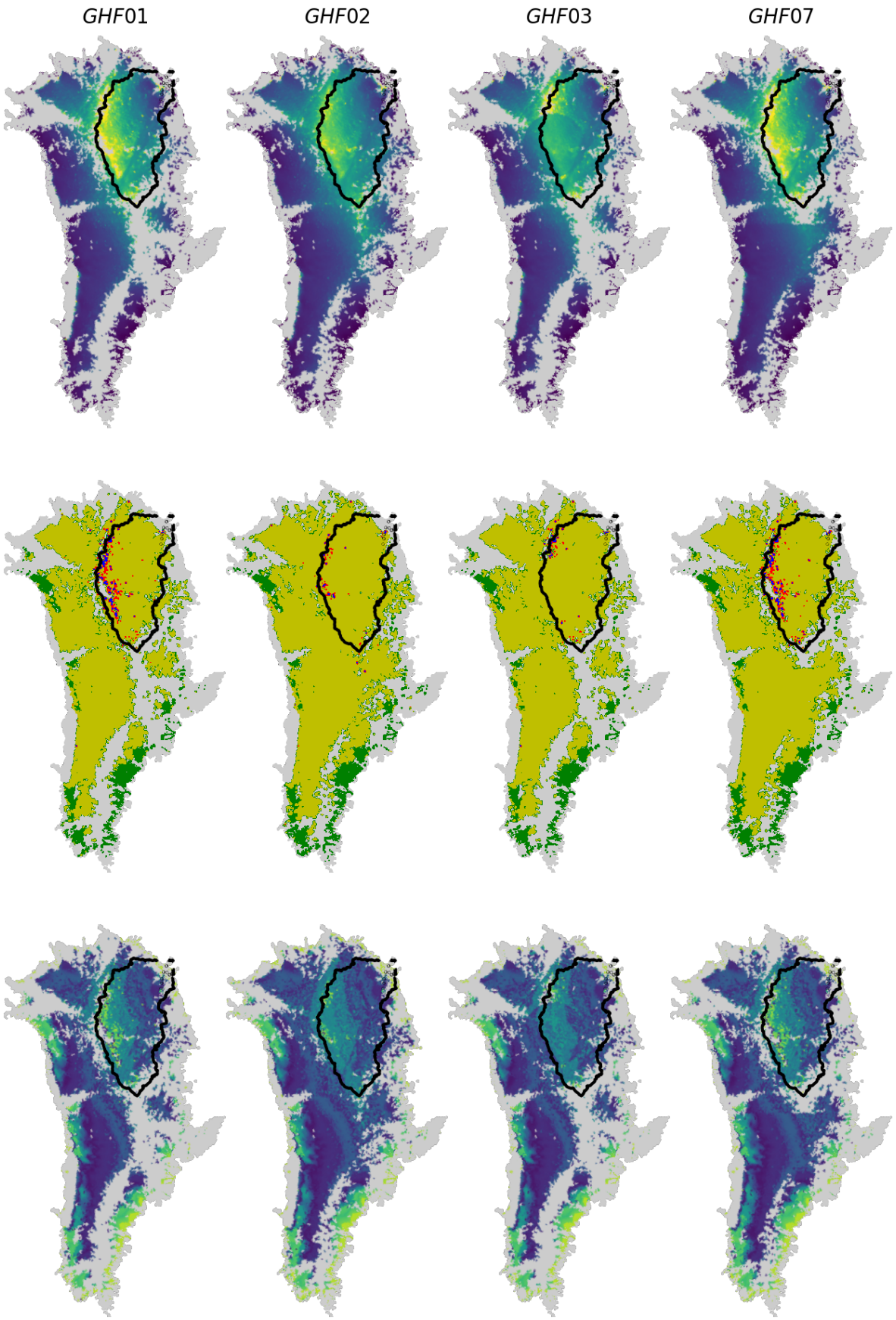

Figure 4.6: Age and isotopic composition of the basal ice for the synthetic GHFs. Layout and color scheme as for figures 4.4 and 4.5.

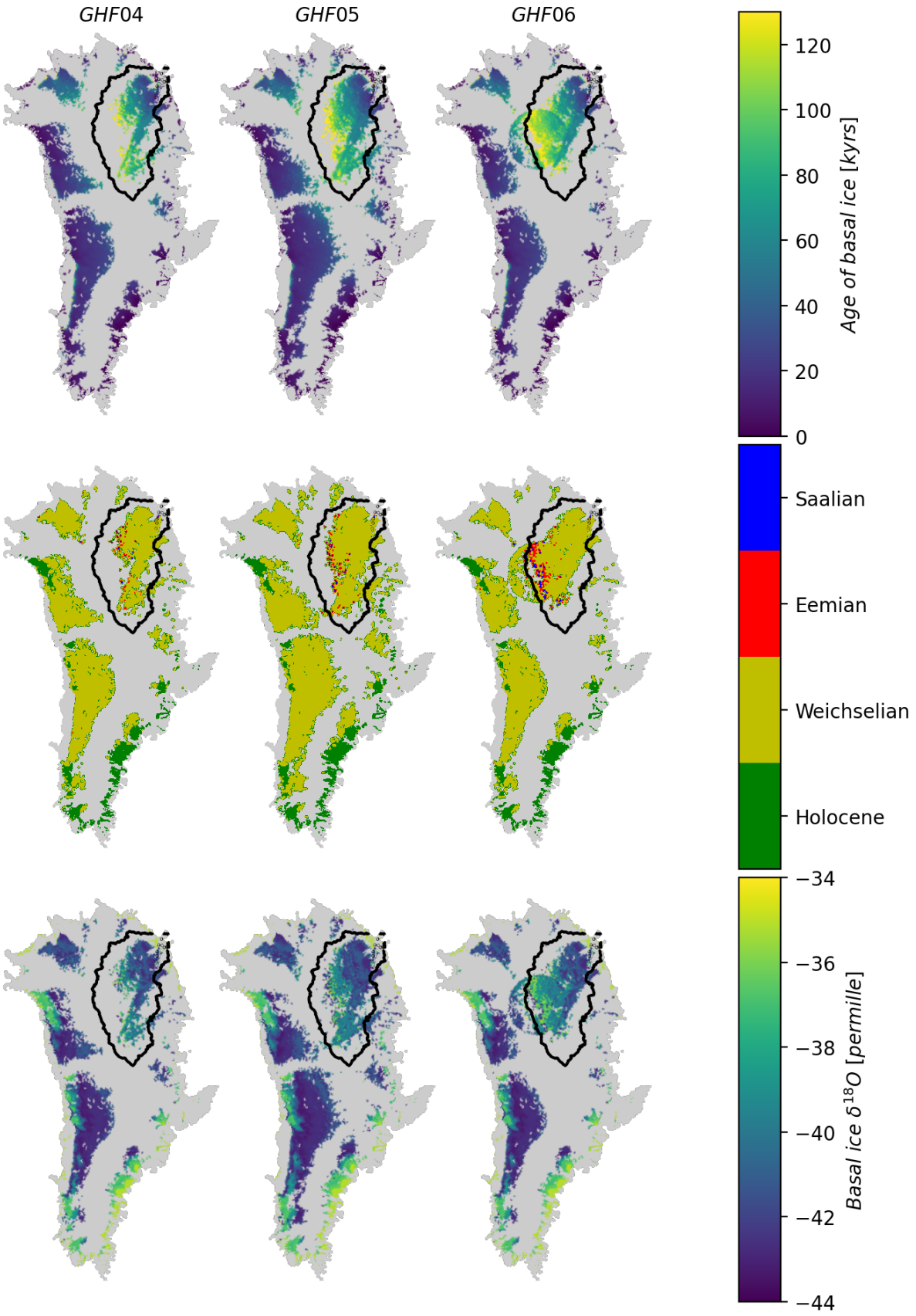

Figure 4.7: Continuation of figure 4.6.

Greenland but the analysis locations are all in the northern part of Greenland. The isotope values produced by GHF07 will therefore not be explicitly described and discussed.

At C1, isotope values from different GHF scenarios are clearly distinguishable from each other, both for the synthetic GHF scenarios as well as the GHF estimates. Isotope values seem to fall on two levels. Colgan22NG, Greve19, Martos18, and Lucazeau19 as well as GHF01, GHF02, and GHF03 show higher isotope values between -40.5 ‰to -40.7 ‰. Isotope values for Colgan22, FMaule09, and Shapiro04 as well as GHF04, GHF05, and GHF06 are lower and fall between -41.4 ‰and -41.6 ‰.

At C7, isotope values for the synthetic GHFs show only small variability with all GHF scenarios resulting in isotope values between -39.2 ‰and -39.9 ‰. For the GHF estimates, isotope values are mostly inside the same range, Colgan22 however shows a distinctly higher value around -38.4 ‰.

Around the EGRIP area, locations EGRIP, C4, C6, T5, T6, and T7 show distinctly similar patterns in their variability, both for the GHF estimates as well as for the synthetic GHFs. At EGRIP, GHF01-03 are indistinguishable from each other with mean values tightly constrained between -41.4 ‰and -41.5 ‰. Values for GHF04-06 range from -40.2 ‰to -41.1 ‰with GHF04 showing a clearly higher value than GHF05 and GHF06. At C6, isotope values fall on two levels. GHF01-03 showing values between -40.4 ‰and -40.9 ‰, GHF04-06 showing distinctly higher values between -39.5 ‰and -39.9 ‰. At C4, GHF04-06 are indistinguishable from each other with values between -39.6 ‰and -39.7 ‰. GHF01-03 show more variability with values between -39.9 ‰and -40.6 ‰, GHF03 showing the lowest values and GHF01 the highest. At T5, GHF01, GHF05, and GHF06 show indistinguishable isotope values of around -39.2 ‰to -39.3 ‰, only GHF02 and GHF03 show lower values with around -39.7 ‰and -40.5 ‰respectively. At T6, GHF02 and GHF03 show the lowest isotope values with around -39.8 ‰. GHF01 and GHF06 show distinguishably higher values of around -39.0 ‰. GHF05 shows a isotope value of around -37.8 ‰, but with a larger error bar. At T7, GHF01 and GHF06 have indistinguishable isotope values of around -38.0 ‰, GHF02 and GHF03 have lower values of around -39.3 ‰and -39.7 ‰respectively. The very low isotope value of GHF05 at this point is an outlier as the location lies directly on the boundary of the isotope area. GHF04 does not show isotope values at T5-7.

For the GHF estimates, Colgan22 shows the highest isotope value at EGRIP with around -40.2 ‰and Greve19 the lowest with around -41.4 ‰. The rest of the GHF estimates are indistinguishable and show values between -40.8 ‰and -41.0 ‰. Colgan22NG shows a very low value around -42 ‰with a large error bar. This is likely and outlier as EGRIP is located right on the edge of the isotope area in this GHF scenario. At C6, Greve19 shows

the lowest isotope value with around -41.2 ‰. The rest of the GHFs show evenly spread values between -39.5 ‰and -40.2 ‰with Colgan22 showing the highest value and Martos18 the lowest. C4 shows a similar situation, the lowest isotope value again for Greve19 with -40.5 ‰and evenly spread values for the other GHFs between -39.9 ‰and -39.3 ‰, the lowest value for Colgan22NG and the highest for FMaule09. At T5, Greve19 shows the lowest value with around -40.2 ‰, the other GHFs show values between -38.8 ‰and -39.5 ‰. At C6, Greve19 again shows the lowest value with around -40.1 ‰, the values of the other GHFs are more spread out than for T5. The isotope value Colgan22NG is around -39.3 ‰, for both Martos18 and Lucazeau19 values are around -38.6 ‰, and for FMaule09 the value is around -37.6 ‰, although with a large error bar. At T7, isotope values for the different GHFs are very spread out. Colgan22NG and Greve19 show values around -40.1 ‰, FMaule09 shows the lowest value around -41.0 ‰, Lucazeau19 and Martos18 show higher values with around -38.6 ‰and -37.0 ‰respectively, but both with large error bars. Colgan22 does not show values at all three of the Ts, Shapiro04 does not show values at both T6 and T7.

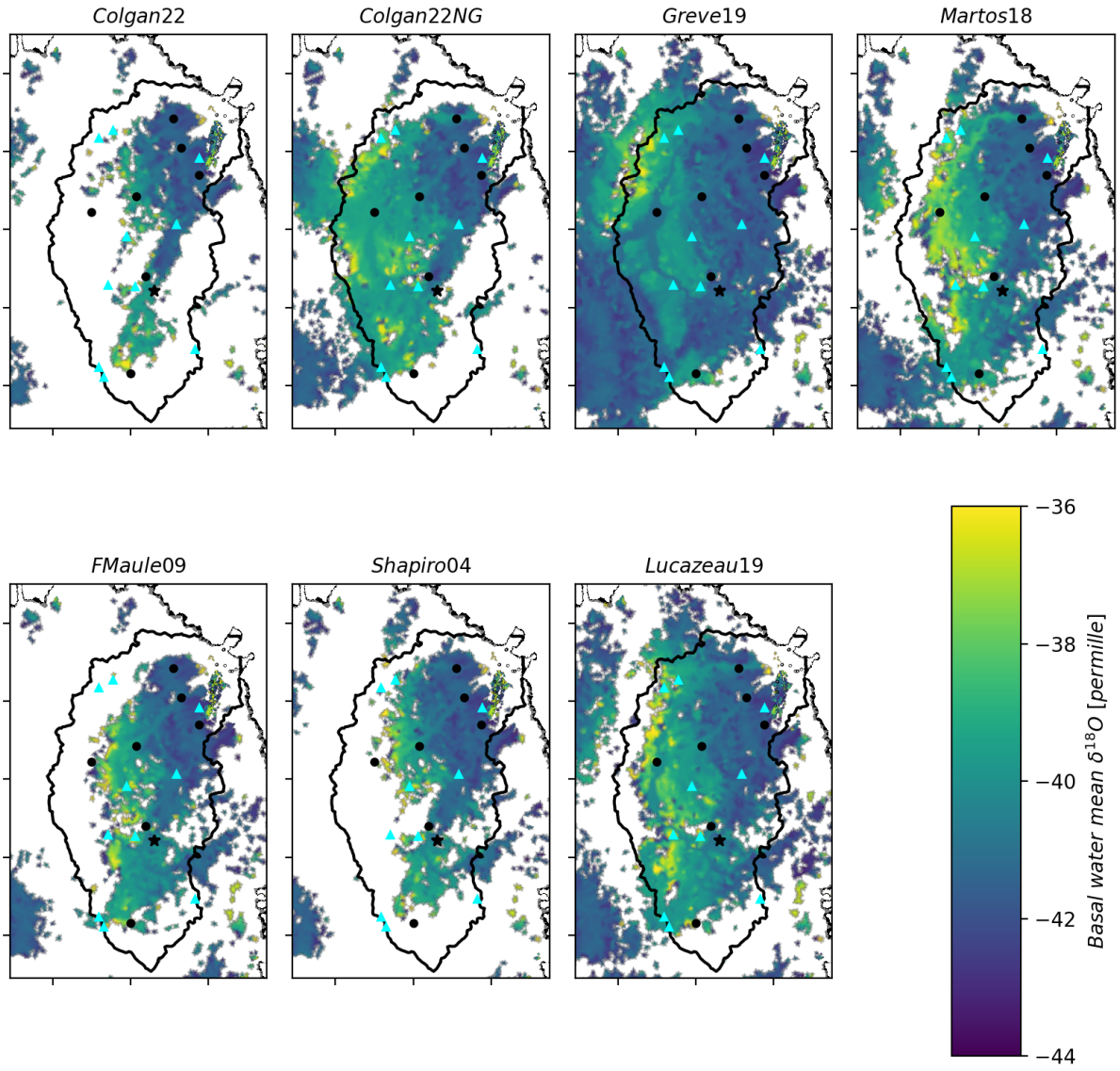

Figure 4.8: Mean isotope composition of the routed and mixed basal meltwater in the NEGIS area for the GHF estimates. White indicates areas with no basal melt. Colorbar indicates delta18O values in ‰. Arrangement of Cs and Ts as in figure 3.12. Black star indicates location of EGRIP. Black outline indicates NEGIS drainage area.

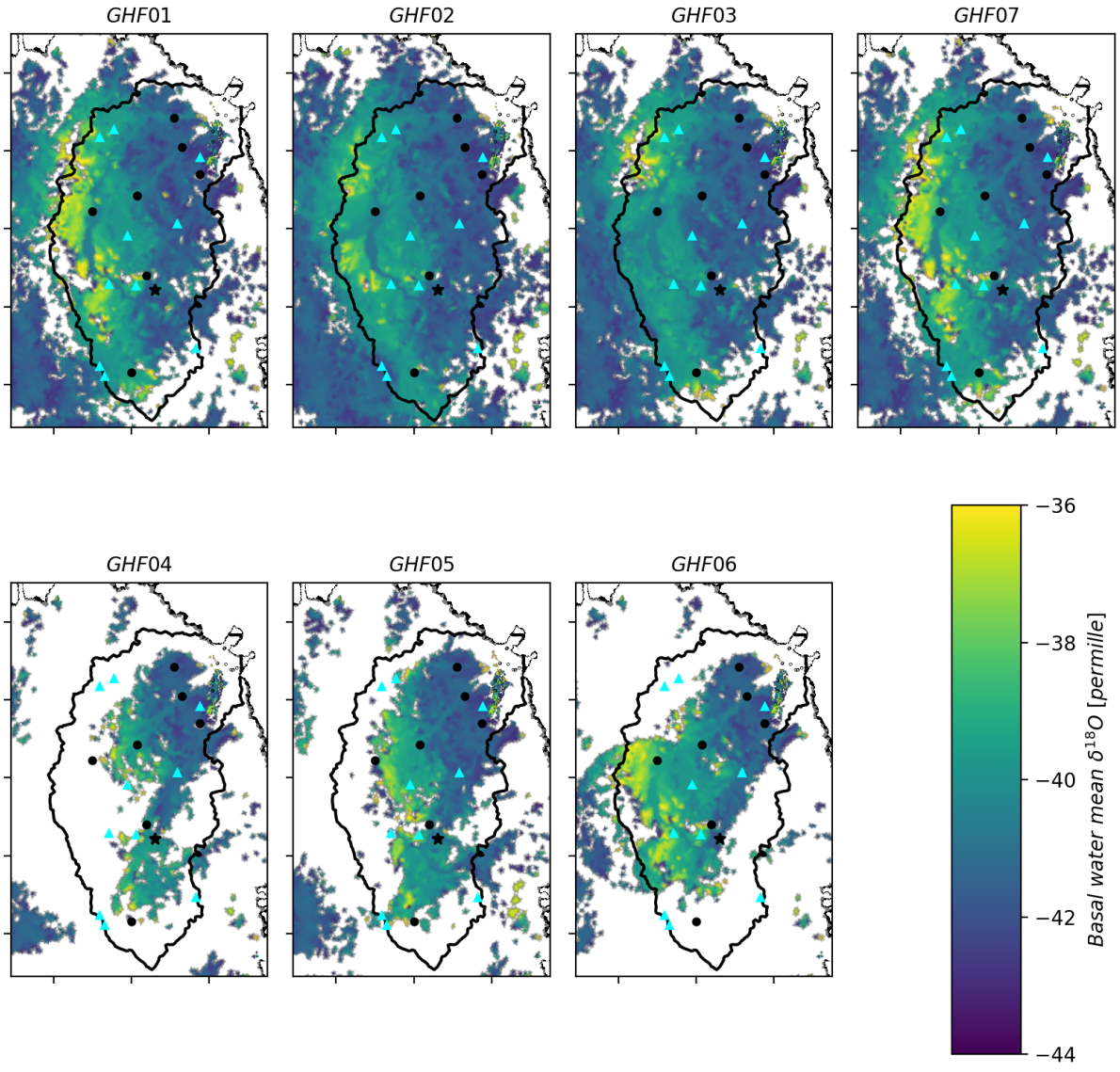

Figure 4.9: Same as figure 4.8 but for the synthetic GHFs.

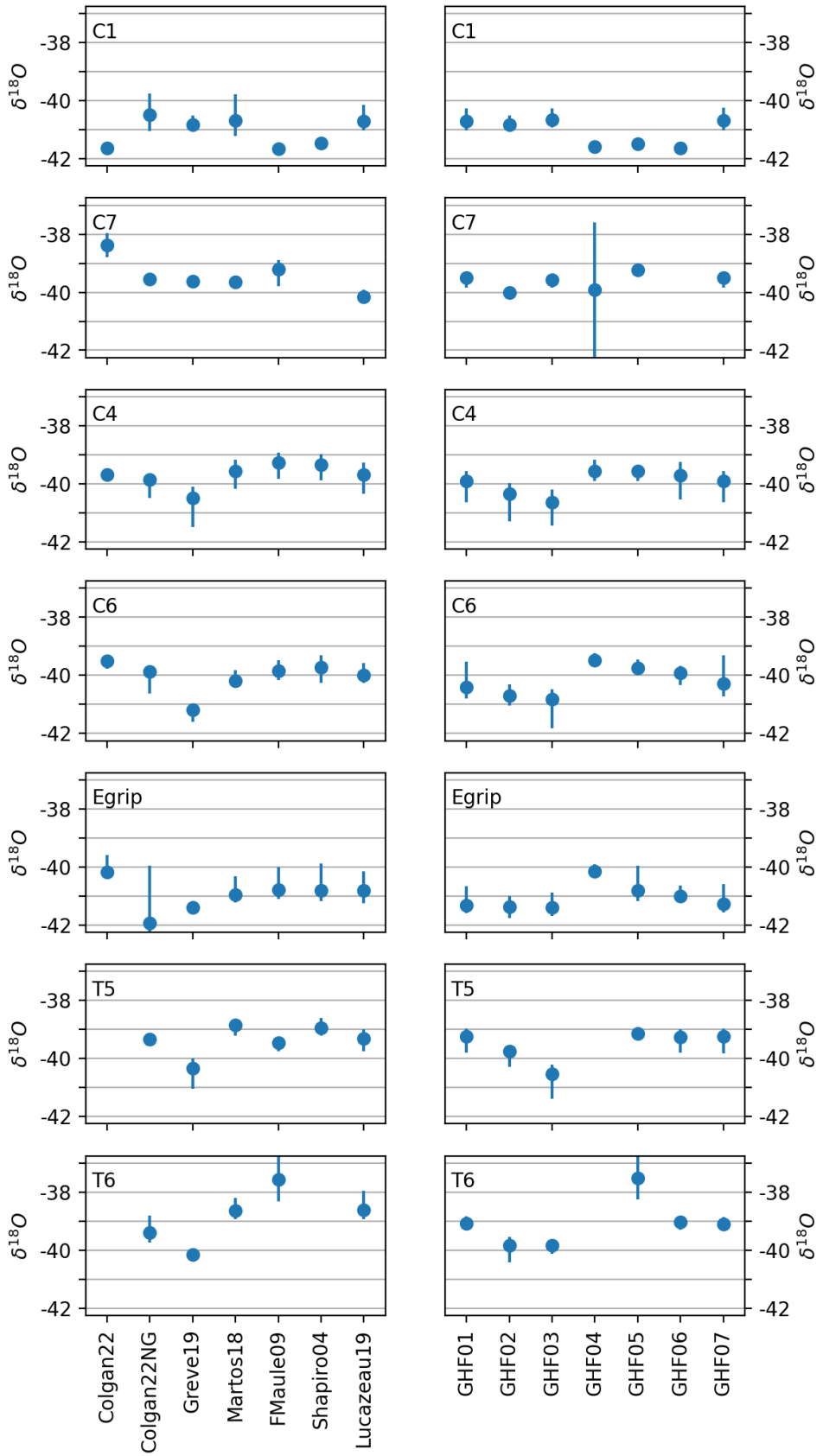

Figure 4.10: Mean isotope values of routed basal water at selected locations. Some GHF scenarios miss values for specific analysis locations, these are located in areas with frozen base in that scenario. Vertical bars give error estimate calculated from the different floatation scenarios. Left column: GHF estimates; Right column: Synthetic GHF experiments.

Chapter 5

Discussion

The results of the analysis presented in chapter 4 show that differences in geothermal heat flux do indeed result in differences in stable isotope composition of the basal meltwater in Greenland. Inferring heat flux in Greenland from stable isotope analysis of meltwater samples thus seems to be a promising concept. In the following sections, the results will be discussed in detail. It is shown that the controlling factor of basal water isotope composition is not so much geothermally induced differences in meltwater area or production as envisioned in the concept of the methodology but rather the dependence of the basal extent of Eemian ice on geothermally induced basal melting rates and the degree to which it lies inside the drainage area of the subglacial water system. Analysis location seems to have an influence on the presence of a geothermally induced isotope signal in the basal meltwater owing to the spatial structure of the subglacial drainage. Isotope values at analyzed sampling locations around EGRIP show strong variability in response to different heat flux estimates which is promising since there might be the possibility to actually obtain a basal water sample there.

Seeing as the purpose of this thesis is to evaluate the feasibility of refining Greenland geothermal heat flux estimates from stable isotope signals and not to actually perform such an analysis, several concepts of ice sheet structure and water flow dynamics were simplified in the methodology. To actually use this method in a study, more sophisticated alternatives to each step of the methodology would need to be considered. These are also discussed.

Finally, the potential of other proxies is discussed that could be used in a similar manner to gain insight into GHF distribution in Greenland. Although the ice cores record other isotopes and other markers like major ions that could be employed in conjunction with the oxygen isotopes to reinforce their signal, the discussion will focus on potentially independent proxies originating from other processes, in particular chemical wheathering at the base and basal microbial activity.

5.1 Interpretation of results

Modern instruments for the measurement of stable isotopes are able to resolve differences between samples of less than 0.1 ‰ for δ^{18}O (e.g., PICARRO, INC., 2017; Masson-Delmotte et al., 2006). At some of the analysis locations, the different GHF scenarios do produce variations that are on that scale, so they could theoretically be resolved and included in an analysis. However seeing as the sensitivity of the results to model set-up and parameter choice is not evaluated at all in this thesis, it would not be appropriate to interpret the results on such a fine scale. Parameters like the grid resolution, the inversion of the basal friction parameter, or the chosen rheology all influence the behaviour of the ice in the simulations and might produce slight variations in the simulated basal meltrate. In extension, this influences the age model which is calculated from the meltrate and thus the isotope composition of the basal ice. The mixing of isotope values in basal water depends on the volume of water and thus also on the meltrate. The chosen hydrology model further influences the mixing of isotope values in the subglacial water system.

The plots of the basal isotope data in figure 4.10 span a range of 5 ‰ which is about half the range of the isotope values in the reconstructed NGRIP δ^{18}O record that the isotope composition of the basal ice is based on (see figure 3.5). Variations in basal water isotope values and patterns thereof that are discernible on a such comparatively large scale should be relatively insensitive to the exact setup of the model. This scale is therefore probably more appropriate for the interpretation of the isotope data in the context of this thesis. The interpretation will thus be largely qualitative rather than quantitative and mostly be concerned with patterns in the variation of basal isotope values that are visible between the different GHF scenarios rather than trying to establish an actual relationship between the exact isotope values and heat flux.

At C1 (C denoting the black circle analysis locations, T the blue triangle locations), which is at the downstream end of the northern drainage path (see figure 3.12, GHF04-06 show lower isotope values that are clearly distinguishable from the values produced by GHF01-03. GHF04-06 are identical to GHF01-03 in their spatial heat flux distribution patterns, only 30 mW/m^2 lower. Because of the lower heat flux the simulated melt area is much smaller and doesn't extend into the central part of northern Greenland where the Eemian ice is. Presumably, because of the smaller extent of the melt area relatively more water is being sourced from the outer (Weichselian) regions of the basal ice where isotope values are generally lower. For the larger melt areas, relatively more water is being sourced from the central part of Greenland where isotope values are generally higher. Thus, this location seems to be sensitive to how far the melt area extends into the centre of the ice sheet. Seeing as there is little variation in isotope signal between the respective three variations of the

high- and low-background heat flux scenarios (70 and 40 mW/m^2 background heat flux, respectively), the isotope signal here might be an indicator of mean or general background heat flux values.

Similar observations can be made for the GHF estimates as well. Colgan22, FMaule09, and Shapiro04 show lower heat fluxes in northern Greenland than the other four (Colgan22NG, Greve19, Martos18, Lucazeau19) and consequently simulate smaller melt areas around NEGIS. Their basal isotope values at C1 are distinctly lower than in the scenarios with higher heat flux in central northern Greenland.

Additionally, the isotope values of Colgan22NG, Greve19, Martos18, Lucazeau19 don't differ much from each other at C1, reinforcing the interpretation that this location isn't sensitive to the scale of any high heat flux anomaly, just high heat flux in general or mean/background heat flux of that region. This might be because after a certain threshold heat flux is passed, (1) the melt area becomes larger than the NEGIS drainage area and the meltwater from regions outside will be routed to other outlets and thus not contribute to the isotope signal at C1, and (2) above a sufficiently high heat flux all the Eemian ice will be melted away as the Nye+melt age model depends on the basal meltrate and so water sourced from that area will contribute a lower isotope signal to the composite water at C1. The latter point is consistent with observations made at NGRIP, where no Eemian ice has remained at the base of the ice core because of the large basal meltrates observed there (Grinsted and Dahl-Jensen, 2002).

The same observations can not be made at C3, which is located at the downstream end of the middle drainage path (isotope values for C3 are shown in Appendix A). The isotope signals at this point are not distinguishable from each other with certainty. Figure 3.12 shows that the middle drainage path doesn't reach as far inland as the northern drainage path for most of the floatation scenarios. Therefore, there is not as much basal meltwater from central northern Greenland contributing to the isotope signal at this location and it is thus not sensitive to the upstream extent of the melt area in the same way as C1, despite its relatively close proximity.

C7 is quite far upstream in the drainage system and very close to the edge of the melt area for all the GHF estimates (for Shapiro04, it is even outside of the melt area). This means that basal water isotope values at this location should be very close to those of the basal ice since there is not much possibility for any mixing in of upstream signals. Consequently, isotope values at this point should be closely related to local heat flux. Colgan22 shows a distinctly higher isotope value at this point than the other GHFs, presumeably corresponding to its generally lower heat flux. FMaule09 and Lucazeau19 likewise seem to be

distinguishable from the rest, but not as clearly.

In the EGRIP area, there are a few locations that show similar patterns in the isotope variability: EGRIP itself, C4, C6, as well as T5 and T6. Looking at the structure of the drainage pathways there (see figure 3.12), it can be seen that C6 is right below the point where the bulk of the southern upstream tributaries converge to form the southern major drainage path, so this point sources water from most of the southern region of the melt area. EGRIP on the other hand is to the east and upstream of that point and only sources water from a small eastern tributary, T6 similarly only sources water from a small western tributary. C4 and T5 are part of the middle drainage path and source water from the central and western region of the drainage basin.

For GHF01-03, isotope values don't show any variability at EGRIP, only GHF04-06 are distinguishable. Since EGRIP sources water from the east, it is presumably relatively immune to heat flux anomalies in the central part of Greenland (which is to the west). However, C6 likewise doesn't show much variability for GHF01-03. In figure 4.9, it can be seen that for these heat fluxes the melt area covers the entire southern part of the drainage basin where C6 sources its water from. Similarly as for C1, it seems that above a certain threshold heat flux isotope values will not vary anymore because the melt area is large enough to cover the entirety of the source area and most of the Eemian ice is melted away.

At C4, the response of isotope values seems to be opposite to C6. GHF01-03 are distinguishable with some uncertainty, but GHF04-06 are not. Because C4 is part of the middle drainage pathway it sources more water from the western part of the drainage basin where the bulk of the Eemian ice is located. Thus, this point seems a bit more sensitive to high heat flux anomalies in central north Greenland, presumably dependent on how much of the Eemian ice is still present there based on the age estimate. Interestingly, for smaller extents of the melt area as for GHF04-06, variability in the extent to the west doesn't seem to have great influence on the isotope signal, seeing as the isotope values for GHF04-06 are quite similar to each other. Looking at the plot of the basal water isotope values (see figure 4.9), it seems that smaller extent of melt area resulting from lower basal melt is somewhat balanced out by larger extent of older ice with higher isotope values.

The observations made for the synthetic GHFs are consistent with the GHF estimates as well. In locations C4, C6, T5 and T6, the Greve19 GHF with its large heat flux anomaly in central north Greenland creates isotope values that are distinctly lower than the ones produced by the other GHFs. For the other GHFs, it seems again that smaller extent of melt area is largely balanced out by presence of higher isotope values at the western boundary of the melt area, so lower heat fluxes don't create much variability in isotope signal compared

to each other.

Judging from these observations, it seems that isotope values at the selected locations are at least sensitive to heat flux variations in the central part of northern Greenland and perhaps mean/background heat flux in general. If the method is further refined it could therefore contribute to the discussion about a potential GHF hotspot in that region and potentially shed some light on the basal conditions underneath NEGIS.

5.2 Choice of location

The choice of analysis location seems to have a large influence on the kind of information basal meltwater isotopes can provide about GHF. Locations toward the ice margin (e.g., C1) are farther downstream in the drainage system and integrate a larger meltarea into their isotope signal. Consequently, these locations don't provide as much information about local variabilities in the heat flux distribution but rather contain a composite isotope of large areas that depends more on the overall mean or background GHF in that area.

Locations farther upstream in the drainage system integrate a much smaller meltarea into their isotope signal and are hence more capable of discerning local features of heat flux present in the area of their location (e.g., EGRIP, C6, C7, T6). The information that can be inferred from these locations is thus more specific about the magnitude of local heat flux but also restricted to a smaller area. A combination of upstream and downstream analysis locations might therefore be optimal to infer as complete information on GHF as possible. However, choice of analysis location ultimately depends on the research question as different locations provide insight into different features of GHF.

The choice of appropriate analysis location is however complicated by the subglacial hydrology. Even though locations Egrip, C6, and T6 are located in close proximity to each other and show similar patterns in the variability of isotope values, the isotope values they show for each GHF scenario differ markedly between the locations. This is due to the complex spatial structure of the subglacial drainage system. Despite their close proximity, the areas where the locations source water from differ greatly. So even though the isotope values at each location react similarly to the different GHFs, values at one location are generally higher or lower than at the other two locations.

This increases uncertainties since it would be difficult or even impossible to constrain the precise location within the drainage system in case of an actual drilling campaign. This is perhaps less of an issue in areas that are more downstream in the drainage basin where

most of the upstream tributaries have already converged into a single drainage path. Even sampling meltwater exiting the outlets at the ice sheet margin might be a reasonable option, as these locations at the very end of the drainage essentially summarize all isotope information of their source areas. But in the case of the EGRIP drillsite and the surrounding region, which is located in the upstream area of the drainage path where most tributaries are still separate from each other, precise choice of analysis location seems to be very important to be able to relate an isotope value to a certain heat flux feature.

5.3 Caveats in the methodology

The attentive reader may have noticed several shortcuts in the methodology that were taken in spite of the better knowledge outlined in the background section. These concern the simulation of the subglacial hydrological system, the modelling of the basal age, and the modelling of the isotopic composition of the basal ice.

Subglacial hydrology

The basal hydraulic gradient is simulated based on the Shreve approximation of the subglacial hydropotential (see section 2.4). This approximation assumes that the hydropotential is determined solely through the geometry of the ice sheet itself. It accounts only for the topography of the bed to calculate the elevation potential of the water and thickness of the ice to calculate the overburden pressure. This is a common approach (e.g., Karlsson and Dahl-Jensen, 2015; Karlsson et al., 2021; Chu et al., 2016; Lindbäck et al., 2015; Rippin et al., 2003), but it disregards the actual movement of water through the subglacial medium which substantially influences the local shape of the hydropotential.

The Shreve approximation is based on the assumption that subglacial water pressure is in balance with the ice overburden pressure Shreve (1972), i.e., that effective pressure is null (or spatially homogeneous if floatation fractions are used). In reality, influx and outflux of water alter the local effective pressure as they raise or lower the water pressure in relation to the overburden. This modulates the local shape of the hydropotential substantially. It is well known from studies of alpine glaciers that the subglacial drainage system changes through the seasons in response to increased meltwater input during summer switching from a distributed to a channelized drainage system as basal water flux increases (e.g., Nienow et al., 1998; Burkimsher, 1983; HOCK and HOOKE, 1993). Similarly, Bartholomew et al. (2011) show that seasonal changes in surface meltwater production drive the spatial evolution of the subglacial drainage system in the ablation zone of an outlet glacier in Greenland. By mapping water conduits in a glacier, Gulley et al. (2012) found conduits originating

in places that the Shreve approximation predicts as low-spots in hydropotential. These areas coincided with moulins and experienced significant recharge through surface meltwater conducted to the base. The authors concluded that recharge location is the larger controlling factor in conduit location rather than Shreve hydropotential. Catania and Neumann (2010) found large and stable englacial drainage features in glaciers in Greenland that persist over several years and originate at moulin-fed recharge locations.

Furthermore, spatial heterogeneities in hydraulic conductivity exert large influence on the flow direction of water as conductivity modulates the drainage speed. In their conduit-mapping study, Gulley et al. (2012) found that water conduits were often oriented at oblique angles to contours of the Shreve hydropotential, sometimes even running perpendicular to the theoretical hydraulic gradient. Overall, the drainage system still followed the hydropotential set by the glacier geometry on the large scale, but locally the direction of water flow was heavily influenced by variabilities in conductivity.

In summary, the Shreve approximation assumes effective pressure to be homogeneous underneath the entire ice covered area. This implicitly assumes that local variations in the amount of recharge will be balanced out by changes in conductivity to maintain constant effective pressure. Both recharge and conductivity thus lose their influence on the shape of the hydropotential and are neglected (de Fleurian, 2023).

Input of surface water to the base through moulins in Greenland is obviously largely limited to the ablation area around the ice sheet margin. However, the principle of recharge controlling the effective pressure holds true even for the much smaller rates of basal meltwater production in the interior of Greenland. This means that different distributions of basal melt caused by different heat flux distributions would result in differences in the spatial structure of the subglacial drainage system. In an analysis of the subglacial drainage as a response to heat flux, it would therefore be prudent to simulate the basal hydrological system with an actual hydraulic simulation that accounts for the effects of water influx and conductivity. This may result in subglacial drainage structures that are different between the individual GHF scenarios, but the improved water flow dynamics and the interaction of the water with the ice are critical to obtain basal water isotope signals that are as close to reality as possible. However, the more complex hydrology models also require input of more parameters, such as a conductivity field if that is to be taken into account. As all subglacial variables, data to constrain those parameters might be difficult to obtain. Hence, more complex hydrology models, while critically improving the actual water flow simulation and basal water isotope mixing, the necessary choice of parameters might re-introduce uncertainty that is difficult to quantify.

Constraining the basal ice age

Like the original Nye-model, the Nye+melt model still assumes uniform vertical strain rate everywhere, which is unrealistic in most parts of the ice sheet. Although the basal ages estimated in this thesis are not completely inconsistent with other estimates of the basal age (compare for example the estimate of basal Eemian extent by MacGregor et al. (2015)), other age models based on non-uniform vertical strain rate might predict different basal ages.

Using non-uniform vertical strain rate however does require adaptation of the age model to the ice sheet stratigraphy. In the Dansgaard-Johnsen model for example, age at depth increases if the kinck-height between the upper section with uniform vertical strain rate and the lower section with decreasing strain rate is higher up in the ice (see seciont 2.3.1; Cuffey and Paterson, 2010). Fahnestock et al. (2001) use the Dansgaard-Johnsen approach to model ice age based on dated radio-stratigraphy and adjust the kink-height to fit the estimate to the observations. However, a Dansgaard-Johnsen-plus-melt model currently doesn't exist and would have to be constructed to model basal ice ages in regions of basal melting.

Another age model that has beed successfully used to model ice ages at ice divides is the easyFlow-model (Fischer et al., 2021). This model is based on non-uniform vertical strain rate that decreases exponentially to the base. The exponent can be adjusted to fit the age model to observed stratigraphy. Unlike the Dansgaard-Johnsen model, a version of the easyFlow model that incorporates basal melting does exist and could be used to determine basal ice ages.

Both the Dansgaard-Johnsen and the easyFlow model (in their plus-melt configurations) still assume the ice sheet to be in steady state and depend on the surface accumulation and the basal melting rate. However in contrast to the Nye+melt model, these models can additionally be tuned to fit observed Greenland age stratigraphy. Using these models and tuning them to the stratigraphy estimate of MacGregor et al. (2015) could result in a basal age estimate that is more constrained by the actual structure of the Greenland ice sheet.

In their "without-melt" configurations, the Dansgaard-Johnsen and the easyFlow model both estimate higher age in the deeper parts of the ice than the Nye-model (see figure 5.1). Assuming this would also be the case in the "plus-melt" configurations, this would increase the estimated ages of the basal ice in comparison to what is presented in this thesis. Importantly, this would increase the area covered by Eemian ice. This would be an improvement to the age estimate as the Eemian area estimates in this thesis are generally smaller than published estimates (MacGregor et al., 2015). The method of detecting GHF variations in water

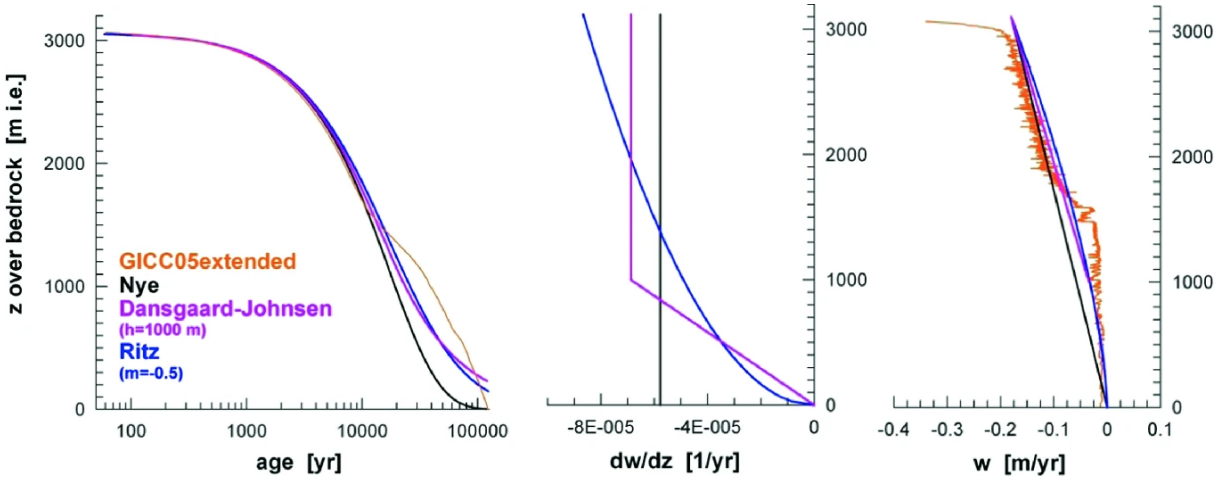

Figure 5.1: Comparison of the depth-age relationship in three common age models. Graphs) Black: Nye-model; Purple: Dansgaard-Johnsen; Blue: easyFlow; Orange: Example of real ice core data. Figures) Left: Plot of age against depth; Middle: Vertical strain rate; Right: Vertical velocity. Figure from Fischer et al. (2021).

stable isotope composition would presumably benefit from this increased Eemian area, as the isotopic composition of Eemian ice is distinctly different from the glacial ice which would potentially increase the amplitude of the GHF-related isotope signals presented in this thesis.

Basal ice isotope composition

The extrapolated isotope composition of the oldest basal ice is hypothetical as the oldest modelled ages (capped at 140 ka) exceed the oldest ages recorded at NGRIP (123 ka). Consequently, no isotope data exist to compare the estimate to and validate it. Isotope values are hence based on a correlation of NGRIP δ^{18}O data to the Vostok CO_2 record. The CO_2 record reconstructs the NGRIP isotope record reasonably well for the Holocene and the glacial period, Eemian isotope values however are too low and do not exceed Holocene values. This is an issue as Eemian isotope values consistently exceed Holocene values by about 3 ‰not only in the NGRIP ice core (Andersen et al., 2004), but also at NEEM (Dahl-Jensen et al., 2013) and GRIP (Landais et al., 2004) and is thus presumably consistent for the entirety of the Greenland ice sheet.

The correlation between NGRIP and Vostok is conceptually based on the established relationship between ice-core δ^{18}O records, climate, and atmoshperic CO_2 (Canadell et al., 2021; Jouzel and Masson-Delmotte, 2007; Masson-Delmotte et al., 2006). Atmoshperic CO_2 exerts great control on global mean temperatures, which in turn affect the isotope fractionation during both evaporation of ocean water and subsequent precipitation of snow. In Greenland ice cores, CO_2 records have been shown to be affected by chemical reactions

with impurities in the ice which lead to in-situ production of CO_2 (ANKLIN et al., 1995). Antarctic ice cores show much lower impurity content than Greenland ice cores, so while in-situ CO_2 production in Antarctic ice cannot totally be excluded it is likely very small (ANKLIN et al., 1995; Stauffer et al., 2003). This and the good agreement in the CO_2 records between different Antarctic ice cores suggest that they do represent a global record of atmoshperic CO_2 evolution (Barnola et al., 1995).

As outlined in the background, section 2.3.2, ice flow influences the values of the vertical profile of isotope values in an ice sheet. Generally, the ice flow is oriented downwards and away from the ice divide. The downwards oriented part dominates for locations close to the ice divide, the outwards oriented flow gains influence with increasing distance from the divide (Cuffey and Paterson, 2010). That means that in the lower parts of a vertical profile through the ice, most ice has been deposited somewhere upstream of that location with deeper ice layers being farther away from their original deposition site.

Extrapolating the isotope values of the entire basal ice from only the NGRIP isotope record is thus a reasonable first estimate (and sufficient for the purposes of this thesis) as the NGRIP site is located on the central ice divide from where large parts of the deepest ice will have likely originated (Gerber et al., 2021; Reeh et al., 2002). Still, the farther away the region is from the central ice divide the farther away from the divide will even the deepest ice have been deposited. This is especially true for basal ice of younger age as that ice has had less time to flow great distances.

In an actual study, effects of the deposition site on the isotope values of the basal ice would need to be considered. Moving the deposition site away from the central ice divide, i.e., more towards the margin of the ice lowers the elevation of the site and thus increases depositional surface temperature and decreases the amount of Rayleigh-fractionation the source-clouds of the precipitation have already experienced. The deposition site of the basal ice can be estimated from particle-flow modelling based on a stratigraphy estimate (Florentine et al., 2018; Clarke and Marshall, 2002; Lhomme et al., 2005).

5.4 Other proxies that can be used for this analysis

The $\delta^{18}O$ of ice is not the only proxy that could be used to constrain GHF in Greenland. All proxies that act as a conservative tracer in the subglacial hydrological system and whose areal distribution is either known or can be constrained in some way can conceptually be used to constrain GHF in the same way as presented in this thesis.

There are three possible sources of tracers:

1) The stratigraphy of the Greenland ice sheet. Similar to the δ^{18}O, all substances that are deposited in the ice and show a distinct record can be used in the same way as outlined in this thesis by constraining their areal distribution through their relation to the age of the ice.
2) Products of basal wheathering at the base. The extent and amount of chemical wheathering at the ice-bed interface depends on the presence of liquid water and is controlled by the type of hydrological drainage system. Chemical wheathering thus depends on the basal thermal state which is controlled by the GHF.
3) Biological activity at the ice sheet base is likewise dependent on the availability of water and the thermal conditions, as these determine the availability of nutrients and the type of microbes that can thrive in a given basal environment.

Other stratigraphic proxies that are recorded in the ice cores depend on the distribution of GHF in the same way as the δ^{18}O that was used in this thesis. They might thus not be independent proxies, i.e., not give a GHF-related signal that is independent to the δ^{18}O signal depending on the temporal evolution of their signal in the ice core record. They might however be useful to reinforce the signal obtained from stable isotopes. As their response to GHF variations would conceptually be similar to what is shown in this thesis, they will not be considered in depth in the following discussion.

Chemical wheathering:

The basal thermal regime has strong control over the potential for and the amount of chemical wheathering underneath the Greenland ice sheet (as summarized by Tranter and Wadham, 2014). This is because the thermal regime controls the presence and amount of liquid water underneath the ice sheet and hence the type of subglacial drainage system that will develop. In the melt areas in the interior of ice sheets, distributed drainage systems are thought to be dominant, in which water moves slowly towards larger channels. Because of the slow water flow, distributed drainages show high rock-water contact times as well as high rock:water ratios, due to the overall small amount of basal water. Distributed drainage systems hence often produce glacial meltwaters that are highly concentrated in chemical wheathering products.

Studying Mg/Na and Ca/Na ratios as tracers of chemical wheathering of the bedrock underneath the Greenand ice sheet, Urra et al. (2019) found differences in chemical proxies that indicate carbonate- vs silicate- mineral dominated wheathering in the meltwater from different glaciers in south-western Greenland. High Mg/Na and Ca/Na ratios indicate carbonate wheathering, low Mg/Na and Ca/Na ratios indicate silicate wheathering. However, the Greenland bedrock has very low concentrations of carbonates, which can be inferred from overall low Ca and Mg weathering yields. They argue instead that the variability in

the proxy data may be explained by the age of the underlying bedrock. The mobility of Ca, Mg and Si in rock increases over time, so older rocks may be enriched in Mg and Ca compared to Na. If the age distribution of the Greenland crust could be constrained, the information provided by these proxies could be used to constrain the basal drainage system in a similar way as the δ^{18}O values of the ice in this thesis. Celli et al. (2021) produced an estimate of the structure of the Greenland crust based on seismic waveform tomography and were able to image the individual Greenland cratons in detail. This data set has been used by Colgan et al. (2022) in the production of their GHF-estimate and could be used to at least roughly constrain the age distribution of the Greenland bedrock.

Biological activity:

Studying the biogeochemistry of subglacial environments, Dubnick et al. (2020) found that the basal ice of glaciers with temparate bases is significantly enriched in microbial content, dissolved organic matter, and major ions compared to cold-based glaciers. They argue that the basal thermal regime is a dominant control on the basal biological environment through its influence on basal erosion and the connected mobilization of nutrients. The distribution of microbial activity underneath the Greenland ice sheet hence depends on the geothermal heat flux. The basal microbes are characteristic for the basal environment. More than 75 % of the identified species were absent from the glacial ice column. The biochemical products of these assemblages could thus be used as proxies to identify basal water in a sample. Furthermore, the authors found high spatial variability in the composition of the microbial communities rendering them potentially useful as tracers of the subglacial drainage system similar to basal ice δ^{18}O.

Chapter 6

Conclusion

The aim of this thesis was to test the feasibility of using basal meltwater stable isotope composition to infer information about geothermal heat flux distribution in Greenland. Through simulating the response of the Greenland ice sheet to different heat flux scenarios and modelling the resulting basal meltwater δ^{18}O values, it could be shown that the isotope composition of the basal water system is influenced by the geothermal heat flux. The variability in resulting δ^{18}O values between the GHF scenarios is on an order that is easily measurable with modern instruments. Isotope variability and resulting signal strength depend however heavily on the sampling location depending on the structure of the basal water system. Overall, the method seems to be able to detect at least large scale features of GHF such as a potential hotspot in central northern Greenland or general magnitude of background heat flux. In a study trying to employ this method on real data, more sophisticated models would need to be used in the simulations as several simplifications have been assumed for the purpose of testing the novel approach. However judging from the results presented in this thesis, infering geothermal heat flux from meltwater stable isotope composition seems to be a promising approach and may be applied in future studies.

Appendix A

Isotope values of all analysis locations

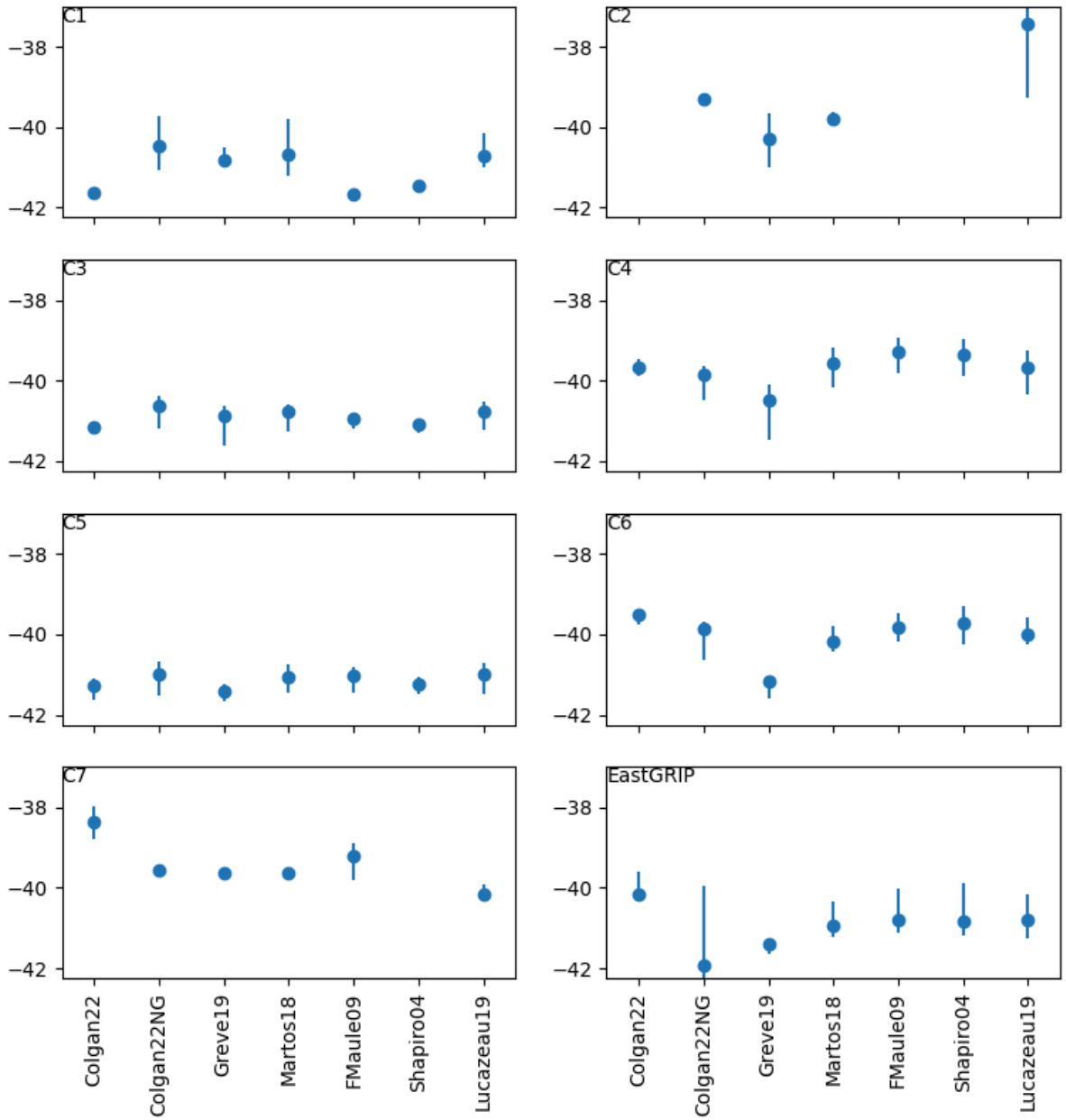

Figure A.1: All isotope data from black circle locations for the GHF estimates.

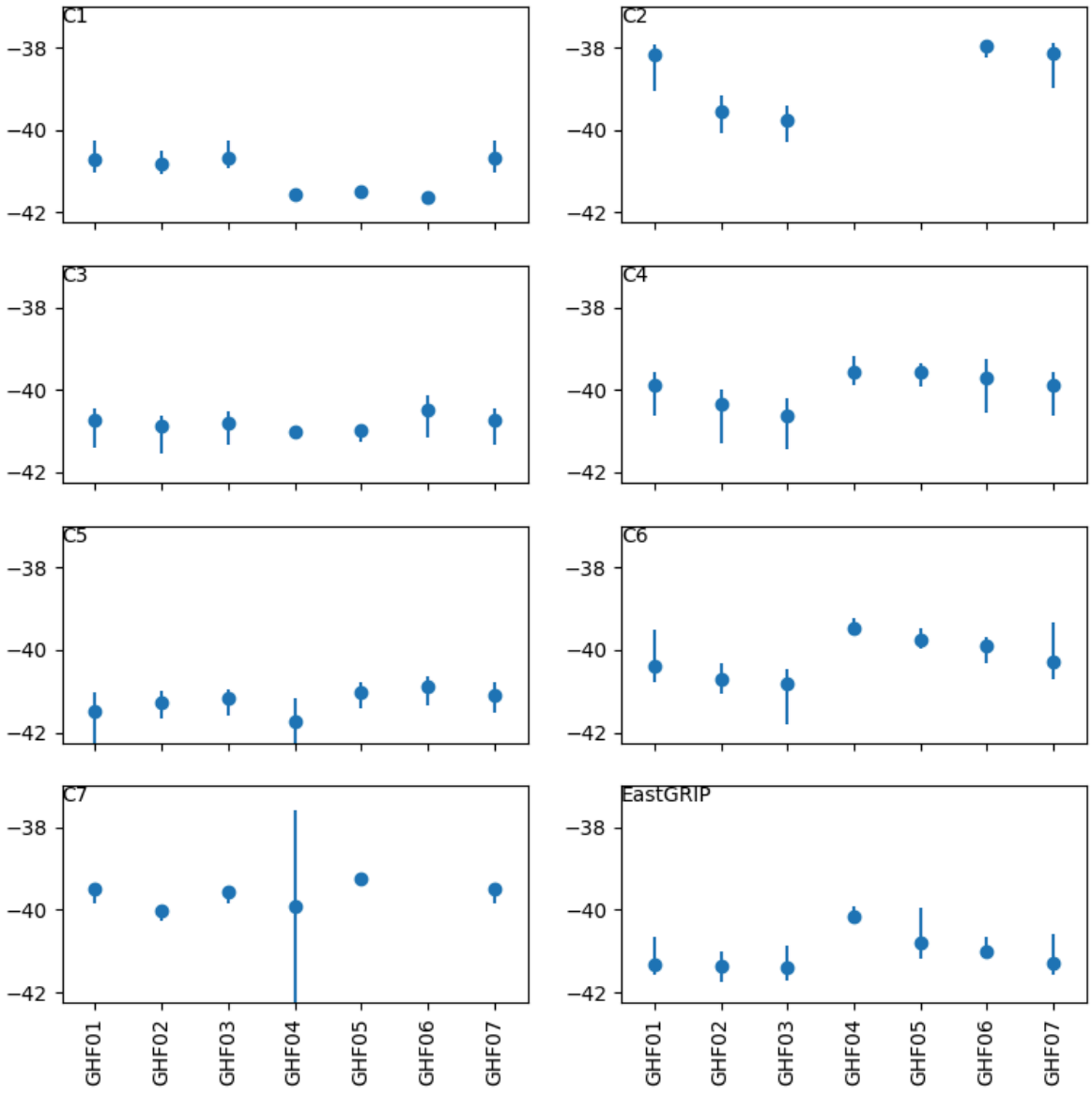

Figure A.2: All isotope data from black circle locations for the synthetic GHF.

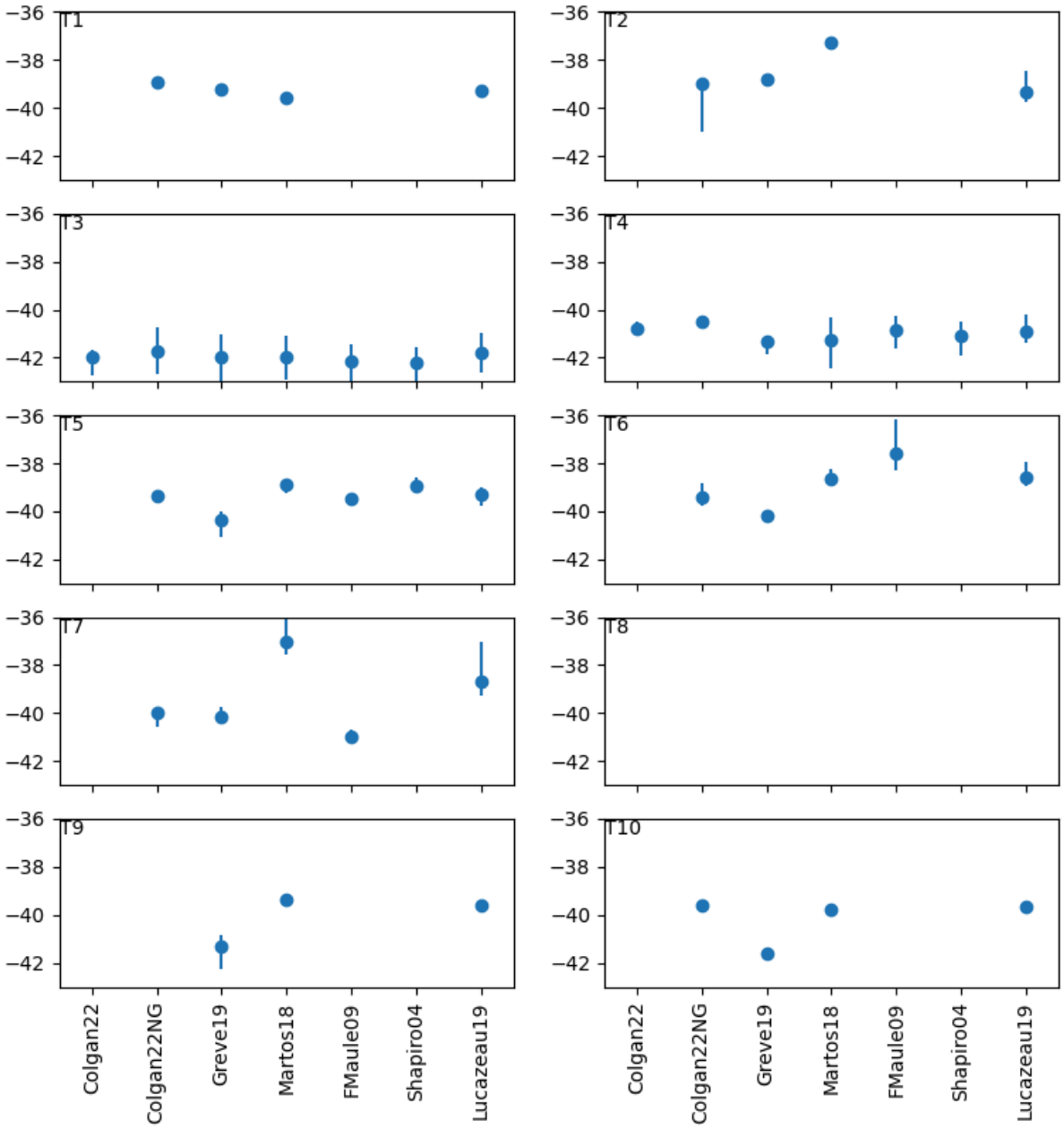

Figure A.3: All isotope data from blue triangle locations for the GHF estimates.

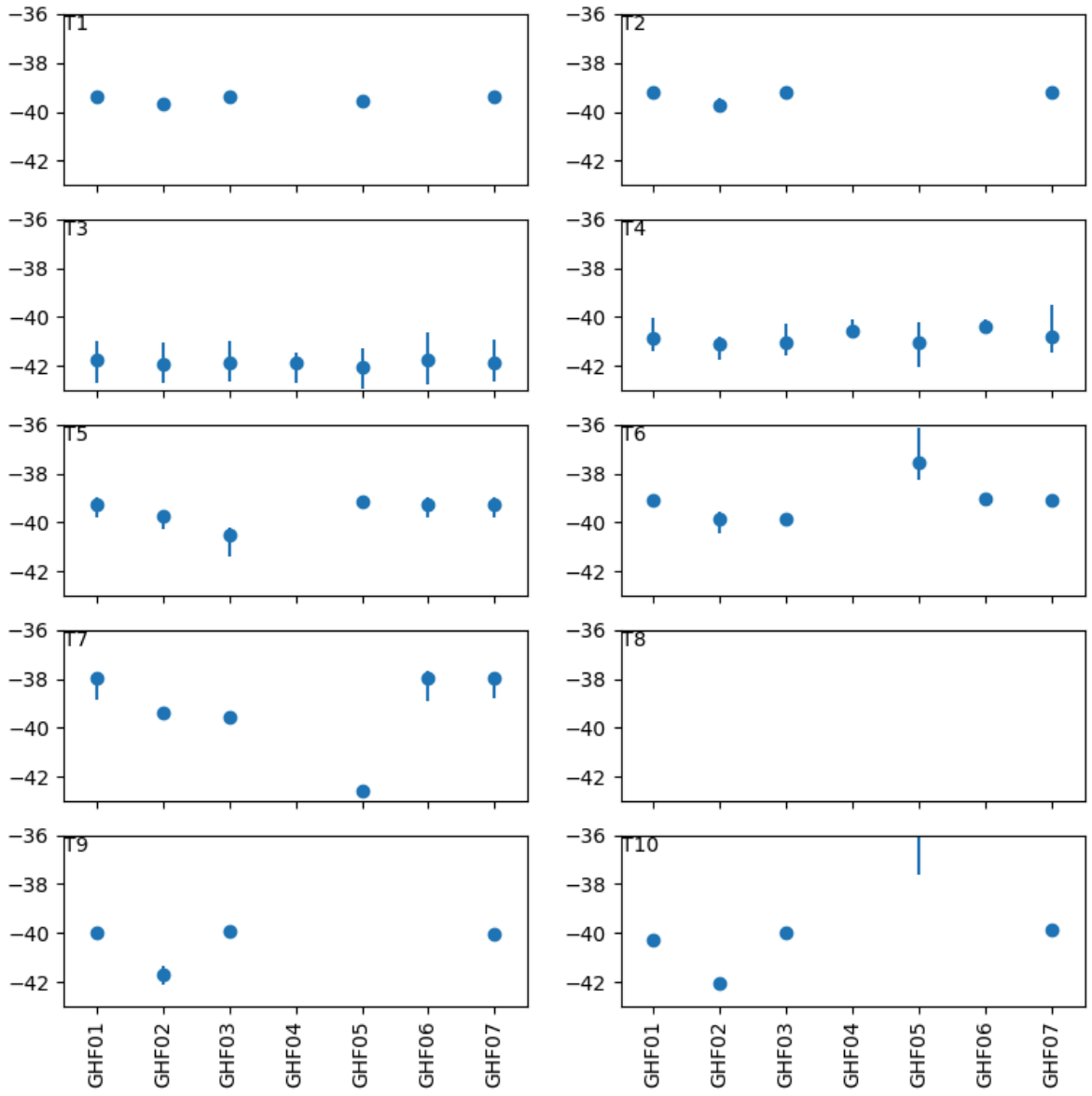

Figure A.4: All isotope data from blue triangle locations for the synthetic GHF.

Bibliography

Andersen, K. K., N. Azuma, J. M. Barnola, M. Bigler, P. Biscaye, N. Caillon, J. Chappellaz, H. B. Clausen, D. Dahl-Jensen, H. Fischer, J. Flückiger, D. Fritzsche, Y. Fujii, K. Goto-Azuma, K. Grønvold, N. S. Gundestrup, M. Hansson, C. Huber, C. S. Hvidberg, S. J. Johnsen, U. Jonsell, J. Jouzel, S. Kipfstuhl, A. Landais, M. Leuenberger, R. Lorrain, V. Masson-Delmotte, H. Miller, H. Motoyama, H. Narita, T. Popp, S. O. Rasmussen, D. Raynaud, R. Rothlisberger, U. Ruth, D. Samyn, J. Schwander, H. Shoji, M. L. Siggard-Andersen, J. P. Steffensen, T. Stocker, A. E. Sveinbjörnsdóttir, A. Svensson, M. Takata, J. L. Tison, T. Thorsteinsson, O. Watanabe, F. Wilhelms, J. W. C. White, and North Greenland Ice Core Project members (2004). High-resolution record of northern hemisphere climate extending into the last interglacial period. *Nature 431*(7005), 147–151. 19, 31, 53, 73

Andrews, L. C., G. A. Catania, M. J. Hoffman, J. D. Gulley, M. P. Lüthi, C. Ryser, R. L. Hawley, and T. A. Neumann (2014). Direct observations of evolving subglacial drainage beneath the greenland ice sheet. *Nature 514*(7520), 80–83. 23

ANKLIN, M., J.-M. BARNOLA, J. SCHWANDER, B. STAUFFER, and D. RAYNAUD (1995). Processes affecting the co2 concentrations measured in greenland ice. *Tellus B 47*(4), 461–470. 74

AntarcticGlaciers.org (2023). Sketch of the stresses in a moving glacier. *https://www.antarcticglaciers.org/glacier-processes/glacier-flow-2/glacier-flow-ii-stress-and-strain/*, Accessed on 30. March 2023. 6

Artemieva, I. M. (2019). Lithosphere thermal thickness and geothermal heat flux in greenland from a new thermal isostasy method. *Earth-Science Reviews 188*, 469–481. 11, 12, 13

Aschwanden, A., E. Bueler, C. Khroulev, and H. Blatter (2012). An enthalpy formulation for glaciers and ice sheets. *Journal of Glaciology 58*(209), 441–457. 26

Azuma, N. and A. Higashi (1984). Mechanical properties of dye 3 greenland deep ice cores. *Annals of Glaciology 5*, 1–8. 14

Banwell, A. F., I. C. Willis, and N. S. Arnold (2013, 2023/03/20). Modeling subglacial water routing at paakitsoq, w greenland. *Journal of Geophysical Research: Earth Surface 118*(3), 1282–1295. 22, 23

Barnola, J. M., M. Anklin, J. Porcheron, D. Raynaud, J. Schwander, and B. Stauffer (1995). Co2 evolution during the last millennium as recorded by antarctic and greenland ice. *Tellus B: Chemical and Physical Meteorology 47*(1-2), 264–272. 74

Bartholomew, I., P. Nienow, A. Sole, D. Mair, T. Cowton, S. Palmer, and J. Wadham (2011, 2023/03/27). Supraglacial forcing of subglacial drainage in the ablation zone of the greenland ice sheet. *Geophysical Research Letters 38*(8). 70

Bazin, L., A. Landais, B. Lemieux-Dudon, H. Toyé Mahamadou Kele, D. Veres, F. Parrenin, P. Martinerie, C. Ritz, E. Capron, V. Lipenkov, M.-F. Loutre, D. Raynaud, B. Vinther, A. Svensson, S. O. Rasmussen, M. Severi, T. Blunier, M. Leuenberger, H. Fischer, V. Masson-Delmotte, J. Chappellaz, and E. Wolff (2013). An optimized multi-proxy, multi-site antarctic ice and gas orbital chronology (aicc2012): 120ndash;800 ka. *Climate of the Past 9*(4), 1715–1731. 19, 53

Benn, D. and D. Evans (2010). *Glaciers and Glaciation, 2nd edition* (2 ed.). London. 5, 6, 7, 20, 21

Blatter, H. (1995). Velocity and stress fields in grounded glaciers: a simple algorithm for including deviatoric stress gradients. *Journal of Glaciology 41*(138), 333–344. 26

Blunier, T., R. Spahni, J.-M. Barnola, J. Chappellaz, L. Loulergue, and J. Schwander (2007). Synchronization of ice core records via atmospheric gases. *Climate of the Past 3*(2), 325–330. 31

Bons, P. D., T. de Riese, S. Franke, M.-G. Llorens, T. Sachau, N. Stoll, I. Weikusat, J. Westhoff, and Y. Zhang (2021). Comment on "exceptionally high heat flux needed to sustain the northeast greenland ice stream" by smith-johnsen et al. (2020). *The Cryosphere 15*(5), 2251–2254. 13

Boral, S., I. S. Sen, D. Ghosal, B. Peucker-Ehrenbrink, and J. D. Hemingway (2019). Stable water isotope modeling reveals spatio-temporal variability of glacier meltwater contributions to ganges river headwaters. *Journal of Hydrology 577*, 123983. 41

Burkimsher, M. (1983). Investigations of glacier hydrological systems using dye tracer techniques: Observations at pasterzengletscher, austria. *Journal of Glaciology 29*(103), 403–416. 70

Canadell, J., P. Monteiro, M. Costa, L. Cotrim da Cunha, P. Cox, A. Eliseev, S. Henson, M. Ishii, S. Jaccard, C. Koven, A. Lohila, P. Patra, S. Piao, J. Rogelj, S. Syampungani, S. Zaehle, and K. Zickfeld (2021). Global carbon and other biogeochemical cycles and feedbacks. In V. Masson-Delmotte, P. Zhai, A. Pirani, S. Connors, C. Péan, S. Berger, N. Caud, Y. Chen, L. Goldfarb, M. Gomis, M. Huang, K. Leitzell, E. Lonnoy, J. Matthews, T. Maycock, T. Waterfield, O. Yelekçi, R. Yu, and B. Zhou (Eds.), *Climate Change 2021: The Physical Science Basis. Contribution of Working Group I to the Sixth Assessment Report of the Intergovernmental Panel on Climate Change*, pp. 673–816. Cambridge, United Kingdom and New York, NY, USA: Cambridge University Press. 73

CAPE-Last Interglacial Project Members (2006). Last interglacial arctic warmth confirms polar amplification of climate change. *Quaternary Science Reviews 25*(13), 1383–1400. 19, 53

Catania, G. A. and T. A. Neumann (2010, 2023/03/27). Persistent englacial drainage features in the greenland ice sheet. *Geophysical Research Letters 37*(2). 71

Celli, N. L., S. Lebedev, A. J. Schaeffer, and C. Gaina (2021). The tilted iceland plume and its effect on the north atlantic evolution and magmatism. *Earth and Planetary Science Letters 569*, 117048. 76

Chu, W., T. T. Creyts, and R. E. Bell (2016). Rerouting of subglacial water flow between neighboring glaciers in west greenland. *Journal of Geophysical Research: Earth Surface 121*(5), 925–938. 21, 22, 23, 34, 37, 53, 70

Clark, I. D. and P. Fritz (1997). *Environmental Isotopes in Hydrogeology*. CRC Press. 40

Clarke, G. K. C. and S. J. Marshall (2002). Isotopic balance of the greenland ice sheet: modelled concentrations of water isotopes from 30,000 bp to present. *Quaternary Science Reviews 21*(1), 419–430. 74

Colgan, W., A. Wansing, K. Mankoff, M. Lösing, J. Hopper, K. Louden, J. Ebbing, F. G. Christiansen, T. Ingeman-Nielsen, L. C. Liljedahl, J. A. MacGregor, A. Hjartarson, S. Bernstein, N. B. Karlsson, S. Fuchs, J. Hartikainen, J. Liakka, R. S. Fausto, D. Dahl-Jensen, A. Bjørk, J.-O. Naslund, F. Mørk, Y. Martos, N. Balling, T. Funck, K. K. Kjeldsen, D. Petersen, U. Gregersen, G. Dam, T. Nielsen, S. A. Khan, and A. Løkkegaard (2022). Greenland geothermal heat flow database and map (version 1). *Earth System Science Data 14*(5), 2209–2238. vi, 11, 12, 27, 29, 30, 76

Cuffey, K. M. and W. S. B. Paterson (2010). *The physics of glaciers* (4 ed.). Academic Press. 5, 6, 7, 8, 15, 16, 21, 72, 74

Cuzzone, J. K., M. Morlighem, E. Larour, N. Schlegel, and H. Seroussi (2018). Implementation of higher-order vertical finite elements in issm v4.13 for improved ice sheet flow modeling
over paleoclimate timescales. *Geoscientific Model Development 11*(5), 1683–1694. 27

Dahl-Jensen, D., M. R. Albert, A. Aldahan, N. Azuma, D. Balslev-Clausen, M. Baumgartner, A. M. Berggren, M. Bigler, T. Binder, T. Blunier, J. C. Bourgeois, E. J. Brook, S. L. Buchardt, C. Buizert, E. Capron, J. Chappellaz, J. Chung, H. B. Clausen, I. Cvijanovic, S. M. Davies, P. Ditlevsen, O. Eicher, H. Fischer, D. A. Fisher, L. G. Fleet, G. Gfeller, V. Gkinis, S. Gogineni, K. Goto-Azuma, A. Grinsted, H. Gudlaugsdottir, M. Guillevic, S. B. Hansen, M. Hansson, M. Hirabayashi, S. Hong, S. D. Hur, P. Huybrechts, C. S. Hvidberg, Y. Iizuka, T. Jenk, S. J. Johnsen, T. R. Jones, J. Jouzel, N. B. Karlsson, K. Kawamura, K. Keegan, E. Kettner, S. Kipfstuhl, H. A. Kjær, M. Koutnik, T. Kuramoto, P. Köhler, T. Laepple, A. Landais, P. L. Langen, L. B. Larsen, D. Leuenberger, M. Leuenberger, C. Leuschen, J. Li, V. Lipenkov, P. Martinerie, O. J. Maselli, V. Masson-Delmotte, J. R. McConnell, H. Miller, O. Mini, A. Miyamoto, M. Montagnat-Rentier, R. Mulvaney, R. Muscheler, A. J. Orsi, J. Paden, C. Panton, F. Pattyn, J. R. Petit, K. Pol, T. Popp, G. Possnert, F. Prié, M. Prokopiou, A. Quiquet, S. O. Rasmussen, D. Raynaud, J. Ren, C. Reutenauer, C. Ritz, T. Röckmann, J. L. Rosen, M. Rubino, O. Rybak, D. Samyn, C. J. Sapart, A. Schilt, A. M. Z. Schmidt, J. Schwander, S. Schüpbach, I. Seierstad, J. P. Severinghaus, S. Sheldon, S. B. Simonsen, J. Sjolte, A. M. Solgaard, T. Sowers, P. Sperlich, H. C. Steen-Larsen, K. Steffen, J. P. Steffensen, D. Steinhage, T. F. Stocker, C. Stowasser, A. S. Sturevik, W. T. Sturges, A. Sveinbjörnsdottir, A. Svensson, J. L. Tison, J. Uetake, P. Vallelonga, R. S. W. van de Wal, G. van der Wel, B. H. Vaughn, B. Vinther, E. Waddington, A. Wegner, I. Weikusat, J. W. C. White, F. Wilhelms, M. Winstrup, E. Witrant, E. W. Wolff, C. Xiao, J. Zheng, and N. community members (2013). Eemian interglacial reconstructed from a greenland folded ice core. *Nature 493*(7433), 489–494. 14, 15, 73

Dahl-Jensen, D., N. Gundestrup, S. P. Gogineni, and H. Miller (2003). Basal melt at northgrip modeled from borehole, ice-core and radio-echo sounder observations. *Annals of Glaciology 37*, 207–212. 10

Dahl-Jensen, D. and N. S. Gundestrup (1989). Derivation of flow-law properties from borehole tilt data: Discussion of the dye 3, camp century, and byrd station bore-hole results. *Annals of Glaciology 12*, 200–201. 15

Dahl-Jensen, D., K. Mosegaard, N. Gundestrup, G. D. Clow, S. J. Johnsen, A. W. Hansen, and N. Balling (1998, 2023/03/29). Past temperatures directly from the greenland ice sheet. *Science 282*(5387), 268–271. 10

Dansgaard, W. and S. J. Johnsen (1969). A flow model and a time scale for the ice core from camp century, greenland. *Journal of Glaciology 8*(53), 215–223. 17

Davies, J. H. and D. R. Davies (2010). Earth's surface heat flux. *Solid Earth 1*(1), 5–24. 1, 10

de Fleurian, B. (2023, March). Private communication. 71

de Fleurian, B., O. Gagliardini, T. Zwinger, G. Durand, E. Le Meur, D. Mair, and P. Råback (2014). A double continuum hydrological model for glacier applications. *The Cryosphere 8*(1), 137–153. 21

Dubnick, A., M. Sharp, B. Danielson, A. Saidi-Mehrabad, and J. Barker (2020). Basal thermal regime affects the biogeochemistry of subglacial systems. *Biogeosciences 17*(4), 963–977. 76

Fahnestock, M., W. Abdalati, I. Joughin, J. Brozena, and P. Gogineni (2001). High geothermal heat flow, basal melt, and the origin of rapid ice flow in central greenland. *Science 294*(5550), 2338–2342. 13, 17, 30, 33, 34, 72

Fischer, H., T. Blunier, and R. Mulvaney (2021). Ice cores: Archive of the climate system. In A. Fowler and F. Ng (Eds.), *Glaciers and Ice Sheets in the Climate System: The Karthaus Summer School Lecture Notes*, pp. 279–325. Cham: Springer International Publishing. 17, 33, 34, 72, 73

Florentine, C., J. Harper, J. Johnson, and T. Meierbachtol (2018). Radiostratigraphy reflects the present-day, internal ice flow field in the ablation zone of western greenland. *Frontiers in Earth Science 6*. 74

Flowers, G. E. (2015, 2023/03/20). Modelling water flow under glaciers and ice sheets. *Proceedings of the Royal Society A: Mathematical, Physical and Engineering Sciences 471*(2176), 20140907. 21, 22

Fowler, A. (2021). Thermal structure. In A. Fowler and F. Ng (Eds.), *Glaciers and Ice Sheets in the Climate System: The Karthaus Summer School Lecture Notes*, pp. 29–45. Cham: Springer International Publishing. 8

Fox-Kemper, B., H. Hewitt, C. Xiao, G. Aðalgeirsdóttir, S. Drijfhout, T. Edwards, N. Golledge, M. Hemer, R. Kopp, G. Krinner, A. Mix, D. Notz, S. Nowicki, I. Nurhati, L. Ruiz, J.-B. Sallée, A. Slangen, and Y. Yu (2021). Ocean, cryosphere and sea level change. In V. Masson-Delmotte, P. Zhai, A. Pirani, S. Connors, C. Péan, S. Berger, N. Caud, Y. Chen, L. Goldfarb, M. Gomis, M. Huang, K. Leitzell, E. Lonnoy, J. Matthews, T. Maycock, T. Waterfield, O. Yelekçi, R. Yu, and B. Zhou (Eds.), *Climate Change 2021: The Physical Science Basis. Contribution of Working Group I to the Sixth*

Assessment Report of the Intergovernmental Panel on Climate Change, pp. 1211–1362. Cambridge, United Kingdom and New York, NY, USA: Cambridge University Press. 1

Fox Maule, C., M. E. Purucker, and N. Olsen (2009). Inferring magnetic crustal thickness and geothermal heat flux from crustal magnetic field models. *Danish Climate Centre Report 09-09*. vi, 11, 28, 30

Franke, S., D. Jansen, T. Binder, N. Dörr, V. Helm, J. Paden, D. Steinhage, and O. Eisen (2020). Bed topography and subglacial landforms in the onset region of the northeast greenland ice stream. *Annals of Glaciology 61*(81), 143–153. 5

Gerber, T. A., C. S. Hvidberg, S. O. Rasmussen, S. Franke, G. Sinnl, A. Grinsted, D. Jansen, and D. Dahl-Jensen (2021). Upstream flow effects revealed in the eastgrip ice core using monte carlo inversion of a two-dimensional ice-flow model. *The Cryosphere 15*(8), 3655–3679. 20, 74

Gibbard, P. and M. Head (2020). Chapter 30 - the quaternary period. In F. M. Gradstein, J. G. Ogg, M. D. Schmitz, and G. M. Ogg (Eds.), *Geologic Time Scale 2020*, pp. 1217–1255. Elsevier. 53

Gilbert, J. C. and C. Lemaréchal (1989). Some numerical experiments with variable-storage quasi-newton algorithms. *Mathematical Programming 45*(1), 407–435. 26

Glen, J. W. (1955). The creep of polycrystalline ice. *Proceedings of the Royal Society of London. Series A. Mathematical and Physical Sciences 228*(1175), 519–538. 7

Greve, R. (2005). Relation of measured basal temperatures and the spatial distribution of the geothermal heat flux for the greenland ice sheet. *Annals of Glaciology 42*, 424–432. 10

Greve, R. (2019). Geothermal heat flux distribution for the greenland ice sheet, derived by combining a global representation and information from deep ice cores. *Polar Data Journal 3*, 22–36. vi, 2, 11, 12, 28, 29, 30

Greve, R. and H. Blatter (2009). Advanced topics. In R. Greve and H. Blatter (Eds.), *Dynamics of Ice Sheets and Glaciers*, pp. 203–259. Berlin, Heidelberg: Springer Berlin Heidelberg. 26

Greve, R. and K. Hutter (1995). Polythermal three-dimensional modelling of the greenland ice sheet with varied geothermal heat flux. *Annals of Glaciology 21*, 8–12. 1

Grinsted, A. and D. Dahl-Jensen (2002). A monte carlo-tuned model of the flow in the northgrip area. *Annals of Glaciology 35*, 527–530. 67

Grotzinger, J. and T. Jordan (2017). Gletscher: Die tätigkeit des eises. In J. Grotzinger and T. Jordan (Eds.), *Press/Siever Allgemeine Geologie*, pp. 593–620. Berlin, Heidelberg: Springer Berlin Heidelberg. 1, 3, 4

Group, W. G. S. L. B. (2018). Global sea-level budget 1993–present. *Earth System Science Data 10*(3), 1551–1590. 1

Gulley, J. D., M. Grabiec, J. B. Martin, J. Jania, G. Catania, and P. Glowacki (2012). The effect of discrete recharge by moulins and heterogeneity in flow-path efficiency at glacier beds on subglacial hydrology. *Journal of Glaciology 58*(211), 926–940. 70, 71

Hammer, C., H. Clausen, W. Dansgaard, N. Gundestrup, S. Johnsen, and N. Reeh (1978). Dating of greenland ice cores by flow models, isotopes, volcanic debris and continental dust. *Journal of Glaciology 20*, 3–26. 13

Hewitt, I. (2021). Slow viscous flow. In A. Fowler and F. Ng (Eds.), *Glaciers and Ice Sheets in the Climate System: The Karthaus Summer School Lecture Notes*, pp. 1–28. Cham: Springer International Publishing. 5, 7

Hewitt, I. J. (2011). Modelling distributed and channelized subglacial drainage: the spacing of channels. *Journal of Glaciology 57*(202), 302–314. 21

HOCK, R. and R. L. HOOKE (1993, 3/29/2023). Evolution of the internal drainage system in the lower part of the ablation area of storglaciären, sweden. *GSA Bulletin 105*(4), 537–546. 70

Hudleston, P. J. (2015). Structures and fabrics in glacial ice: A review. *Journal of Structural Geology 81*, 1–27. 4

Jacka, T. H. (1984). Laboratory studies on relationships between ice crystal size and flow rate. *Cold Regions Science and Technology 10*(1), 31–42. 15

Johnsen, S. J., D. Dahl-Jensen, N. Gundestrup, J. P. Steffensen, H. B. Clausen, H. Miller, V. Masson-Delmotte, A. E. Sveinbjörnsdottir, and J. White (2001, 2023/03/21). Oxygen isotope and palaeotemperature records from six greenland ice-core stations: Camp century, dye-3, grip, gisp2, renland and northgrip. *Journal of Quaternary Science 16*(4), 299–307. 13, 18

Joughin, I., B. Smith, I. Howat, and T. Scambos (2016). Measures multi-year greenland ice sheet velocity mosaic, version 1. boulder, colorado usa. nasa national snow and ice data center distributed active archive center. 26

JOUGHIN, I., B. E. SMITH, and I. M. HOWAT (2018). A complete map of greenland ice velocity derived from satellite data collected over 20 years. *Journal of Glaciology 64*(243), 1–11. 26

Jouzel, J. and V. Masson-Delmotte (2007). Ice core records | antarctic stable isotopes. In S. A. Elias (Ed.), *Encyclopedia of Quaternary Science*, pp. 1242–1250. Oxford: Elsevier. 73

Kang, H., L. Zhao, M. Wolovick, and J. C. Moore (2022). Evaluation of six geothermal heat flux maps for the antarctic lambert–amery glacial system. *The Cryosphere 16*(9), 3619–3633. 1, 9

Karlsson, N. B. and D. Dahl-Jensen (2015). Response of the large-scale subglacial drainage system of northeast greenland to surface elevation changes. *The Cryosphere 9*(4), 1465–1479. 21, 70

Karlsson, N. B., A. M. Solgaard, K. D. Mankoff, F. Gillet-Chaulet, J. A. MacGregor, J. E. Box, M. Citterio, W. T. Colgan, S. H. Larsen, K. K. Kjeldsen, N. J. Korsgaard, D. I. Benn, I. J. Hewitt, and R. S. Fausto (2021). A first constraint on basal melt-water production of the greenland ice sheet. *Nature Communications 12*(1), 3461. 9, 21, 70

Kendall, C., D. H. Doctor, and M. B. Young (2014). 7.9 - environmental isotope applications in hydrologic studies. In H. D. Holland and K. K. Turekian (Eds.), *Treatise on Geochemistry (Second Edition)*, pp. 273–327. Oxford: Elsevier. 17, 20, 40

Khan, S. A., A. Aschwanden, A. A. Bjørk, J. Wahr, K. K. Kjeldsen, and K. H. Kjær (2015). Greenland ice sheet mass balance: a review. *Reports on Progress in Physics 78*(4), 046801. 1

Klaus, J. and J. J. McDonnell (2013). Hydrograph separation using stable isotopes: Review and evaluation. *Journal of Hydrology 505*, 47–64. 41

Kleiner, T., M. Rückamp, J. H. Bondzio, and A. Humbert (2015). Enthalpy benchmark experiments for numerical ice sheet models. *The Cryosphere 9*(1), 217–228. 26

Landais, A., J. P. Steffensen, N. Caillon, J. Jouzel, V. Masson-Delmotte, and J. Schwander (2004, 2023/03/28). Evidence for stratigraphic distortion in the greenland ice core project (grip) ice core during event 5e1 (120 kyr bp) from gas isotopes. *Journal of Geophysical Research: Atmospheres 109*(D6). 73

Larour, E., H. Seroussi, M. Morlighem, and E. Rignot (2012). Continental scale, high order, high spatial resolution, ice sheet modeling using the ice sheet system model (issm). *Journal of Geophysical Research: Earth Surface 117*(F1). 26

Lhomme, N., G. K. C. Clarke, and S. J. Marshall (2005). Tracer transport in the greenland ice sheet: constraints on ice cores and glacial history. *Quaternary Science Reviews 24*(1), 173–194. 74

Lindbäck, K., R. Pettersson, A. L. Hubbard, S. H. Doyle, D. van As, A. B. Mikkelsen, and A. A. Fitzpatrick (2015, 2023/03/20). Subglacial water drainage, storage, and piracy beneath the greenland ice sheet. *Geophysical Research Letters 42*(18), 7606–7614. 22, 23, 70

Lliboutry, L. and P. Duval (1985). Various isotropic and anisotropic ices found in glaciers and polar ice caps and their corresponding rheologies. *3*(2), 207–224. 26

Lucazeau, F. (2019). Analysis and mapping of an updated terrestrial heat flow data set. *Geochemistry, Geophysics, Geosystems 20*(8), 4001–4024. vi, 2, 12, 29, 30

MacGregor, J. A., M. A. Fahnestock, G. A. Catania, J. D. Paden, S. Prasad Gogineni, S. K. Young, S. C. Rybarski, A. N. Mabrey, B. M. Wagman, and M. Morlighem (2015). Radiostratigraphy and age structure of the greenland ice sheet. *Journal of Geophysical Research: Earth Surface 120*(2), 212–241. 13, 14, 15, 72

Martos, Y. M., T. A. Jordan, M. Catalán, T. M. Jordan, J. L. Bamber, and D. G. Vaughan (2018). Geothermal heat flux reveals the iceland hotspot track underneath greenland. *Geophysical Research Letters 45*(16), 8214–8222. vi, 2, 11, 28, 29

Masson-Delmotte, V., G. Dreyfus, P. Braconnot, S. Johnsen, J. Jouzel, M. Kageyama, A. Landais, M.-F. Loutre, J. Nouet, F. Parrenin, D. Raynaud, B. Stenni, and E. Tuenter (2006). Past temperature reconstructions from deep ice cores: relevance for future climate change. *Climate of the Past 2*(2), 145–165. 66, 73

McCormack, F. S., J. L. Roberts, C. F. Dow, T. Stål, J. A. Halpin, A. M. Reading, and M. J. Siegert (2022, 2023/03/29). Fine-scale geothermal heat flow in antarctica can increase simulated subglacial melt estimates. *Geophysical Research Letters 49*(15), e2022GL098539. 1

Meierbachtol, T., J. Harper, and N. Humphrey (2013, 2023/03/20). Basal drainage system response to increasing surface melt on the greenland ice sheet. *Science 341*(6147), 777–779. 23

Meierbachtol, T. W., J. T. Harper, J. V. Johnson, N. F. Humphrey, and D. J. Brinkerhoff (2015, 2023/03/29). Thermal boundary conditions on western greenland: Observational constraints and impacts on the modeled thermomechanical state. *Journal of Geophysical Research: Earth Surface 120*(3), 623–636. 1

Miller, J. B., M. D. Frisbee, T. L. Hamilton, and S. K. Murugapiran (2021). Recharge from glacial meltwater is critical for alpine springs and their microbiomes. *Environmental Research Letters 16*(6), 064012. 41

Morlighem, M., C. N. Williams, E. Rignot, L. An, J. E. Arndt, J. L. Bamber, G. Catania, N. Chauché, J. A. Dowdeswell, B. Dorschel, I. Fenty, K. Hogan, I. Howat, A. Hubbard, M. Jakobsson, T. M. Jordan, K. K. Kjeldsen, R. Millan, L. Mayer, J. Mouginot, B. P. Y. Noël, C. O'Cofaigh, S. Palmer, S. Rysgaard, H. Seroussi, M. J. Siegert, P. Slabon, F. Straneo, M. R. van den Broeke, W. Weinrebe, M. Wood, and K. B. Zinglersen (2017). Bedmachine v3: Complete bed topography and ocean bathymetry mapping of greenland from multibeam echo sounding combined with mass conservation. *Geophysical Research Letters 44*(21), 11,051–11,061. 1, 4, 27

Näslund, J.-O., P. Jansson, J. L. Fastook, J. Johnson, and L. Andersson (2005). Detailed spatially distributed geothermal heat-flow data for modeling of basal temperatures and meltwater production beneath the fennoscandian ice sheet. *Annals of Glaciology 40*, 95–101. 1, 9

Nienow, P., M. Sharp, and I. Willis (1998, 2023/03/29). Seasonal changes in the morphology of the subglacial drainage system, haut glacier d'arolla, switzerland. *Earth Surface Processes and Landforms 23*(9), 825–843. 70

Nye, J. F. (1963). Correction factor for accumulation measured by the thickness of the annual layers in an ice sheet. *Journal of Glaciology 4*(36), 785–788. 16, 33

O'Callaghan, J. F. and D. M. Mark (1984). The extraction of drainage networks from digital elevation data. *Computer vision, graphics, and image processing 28*(3), 323–344. 34, 35

Pattyn, F. (2003). A new three-dimensional higher-order thermomechanical ice sheet model: Basic sensitivity, ice stream development, and ice flow across subglacial lakes. *Journal of Geophysical Research: Solid Earth 108*(B8). 26

Petit, J. R., J. Jouzel, D. Raynaud, N. I. Barkov, J. M. Barnola, I. Basile, M. Bender, J. Chappellaz, M. Davis, G. Delaygue, M. Delmotte, V. M. Kotlyakov, M. Legrand, V. Y. Lipenkov, C. Lorius, L. PÉpin, C. Ritz, E. Saltzman, and M. Stievenard (1999). Climate and atmospheric history of the past 420,000 years from the vostok ice core, antarctica. *Nature 399*(6735), 429–436. 31, 32

Petrunin, A. G., I. Rogozhina, A. P. M. Vaughan, I. T. Kukkonen, M. K. Kaban, I. Koulakov, and M. Thomas (2013). Heat flux variations beneath central greenland's ice due to anomalously thin lithosphere. *Nature Geoscience 6*(9), 746–750. 10, 11

PICARRO, INC. (2017). L2140-i analyzer datasheet. *https://www.picarro.com/support/library/documents/l2140i_analyzer_datasheet*, Last accessed 29. March 2023. 66

Pollack, H. N., S. J. Hurter, and J. R. Johnson (1993). Heat flow from the earth's interior: Analysis of the global data set. *Reviews of Geophysics 31*(3), 267–280. 12, 28, 29

Quinn, P., K. Beven, P. Chevallier, and O. Planchon (1991). The prediction of hillslope flow paths for distributed hydrological modelling using digital terrain models. *Hydrological Processes 5*(1), 59–79. 35, 36

Reeh, N., H. Oerter, and H. H. Thomsen (2002). Comparison between greenland ice-margin and ice-core oxygen-18 records. *Annals of Glaciology 35*, 136–144. 20, 74

Rezvanbehbahani, S., L. A. Stearns, A. Kadivar, J. D. Walker, and C. J. van der Veen (2017). Predicting the geothermal heat flux in greenland: A machine learning approach. *Geophysical Research Letters 44*(24), 12,271–12,279. 10, 11, 27

Rezvanbehbahani, S., L. A. Stearns, C. J. van der Veen, G. K. A. Oswald, and R. Greve (2019). Constraining the geothermal heat flux in greenland at regions of radar-detected basal water. *Journal of Glaciology 65*(254), 1023–1034. 10

Rignot, E. and J. Mouginot (2012, 2023/03/26). Ice flow in greenland for the international polar year 2008–2009. *Geophysical Research Letters 39*(11). 4, 44

Rippin, D., I. Willis, N. Arnold, A. Hodson, J. Moore, J. Kohler, and H. BjöRnsson (2003, 2023/03/20). Changes in geometry and subglacial drainage of midre lovénbreen, svalbard, determined from digital elevation models. *Earth Surface Processes and Landforms 28*(3), 273–298. 22, 23, 70

Rogozhina, I., J. M. Hagedoorn, Z. Martinec, K. Fleming, O. Soucek, R. Greve, and M. Thomas (2012, 2023/03/23). Effects of uncertainties in the geothermal heat flux distribution on the greenland ice sheet: An assessment of existing heat flow models. *Journal of Geophysical Research: Earth Surface 117*(F2). 2, 9, 10, 27

Rogozhina, I., A. G. Petrunin, A. P. M. Vaughan, B. Steinberger, J. V. Johnson, M. K. Kaban, R. Calov, F. Rickers, M. Thomas, and I. Koulakov (2016). Melting at the base of the greenland ice sheet explained by iceland hotspot history. *Nature Geoscience 9*(5), 366–369. 11, 13

Röthlisberger, H. (1972). Water pressure in intra- and subglacial channels. *Journal of Glaciology 11*(62), 177–203. 51

Rückamp, M. (2022, October). A 3d issm model of the greenand ice sheet set up for thermomechanical steadystate simulations. Private communication. 26

Rückamp, M., A. Humbert, T. Kleiner, M. Morlighem, and H. Seroussi (2020). Extended enthalpy formulations in the ice-sheet and sea-level system model (issm) version 4.17: discontinuous conductivity and anisotropic streamline upwind petrov–galerkin (supg) method. *Geoscientific Model Development 13*(9), 4491–4501. 26

Rysgaard, S., J. Bendtsen, J. Mortensen, and M. K. Sejr (2018). High geothermal heat flux in close proximity to the northeast greenland ice stream. *Scientific Reports 8*(1), 1344. 12

Seibert, J. and B. L. McGlynn (2007). A new triangular multiple flow direction algorithm for computing upslope areas from gridded digital elevation models. *Water Resources Research 43*(4). 34, 35, 36, 37

Seroussi, H., M. Morlighem, E. Rignot, A. Khazendar, E. Larour, and J. Mouginot (2013). Dependence of century-scale projections of the greenland ice sheet on its thermal regime. *Journal of Glaciology 59*(218), 1024–1034. 26, 27

Shapiro, N. M. and M. H. Ritzwoller (2004). Inferring surface heat flux distributions guided by a global seismic model: particular application to antarctica. *Earth and Planetary Science Letters 223*(1), 213–224. vi, 2, 12, 29, 30

Shepherd, A., E. Ivins, E. Rignot, B. Smith, M. van den Broeke, I. Velicogna, P. Whitehouse, K. Briggs, I. Joughin, G. Krinner, S. Nowicki, T. Payne, T. Scambos, N. Schlegel, G. A, C. Agosta, A. Ahlstrøm, G. Babonis, V. R. Barletta, A. A. Bjørk, A. Blazquez, J. Bonin, W. Colgan, B. Csatho, R. Cullather, M. E. Engdahl, D. Felikson, X. Fettweis, R. Forsberg, A. E. Hogg, H. Gallee, A. Gardner, L. Gilbert, N. Gourmelen, A. Groh, B. Gunter, E. Hanna, C. Harig, V. Helm, A. Horvath, M. Horwath, S. Khan, K. K. Kjeldsen, H. Konrad, P. L. Langen, B. Lecavalier, B. Loomis, S. Luthcke, M. McMillan, D. Melini, S. Mernild, Y. Mohajerani, P. Moore, R. Mottram, J. Mouginot, G. Moyano, A. Muir, T. Nagler, G. Nield, J. Nilsson, B. Noël, I. Otosaka, M. E. Pattle, W. R. Peltier, N. Pie, R. Rietbroek, H. Rott, L. Sandberg Sørensen, I. Sasgen, H. Save, B. Scheuchl, E. Schrama, L. Schröder, K.-W. Seo, S. B. Simonsen, T. Slater, G. Spada, T. Sutterley, M. Talpe, L. Tarasov, W. J. van de Berg, W. van der Wal, M. van Wessem, B. D. Vishwakarma, D. Wiese, D. Wilton, T. Wagner, B. Wouters, J. Wuite, and T. I. Team (2020). Mass balance of the greenland ice sheet from 1992 to 2018. *Nature 579*(7798), 233–239. 1, 4

Shreve, R. L. (1972). Movement of water in glaciers. *Journal of Glaciology 11*(62), 205–214. 22, 70

Smith-Johnsen, S., B. de Fleurian, N. Schlegel, H. Seroussi, and K. Nisancioglu (2020). Exceptionally high heat flux needed to sustain the northeast greenland ice stream. *The Cryosphere 14*(3), 841–854. 9, 13, 27

Smith-Johnsen, S., N. J. Schlegel, B. de Fleurian, and K. H. Nisancioglu (2020, 2023/03/23). Sensitivity of the northeast greenland ice stream to geothermal heat. *Journal of Geophysical Research: Earth Surface 125*(1), e2019JF005252. 1, 7, 10

Sommers, A., H. Rajaram, and M. Morlighem (2018). Shakti: Subglacial hydrology and kinetic, transient interactions v1.0. *Geoscientific Model Development 11*(7), 2955–2974. 21

Stauffer, B., J. Fluckiger, E. Monnin, T. Nakazawa, S. Aoki, et al. (2003). Discussion of the reliability of co2, ch4 and n2o records from polar ice cores. *Mem. Natl Inst. Polar Res., Spec. Issue 57*, 139–152. 74

Tarboton, D. G. (1997). A new method for the determination of flow directions and upslope areas in grid digital elevation models. *Water Resources Research 33*(2), 309–319. 34, 36, 39

Tranter, M. and J. L. Wadham (2014). 7.5 - geochemical weathering in glacial and proglacial environments. In H. D. Holland and K. K. Turekian (Eds.), *Treatise on Geochemistry (Second Edition)*, pp. 157–173. Oxford: Elsevier. 75

Urra, A., J. Wadham, J. R. Hawkings, J. Telling, J. E. Hatton, J. C. Yde, B. Hasholt, D. van As, M. P. Bhatia, and P. Nienow (2019). Weathering dynamics under contrasting greenland ice sheet catchments. *Frontiers in Earth Science 7*. 75

Walker, M., S. Johnsen, S. O. Rasmussen, T. Popp, J.-P. Steffensen, P. Gibbard, W. Hoek, J. Lowe, J. Andrews, S. Björck, L. C. Cwynar, K. Hughen, P. Kershaw, B. Kromer, T. Litt, D. J. Lowe, T. Nakagawa, R. Newnham, and J. Schwander (2009). Formal definition and dating of the gssp (global stratotype section and point) for the base of the holocene using the greenland ngrip ice core, and selected auxiliary records. *Journal of Quaternary Science 24*(1), 3–17. 19, 53

Walker, M., S. Johnsen, S. O. Rasmussen, J.-P. Steffensen, T. Popp, P. Gibbard, W. Hoek, J. Lowe, J. Andrews, S. Björck, L. Cwynar, K. Hughen, P. Kershaw, B. Kromer, T. Litt, D. J. Lowe, T. Nakagawa, R. Newnham, and J. Schwander (2008, 06). The global stratotype section and point (gssp) for the base of the holocene series/epoch (quaternary system/period) in the ngrip ice core. *International Union of Geological Sciences 31*(2), 264–267. 19, 53

Werder, M. A., I. J. Hewitt, C. G. Schoof, and G. E. Flowers (2013, 2023/03/20). Modeling channelized and distributed subglacial drainage in two dimensions. *Journal of Geophysical Research: Earth Surface 118*(4), 2140–2158. 21

Willis, I. C., C. D. Fitzsimmons, K. Melvold, L. M. Andreassen, and R. H. Giesen (2012, 2023/03/20). Structure, morphology and water flux of a subglacial drainage system, midtdalsbreen, norway. *Hydrological Processes 26*(25), 3810–3829. 22, 23, 34

Zeising, O. and A. Humbert (2021). Indication of high basal melting at the eastgrip drill site on the northeast greenland ice stream. *The Cryosphere 15*(7), 3119–3128. 13

Zwally, H. J., M. B. Giovinetto, M. A. Beckley, and J. L. Saba (2012). Antarctic and greenland drainage systems. *GSFC Cryospheric Sciences Laboratory https://earth.gsfc.nasa.gov/cryo/data/polar-altimetry/antarctic-and-greenland-drainage-systems*, accessed on 29 March 2023. 4, 5